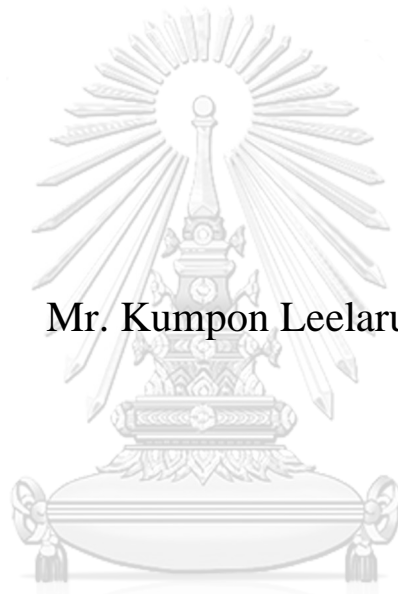


**EFFECT OF ZIRCONIUM ON PHYSICAL PROPERTIES
AND CORROSION RESISTANCE OF CHROMIUM
AND CHROMIUM NITRIDE FILMS**



Mr. Kumpon Leelaruedee

จุฬาลงกรณ์มหาวิทยาลัย
CHULALONGKORN UNIVERSITY

**A Dissertation Submitted in Partial Fulfillment of the Requirements
for the Degree of Doctor of Engineering in Metallurgical and Materials**

Engineering

Department of Metallurgical Engineering

FACULTY OF ENGINEERING

Chulalongkorn University

Academic Year 2019

Copyright of Chulalongkorn University

ผลของเซอร์โคเนียมต่อสมบัติทางกายภาพและความต้านทานการกัดกร่อนของฟิล์มโครเมียมและโครเมียมไนไตรด์



วิทยานิพนธ์นี้เป็นส่วนหนึ่งของการศึกษาตามหลักสูตรปริญญาวิศวกรรมศาสตรดุษฎีบัณฑิต
สาขาวิชาวิศวกรรมโลหการและวัสดุ ภาควิชาวิศวกรรมโลหการ
คณะวิศวกรรมศาสตร์ จุฬาลงกรณ์มหาวิทยาลัย
ปีการศึกษา 2562
ลิขสิทธิ์ของจุฬาลงกรณ์มหาวิทยาลัย

ก่าพล สีลาฤดี : ผลของเซอร์โคเนียมต่อสมบัติทางกายภาพและความต้านทานการกัดกร่อนของฟิล์มโครเมียมและโครเมียมไนไตรด์. (EFFECT OF ZIRCONIUM ON PHYSICAL PROPERTIES AND CORROSION RESISTANCE OF CHROMIUM AND CHROMIUM NITRIDE FILMS) อ.ที่ปรึกษาหลัก : รศ. ดร.ปฐมา วิทยุทธิพิทักษ์กุล, อ.ที่ปรึกษาร่วม : ผศ. ดร.นิตินยวงษ์,ดร.ฮิเดยูกิ คุวาสาร

การกัดกร่อนเป็นปรากฏการณ์ที่มักจะเกิดขึ้นบนพื้นผิวโลหะและนำมาซึ่งความเสียหายของชิ้นงาน ด้วยสาเหตุนี้ปัญหาเกี่ยวกับการกัดกร่อนจึงได้รับความสนใจจากนักวิจัยต่างๆ เพื่อที่จะหาทางป้องกันและยืดระยะเวลาการใช้งานโลหะ การเคลือบผิวด้วยฟิล์มโครเมียมหรือโครเมียมไนไตรด์เป็นหนึ่งในวิธีที่ได้รับความนิยม เนื่องจากเป็นวิธีการเพิ่มความต้านทานการกัดกร่อนโดยไม่จำเป็นต้องเปลี่ยนทั้งชิ้นงาน อย่างไรก็ตามสมบัติของฟิล์มจากวิธีเคลือบผิวแบบปกติอาจไม่ให้ความต้านทานการกัดกร่อนที่สูงเพียงพอสำหรับการใช้งานในสภาวะที่มีการกัดกร่อนรุนแรง ด้วยเหตุนี้การปรับปรุงโครงสร้างของชั้นเคลือบให้เป็นแบบอสัณฐานจึงเป็นวิธีที่ได้รับความนิยมในการเพิ่มความต้านทานการกัดกร่อน

ฟิล์มบางอสัณฐานแบบไร้รูปร่างของโครเมียมเซอร์โคเนียมสามารถถูกเตรียมได้ด้วยวิธีการแมกนีตรอนโคสปีดเตอริง โดยการเตรียมด้วยส่วนผสมที่เหมาะสม (46 เปอร์เซ็นต์โดยอะตอม) พร้อมกับการทำให้อะตอมที่พื้นผิวตัวรองรับมีพลังงานต่ำจะขัดขวางการแพร่และการเกิดผลึก ทำให้ชั้นได้ชั้นฟิล์มที่มีโครงสร้างเป็นแบบอสัณฐาน โครงสร้างอสัณฐานแบบไร้รูปร่างของฟิล์มโครเมียมเซอร์โคเนียมส่งผลให้ฟิล์มมีความต้านทานการกัดกร่อนที่ดี เห็นได้จากค่าความต้านทานของฟิล์มและศักย์ไฟฟ้าการกัดกร่อนที่สูง กระแสไฟฟ้าการกัดกร่อนที่ต่ำและความสามารถในการเกิดชั้นป้องกันการกัดกร่อน การมีอยู่ร่วมกันของโครเมียมและเซอร์โคเนียมเป็นปัจจัยสำคัญที่ลดการละลายของเซอร์โคเนียมไดออกไซด์ที่เป็นสารประกอบหลักของชั้นป้องกันการกัดกร่อนของฟิล์มโครเมียมเซอร์โคเนียม

ฟิล์มโครเมียมเซอร์โคเนียมไนไตรด์สามารถถูกเตรียมได้ด้วยวิธีการรีแอคทีฟแมกนีตรอนโคสปีดเตอริง โดยพบว่าสารประกอบเชิงซ้อนของโครเมียมเซอร์โคเนียมไนไตรด์เป็นสารประกอบหลักในฟิล์มทั้งหมด การเติมเซอร์โคเนียมในปริมาณที่มากขึ้นจะลดขนาดผลึกของสารประกอบเชิงซ้อนเนื่องจากผลของพลังงานความเครียดพร้อมกันกับการกระตุ้นให้เกิดโครงสร้างอสัณฐานของเซอร์โคเนียมออกไซด์ในไตรด์ การเติมเซอร์โคเนียมที่ 0.578 สัดส่วนโดยอะตอมนั้นเพียงพอที่จะทำให้โครงสร้างอสัณฐานมีปริมาณมากพอที่จะถูกตรวจสอบได้ด้วยเครื่องเอ็กซ์เรย์

การปรับปรุงรอยต่อระหว่างเนื้อฟิล์มและฟิล์มเป็นอีกหนึ่งปัจจัยที่ส่งผลต่อโครงสร้างผลึกของฟิล์ม งานวิจัยนี้ได้แสดงให้เห็นว่าการเติมชั้นรอยต่อที่มีโครงสร้างเป็นอสัณฐานสามารถกระตุ้นให้เกิดโครงสร้างอสัณฐานในชั้นฟิล์มด้านบนได้โดยการทำตัวเป็นต้นแบบที่มีการจัดเรียงตัวแบบสุ่ม วิธีนี้สามารถกระตุ้นให้เกิดโครงสร้างอสัณฐานได้อย่างมีประสิทธิภาพ ดังเห็นได้จากการที่ไม่พบพิกัดในผลทดสอบเอ็กซ์เรย์ โครงสร้างอสัณฐานไร้รูปร่างที่เกิดขึ้นในชั้นฟิล์มไนไตรด์นี้ส่งเสริมให้ฟิล์มมีความต้านทานการกัดกร่อนที่มากขึ้นเนื่องจากการที่ฟิล์มไม่มีจุดอ่อนไหวต่อการกัดกร่อน

สาขาวิชา วิศวกรรมโลหการและวัสดุ
ปีการศึกษา 2562

ลายมือชื่อนิติดี
ลายมือชื่อ อ.ที่ปรึกษาหลัก
ลายมือชื่อ อ.ที่ปรึกษาร่วม
ลายมือชื่อ อ.ที่ปรึกษาร่วม

5871443121 : MAJOR METALLURGICAL AND MATERIALS ENGINEERING

KEYWORD: Chromium, Zirconium, Corrosion, Amorphization, Nitride, Thin film

Kumpon

Leelaruedee

:

EFFECT OF ZIRCONIUM ON PHYSICAL PROPERTIES

AND CORROSION RESISTANCE OF CHROMIUM AND CHROMIUM

NITRIDE FILMS. Advisor: Assoc. Prof. Patama Visuttipitukul, Ph.D. Co-

advisor: Asst. Prof. Niti Yongvanich, Ph.D., Hideyuki Kuwahara, D.Eng.

Corrosion is a common phenomenon which usually undergoes on metal surface leading to structural failure. Consequently, this topic has attracted many researchers to look for ways to prevent corrosion and extend lifetime of service. Coating with chromium (Cr) or chromium nitride (CrN) is the one popular technique, given the high corrosion resistance and obviating whole part replacement. However, the conventional film's properties might not provide enough resistance for using in some severe environments. Tailoring structure to amorphous is usually considered for improve corrosion resistance.

Thin amorphous featureless of CrZr-film was successfully fabricated by magnetron co-sputtering. The suitable composition (46 %at.Zr) with low energetic adatoms due to low sputtering power, restricted adatoms diffusion and nucleation in a similar way to frozen them like amorphous structure. The amorphous featureless in CrZr-film contributed to the excellent anti-corrosion property as seen by the high value of R_{film} , E_{corr} with low I_{corr} and passivation ability. The co-existing of Cr and Zr played the important role for reducing dissolution of zirconium oxide (ZrO_2) which was the major compound in CrZr-passive film.

For nitride films, the CrZrN could be fabricated by reactive magnetron co-sputtering. Complex nitride of Cr and Zr, (Cr,Zr)N, was the predominant phase in all sputtering films. Addition of Zr with higher concentration refined crystallite size of (Cr,Zr)N due to strain confinement and simultaneously promote an amorphous Zr_2ON_2 . Addition of Zr at 0.578 atomic fraction was enough for promoting amorphous phase which was high enough content for detectable by XRD.

Modification interface between matrix and film is one parameter affecting film's crystallinity. This work revealed that addition of amorphous CrZr-interlayer could promote amorphous structure in the top nitride film by performing as "random atomic arrangement template" for top film. It was effective method for promoting amorphization as seen by no evidence of crystallinity in XRD result. This amorphous featureless nitride film contributed the excellent corrosion resistance due to less of susceptible points and columnar structure.

Field of Study:	Metallurgical and Materials Engineering	Student's Signature
Academic Year:	2019	Advisor's Signature
		Co-advisor's Signature
		Co-advisor's Signature

ACKNOWLEDGEMENTS

Firstly, I would like to thank my “Super advisor”, Associate Professor Patama Visuttipitukul, Ph.D., who patience and played the greatest role for supporting me through the challenge of studying. She has guided, advised, and supported me for my long journey of study since the first year of master’s degree. I passed through several difficult situations with her advices and finally I finished my doctoral degree. I am so proud to being a part of surface engineering laboratory and department of metallurgical engineering, Chulalongkorn university.

For Assistant Professor Niti Yongvanich, Ph.D., my Co-advisor, is the other important person who guided, advised, and supported me through my career of student. He has supported me since I studied in bachelor’s degree at Silpakorn university, and recommended me to study at Chulalongkorn with Associate Professor Patama Visuttipitukul. For this successful, they are the important person who gave this opportunity for me.

I also would like to thank my Japanese co-advisor, Dr. Hideyuki Kuwahara, clericals, and all of teachers in my department. They helped, advised and taught me for many years. Thanks also go to my friends, and my lovely co-works for supporting, laughing, and providing a grate time in surface engineering laboratory.

Finally, I cannot adequately express gratitude to my family who have been supporting everything and encouragement for me through this successful.

Kumpon Leelaruedee

TABLE OF CONTENTS

	Page
ABSTRACT (THAI)	iii
ABSTRACT (ENGLISH)	iv
ACKNOWLEDGEMENTS	v
TABLE OF CONTENTS	vi
LIST OF FIGURES	ix
LIST OF TABLES	xii
Chapter 1 General introduction	1
1.1 Statement of problems	1
1.2 Objectives	4
1.3 Scopes	4
1.4 Expected or Anticipated Benefit Gain	6
Chapter 2 Literature reviews	7
2.1 Corrosion in metals [33]	7
2.2 Thermodynamics of corrosion [33]	8
2.3 Kinetics and corrosion measurement [33]	9
2.3.1 Potentiodynamic polarization	9
2.3.2 Electrochemical impedance spectroscopy	10
2.3.2.1 Nyquist plot	11
2.3.2.2 Bode plot	12
2.3.2.3 Interpretation of EIS	13
2.4 Forms of corrosion in metals and metal alloys	15
2.4.1 Uniform corrosion	16
2.4.2 Galvanic corrosion	16
2.4.3 Dealloying	17
2.4.4 Crevice corrosion	17

2.4.5 Pitting corrosion	18
2.5 Corrosion prevention	18
2.5.1 Environment modifications and materials selection	18
2.5.2 Cathodic protection and sacrificial anode	19
2.5.3 Painting.....	19
2.5.4 Coating	19
2.6 Coating materials	20
2.6.1 Chromium.....	20
2.6.2 Chromium nitride compounds.....	22
2.7 Coating methods	25
2.7.1 Magnetron sputtering	25
2.7.1.1 Instrumental parameters of magnetron sputtering.....	26
2.7.1.2 Process modification	28
2.8 Concepts of research.....	29
Chapter 3 Metallic film of chromium-zirconium.....	31
3.1 Chromium-zirconium film.....	31
3.2 Film preparation and characterizations.....	31
3.2.1 Film preparation	31
3.2.2 Material characterizations	33
3.2.3 Corrosion behavior analysis	33
3.3 Results and discussions.....	35
3.3.1 Microstructure and morphology	35
3.3.2 Phase, chemical composition and crystallinity.....	39
3.3.3 Corrosion behavior	42
3.3.3.1 Open circuit monitoring	42
3.3.3.2 Impedance measurement	43
3.3.3.3 Potentiodynamic polarization.....	48
3.3.4 SEM observation of corroding films	52
3.3.5 XPS analysis of corroding film	53

3.3.4.1 XPS analysis of Cr-film.....	53
3.3.4.2 XPS analysis of Zr-film.....	56
3.3.4.3 XPS analysis of CrZr-film.....	58
3.3.6 Effect of the oxide/hydroxide ratio on corrosion property.....	61
3.4 Summary.....	64
Chapter 4 Chromium-zirconium nitride film.....	66
4.1 Chromium-zirconium nitride film	66
4.2 Film preparation and characterizations.....	66
4.2.1 Film preparation	66
4.2.2 Material characterizations	68
4.3 Results and discussions.....	68
4.3.1 Microstructure and morphology	68
4.3.2 Phase, chemical composition, and crystallinity.....	71
4.3.3 Effect of interlayer addition and corrosion property	78
4.4 Summary.....	86
Chapter 5 Conclusions	88
5.1 Chromium-zirconium metallic film.....	88
5.2 Chromium-zirconium nitride film	89
REFERENCES	92
Appendix A General information.....	101
A.1 Materials and substrate preparation	101
A.2 Thickness measurement with image J software.....	102
A.3 The XRD patterns for analyzation	102
VITA.....	109

LIST OF FIGURES

	Page
Figure 2-1 Potentiodynamic polarization curve.....	10
Figure 2-2 Example of Nyquist plot	12
Figure 2-3 Bode plot of coating specimen.....	13
Figure 2-4 Equivalent circuits model of coating specimen	14
Figure 2-5 Relationship between atomic size differences (δ) and composition in chromium-zirconium system	22
Figure 2-6 Potentiodynamic polarization curves of (a) AISI 304 stainless steels and (b) CrN coating	23
Figure 2-7 Binary phases diagram of chromium-nitrogen.....	24
Figure 2-8 XRD patterns of CrZrN films: (a) (Cr-rich)N, (b) (Cr-Zr)N and (c) (Zr-rich)N	25
Figure 2-9 Schematic of reactive magnetron sputtering chamber	26
Figure 3-1 FESEM images of metallic films (a) - (b) Cr-film, (c) - (d) Zr-film and (e) - (f) CrZr-film	36
Figure 3-2 TEM images of the FIB specimen of CrZr-film	37
Figure 3-3 Topographic images of films by AFM (a) - (b) Cr-film, (c) - (d) Zr-film and (e) - (f) CrZr-film	38
Figure 3-4 XRD patterns of metallic films and substrate	40
Figure 3-5 Prediction of amorphous formation zone in chromium-zirconium binary system and composition of the CrZr-film.....	40
Figure 3-6 HRTEM image (a) and EDP (b) of the CrZr-film.....	41
Figure 3-7 Binary phase diagram of chromium and zirconium.....	42
Figure 3-8 OCP monitoring with a function of immersion time	43

Figure 3-9 Bode phase of metallic films.....	44
Figure 3-10 Bode modulus of metallic films	44
Figure 3-11 Nyquist plot of metallic films	45
Figure 3-12 Equivalent circuit models (a) bare H13 substrate and (b) films on H13 substrate	46
Figure 3-13 Potentiodynamic polarization of metallic film and substrate.....	49
Figure 3-14 Illustration of corrosion process and passivation on the CrZr-film	50
Figure 3-15 Illustration of corrosion process and passivation on columnar films.....	51
Figure 3-16 SEM after potentiodynamic polarization testing (a) - (c) Cr-film, Zr-film and CrZr-film.....	53
Figure 3-17 XPS evolution of Cr 2p and O 1s spectra in Cr-film	54
Figure 3-18 Compounds profiles of Cr-film with sputtering time.....	55
Figure 3-19 XPS evolution of Zr 3d and O 1s spectra in Zr-film.....	56
Figure 3-20 Compounds profile of Zr film with sputtering time.....	57
Figure 3-21 XPS evolution of Cr 2p, Zr 3d and O 1s of CrZr-film.....	59
Figure 3-22 Compounds profile of CrZr-film with sputtering time	61
Figure 3-23 Oxide/hydroxide ration with sputtering time	62
Figure 4-1 Cross-sectional FESEM images of nitride films; (a) Low-Zr, (b) Med-Zr and (c) High-Zr	69
Figure 4-2 AFM topographic images of nitride films.....	70
Figure 4-3 XRD patterns of nitride films.....	72
Figure 4-4 Lattice parameter of (Cr,Zr)N with a zirconium fraction in nitride film ...	72
Figure 4-5 XPS spectra of Cr 2p _{3/2} in nitride films.....	74
Figure 4-6 XPS spectra of Zr 3d in nitride films	75
Figure 4-7 XPS spectra of N 1s in nitride films.....	76

Figure 4-8 XPS spectra of O 1s in nitride films.....	77
Figure 4-9 Compound fraction in nitride films.....	78
Figure 4-10 FESEM images of the Int.-MedZr film: (a) SEM image and (b) BSE image.....	80
Figure 4-11 AFM Topographic images of the Int.-MedZr film.....	80
Figure 4-12 XRD patterns of Int.-Med-Zr film and Med-Zr	81
Figure 4-13 Out-view TEM image of the Int.-MedZr film.....	81
Figure 4-14 HRTEM image at junction between interlayer and nitride of the Int.-MedZr.....	82
Figure 4-15 HRTEM image and EDP in the interlayer area of Int.-MedZr film.....	82
Figure 4-16 HRTEM image and EDP in the nitride area of Int.-MedZr film.....	83
Figure 4-17 HRTEM image in the nitride area of Int.-MedZr film.....	83
Figure 4-18 EDP of the top nitride and calculated real space.....	84
Figure 4-19 Potentiodynamic polarization of Int.-MedZr comparing with other reports	85

LIST OF TABLES

	Page
Table 2-1 Relationship of equivalent circuits to impedance and phase shift.....	14
Table 2-2 The popular equivalent circuit models for film specimens	15
Table 3-1 Details of deposition parameters	32
Table 3-2 Surface roughness of films measured by AFM	38
Table 3-3 Summarized of equivalent circuit model.....	46
Table 3-4 Corrosion parameters of specimens.....	49
Table 3-5 Deconvolution of XPS spectra in the Cr-film	55
Table 3-6 Deconvolution of XPS spectra in the Zr-film.....	57
Table 3-7 Deconvolution of XPS spectra in the CrZr-film.....	60
Table 4-1 Details of deposition parameters	67
Table 4-2 Surface roughness and chemical compositions of nitride films	70
Table 4-3 Amount of chromium and zirconium in each compound calculated by EDS and XPS results	77
Table 4-4 Deposition parameters of Int.-MedZr.....	79

Chapter 1

General introduction

1.1 Statement of problems

Corrosion is an electrochemical, destructive process which usually undergoes on metals/alloys and is the major cause of structural failure resulting in plants shutdown, unsafe operations even decrease. The “National Association of Corrosion Engineers” (NACE) reported that the global cost of corrosion was approximately 2.5 trillion U.S. dollar in 2016 and continuously increased every year. Consequently, the topic of corrosion has attracted researchers to look for ways to prevent corrosion damage thereby achieving longer lifetime of services. For this reason, chromium (Cr) has drawn much attention due to its corrosion resistance and a self-healing protective passive layer. From “the national academics press” report, the mine chromium production was produced about 23,700 in thousand metric tons in 2010 and still on demanded. The main purpose of using chromium is a providing an anti-corrosion property as seen by it is an essential alloying element in stainless steel. Not only is it used in the form of a major alloy element in stainless steels, a layer of chromium and its alloys is also typically applied on surfaces of iron and steel components. This is an effective and economical technique which is also decorative, obviating whole part replacement and could protect substrate from corrosion attack.

Several studies revealed that the microstructural integrity and durability of the coating layer are the keys for determining functionality and operating life [1-4]. These two features are governed by the selection of appropriate materials with tailored structures and environmental parameters, e.g. pH and temperature. Unfortunately,

chromium alloy coatings are particularly prone to degrade under reducing saline environments. Several attempts have been done to improve corrosion resistance and achieve a good passive film such as thickening, phase modifications and alloying elements etc. [1-4]. Tailoring structure to amorphous is the interesting method which could provide an excellent corrosion resistance [4-6]. Amorphous structure with uniformity has been reported to successfully inhibit pit formation, which is the main root cause of passive film failure, due to less defective interfacial region [7, 8].

With the purpose of amorphous coating, several chemical composition by material design of metal-metal binary systems has been investigated and developed by many researchers for example K. Hashimoto (1993), D. Landolt (1998), M. Kitada (2005), B. Mallia (2007), D. Wang (2012), H. Skliarova (2015) and J. D. Schuler (2017) [2, 6, 9-13]. Noteworthy, the degree of crystallinity in various metallic binary could be decreased when zirconium was incorporated [13, 14]. Ali *et al.* [15] reported that zirconium base with chromium 20 atomic percentage (%at.) could develop a partially amorphous structure which improves corrosion resistance in HCl solution by the formation of an effective passive layer. Several studies have reported that addition of zirconium increased the possibility of oxide formation in the form of zirconium oxide (ZrO_2) which is an effective passive layer [6, 16-19]. Thus, a further improvement in corrosion resistance of chromium film was expected by tailoring with zirconium addition especially for forming an effective passive layer.

Not only using in metallic coating, chromium was also used in ceramic compound coating [20-24]. Chromium nitride (CrN) is a kind of chromium compounds which has been used for coating application due to its high corrosion resistance, high hardness and low friction coefficient [20-23]. In addition, it was

reported that addition of zirconium (Zr) into CrN tended to reduce crystallite size of CrN from 11 to 7 nm with 31%at. Zr addition, and a small percentage of Zr addition improved corrosion resistance of the nitride films [25-28]. For that tendency, researchers aim to addition Zr with high percentages for achieving amorphous nitride films. Therefore, Zr demonstrated a good potential for addition into both of Cr and CrN because of possibility to promote amorphization and improve corrosion resistance. Published reports only stated that the small amount of Zr addition and did not investigate in detail about phasic nature of the metallic Cr-Zr films and CrZrN films with a high degree of Zr addition. Therefore, researchers have been interested to study about effect of Zr addition on phase evolution, amorphization and corrosion behavior of the Cr-Zr and CrZrN films for using in anti-corrosion application.

Although film preparations could be done by several methods [25, 29, 30], magnetron sputtering is an outstanding method. It is convenience, powerful, reliable method and could perform in a wide range of temperature or work with reactive gases including nitrogen gas [20, 31]. Moreover, the desired film's properties could be achieved by controlling of processing parameters. For achieving amorphous films, the processing parameters should provide the low adatoms energy or mobility as low as possible e.g. no auxiliary heat and bias voltage supply. Thus, magnetron sputtering was an appropriate method for preparing both of thin metallic and nitride films in this research. From the industrial point of view, plasma ignition in nitride deposition process usually starts from only argon gas then introducing nitride gas. The metallic interlayer between substrate and nitride film is inevitable. From literature reviews, amorphous interface at substrate or matrix interface could promote amorphization in

the top films [32]. Therefore, researchers are also interesting to preparing amorphous interlayer and investigate possibility to promote amorphization in top nitride films.

As above described, this research was categorized into 2 main sections according to the types of films: metallic and nitride films. All films were deposited on silicon wafer and polished AISI H13 steel by magnetron co-sputtering. For metallic section, amorphization was done by material design of Cr and Zr. In the case of nitride section, amorphization was done by 2 techniques: material design and interface modification. For material design in nitride section, various Zr content films were fabricated and investigated effect of Zr addition without the interlayer. Then, effect of the amorphous interlayer on amorphization in top nitride films was investigated. All films (both of metallic and nitride films) was clarified about physical properties and relation of those parameters to corrosion behavior.

1.2 Objectives

1. Investigate effect of zirconium addition to microstructure, morphology, phase evolution, corrosion behavior of the chromium-zirconium metallic films prepared by magnetron sputtering.
2. Investigate effect of zirconium addition and amorphous interlayer to microstructure, morphology, phase evolution of chromium-zirconium nitride films prepared by magnetron sputtering.

1.3 Scopes

This research was categorized into two main sections including metallic and nitride section. For the metallic section, all films were prepared by dual-head magnetron co-sputtering of chromium and zirconium targets with argon as working

gas. Base and working pressure were controlled at 7.5×10^{-6} and 3.0×10^{-3} Torr, respectively. Metallic films consisted of 3 specimens according to zirconium contents: pure chromium (Cr-film), mixture of chromium-zirconium (CrZr-film) and pure zirconium (Zr-film). Films were deposited on (100) silicon wafer and polished AISI H13 steel with rotating substrate holder speed 4 rpm for achieving film homogeneity.

In the case of nitride films, they were deposited on those substrates by reactive magnetron co-sputtering of chromium and zirconium targets with argon and nitrogen as a working gas and reactive gas. The flow rate of those gases was controlled at 40.0 and 4.0 sccm, respectively. Base pressure and working pressure for nitride films preparation were 2.5×10^{-4} and 8.5×10^{-3} torr, respectively. Nitride films were also categorized to three groups various on zirconium contents according to low-zirconium (Low-Zr), medium-zirconium (Med-Zr) and high-zirconium (High-Zr). Deposition time was kept at 60 minutes for all depositions. In the case of nitride film with interlayer, the amorphous film condition in metallic section would be designed to the amorphous interlayer.

Microstructure and morphology of films were investigated by field-emission scanning electron microscopy (FESEM) and atomic force microscopy (AFM). Bulk chemical composition of films was measured by energy dispersive spectroscopy (EDS) during in FESEM observation. Phase identification was examined by X-ray diffraction (XRD). In case of amorphous structure, film crystallinity was again confirmed by transmission electron microscopy (TEM) and electron diffraction patterns (EDP). Focused ion beam field-emission scanning electron microscopy (FIB-FESEM) was employed for TEM sample preparation. Chemical composition and compound at/near film surface was investigated by X-ray photoelectron spectroscopy

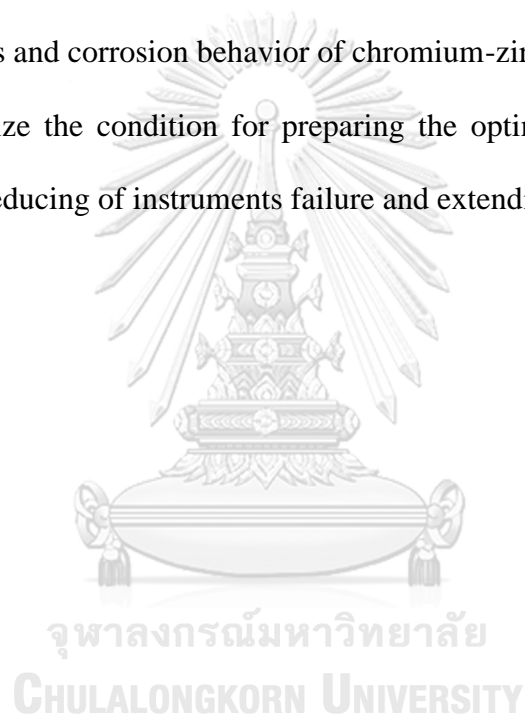
(XPS). Corrosion behavior was investigated by potentiodynamics and electrochemical impedance spectroscopy (EIS) in 3.5 %wt. NaCl solution at ambient temperature.

1.4 Expected or Anticipated Benefit Gain

1. Acknowledge effect of zirconium on phase evolution, physical properties and corrosion behavior of chromium-zirconium metallic films.

2. Acknowledge effect of zirconium content and interlayer on phase evolution, physical properties and corrosion behavior of chromium-zirconium nitride films.

3. Recognize the condition for preparing the optimize corrosion prevention film resulting in reducing of instruments failure and extending lifetime of service.



Chapter 2

Literature reviews

2.1 Corrosion in metals [33]

In nature, most of the thermodynamically stable phase of metals are formed in mineral compounds e.g. oxides, nitrides and sulfides. Thus, metals usually and spontaneously transform to their stable phases. Corrosion is one process which brings them to their stable forms. It could be categorized into many kinds of corrosion depending on the resulting damages, mechanisms and authors. Nevertheless, all corrosion forms must have these four necessary components: anodes, cathodes, electrolytes and electron paths.

- Anodes: these components are corroding and simultaneously produce free electrons for supporting corrosion reactions. Generally, these components are metals and perform as relatively negative potential.
- Cathodes: these components consume electrons from the anodes and produce/transform corrosion products. Thus, they are not corroded and relatively positive potentials with anodes.
- Electrolytes: they are mediums for ions/electrons migration.
- Electron paths: they are conductive components for electrons flow between cathodes and anodes. In some cases, it could be a corroding metal itself.

General reaction of corroding metals (anodes) and corrosion products (cathodes) are expressed in equation 2-1 and 2-2, respectively. In equation 2-1, solid

metal (M) emits electrons and becomes to metal ions (M^{n+}) resulting to weight loss and thinning. Simultaneously, oxidizer (R^{s+}) or cathode component consumes the electron from anodic reaction and becomes to the lower charge (R^t). Thereby, both reactions preform as each half-cell electrochemical reaction for corrosion process.



2.2 Thermodynamics of corrosion [33]

Because corrosion is chemical reactions, possibility and direction of reactions could be determined by thermodynamics. Reaction spontaneously forwards when the change of Gibb's free energy (ΔG) of reaction is negative and in vice versa. The relationship between ΔG and corrosion reaction could be expressed in term of electrochemical potential (E) as equation 2-3. Electrochemical potential occurred from the accumulation and depletion of electrons at anodes and cathodes, respectively. The n and F are number of equivalent exchanged electrons and Faraday's constant.

$$\Delta G = -nFE \quad (\text{equation 2-3})$$

$$E = e_a + e_c \quad (\text{equation 2-4})$$

Electrochemical potential (E) is the sum of half-cell electrode potentials of anode (e_a) and cathode (e_c) as shown in equation 2-4. Standard values of half-cell electrode potentials of the interesting metals are tabulated in the electromotive force (emf) series. The standard potentials in emf series could estimate stability of metals. The higher standard potential is a noble metal whereas the negative one is active metals (prefer corroding). Reactions in the emf series are usually written in the

reduction form; therefore, the sign of values in emf series must be remarked. Although thermodynamics could tell us about corrosion possibility and direction, it does not tell about how fast corrosion is.

2.3 Kinetics and corrosion measurement [33]

After understanding about thermodynamics of corrosion, kinetic of corrosion or corrosion rate is the other important information which must be considered. As previous discussion, corrosion composes of cathodic and anodic reaction which accomplish with electrons flow or exchanged current between them. Consequently, many investigations about corrosion rate base on determination of exchanged currents e.g. potentiodynamic polarization and electrochemical impedance spectroscopy (EIS).

2.3.1 Potentiodynamic polarization

Potentiodynamic polarization is a popular, convenient method for determine corrosion behavior and corrosion rate. In this method, specimen is immersed in testing electrolytes and applied electrical potentials (voltages) for accelerating reactions. The instrument records data of applied electrical potentials (E_{app}) and responding current of specimen (I) during operation as shown in figure 2-1. For example, considering corrosion of metal (M) which immerses in an acid solution. Cathodic and anodic reaction is expressed in equation 2-5 and 2-6, respectively. Because both reactions simultaneously occur at the same surface, each reaction relates on the other. The potentials, at cathodic and anodic currents are equilibrium, is described to corrosion potentials (E_{corr}). It normally locates between the half-cell potentials of metal M (e_{M/M^+}) and acids (e_{H^+/H_2}). Current density at E_{corr} is called as corrosion current

density (I_{corr}). Generally, the higher E_{corr} implies to the higher degree of corrosion resistance and the lower I_{corr} represents to lower corrosion rate.

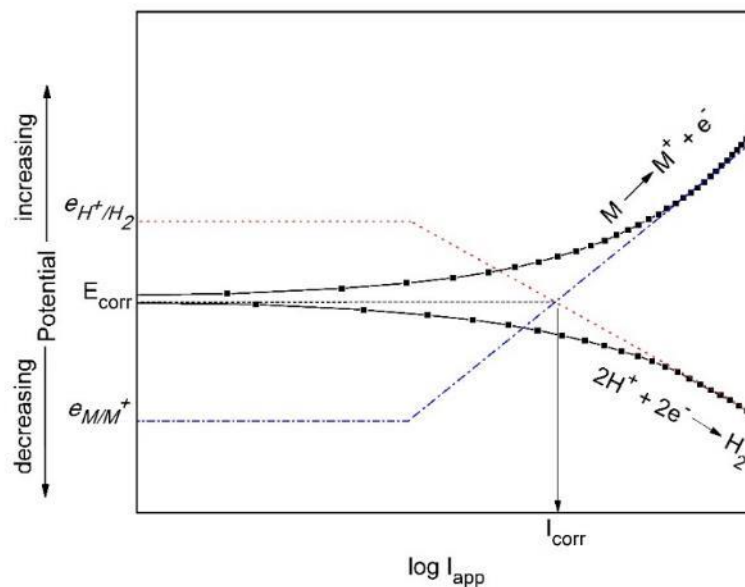


Figure 2-1 Potentiodynamic polarization curve

2.3.2 Electrochemical impedance spectroscopy

Electrochemical impedance spectroscopy (EIS) is an interesting non-destructive testing (NDT) technique which could distinguish corrosion at different interfaces. Therefore, it has been widely employed for corrosion investigations especially using for coating specimens. Because corrosion resistance of materials could be considered as ability to restrict electrical flow, measurement of only resistance might not represent to the whole corrosion behavior. Thus, EIS measurement has gained a lot of attends for corrosion investigation. It measures impedance (Z) of specimen by applied sinusoidal alternating current (AC) potential and records responding current through specimen at various frequency. Potential ($E(t)$)

and current ($I_{(t)}$) as a function of time (t) are expressed in equation 2-7 and 2-8, respectively. Herein, the E_0 and I_0 are amplitude of potential and current signal. The ω is a radial frequency which equals $2\pi f$; f is frequency and expressed in hertz. The Φ is a phase shift between current and potential signal, j is an imaginary number ($\sqrt{-1}$).

$$E_{(t)} = E_0 \exp(j\omega t) \quad (\text{equation 2-7})$$

$$I_{(t)} = I_0 \exp(j\omega t - \Phi) \quad (\text{equation 2-8})$$

Impedance with a function of time ($Z_{(\omega)}$) is defined in equation 2-9. It is also expressed as equation 2-10 by substitution with equation 2-7 and 2-8. It reveals that total impedance composes of real (Z_{re}) and imaginary (Z_{im}) part. The EIS instrument records data of potential, responding current, frequency and calculate to impedance during measurement. Typically, the EIS result or frequency respond analysis (FRA) could present in 2 forms of Nyquist plot and Bode plot which will describe in the further topics.

$$Z_{(\omega)} = E_{(t)} / I_{(t)} \quad (\text{equation 2-9})$$

$$Z_{(\omega)} = Z_0 \exp(j\Phi) = Z_{re} + jZ_{im} \quad (\text{equation 2-10})$$

2.3.2.1 Nyquist plot

Nyquist plot is one kind to present the EIS result. It displays the real impedance on x-axis and imaginary part on y-axis. Example of Nyquist plot for coating sample is shown in figure 2-2. In this plot, real and imaginary impedance could be considered as a vector. As a result, the value of impedance or impedance modulus ($|Z|$) at a certain frequency is a resultant vector of Z_{re} crossing with Z_{im} . Though this plot does not display frequency on the axis, frequency could be estimated by the lower frequency staying on the left side of plot. Angle between the resultant

vector and x-axis is a phase shift between potential and responding current. Generally, the large semi-arc or semicircle implies to the high anti-corrosion property.

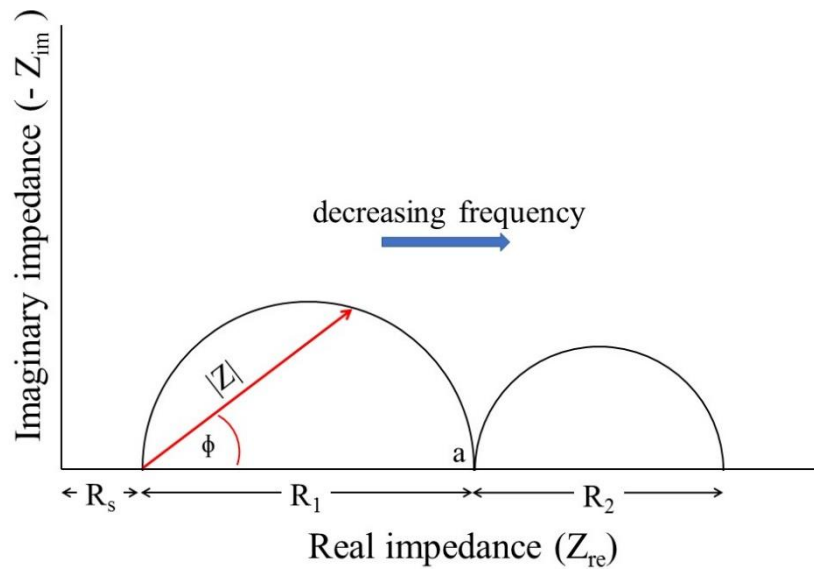


Figure 2-2 Example of Nyquist plot

2.3.2.2 Bode plot

Bode plot is the other popular form to present the EIS data, and could be categorized into two subplots. In case of a plot of logarithm frequency versus impedance modulus ($|Z|$), it is called as Bode modulus plot. The plot of frequency and phase shift (Φ) is call Bode phase. The example of bode plot, which accords to Nyquist plot in figure 2-2, is shown in figure 2-3. The higher and wider phase shift peak in Bode phase attributed to the higher degree of anti-corrosion.

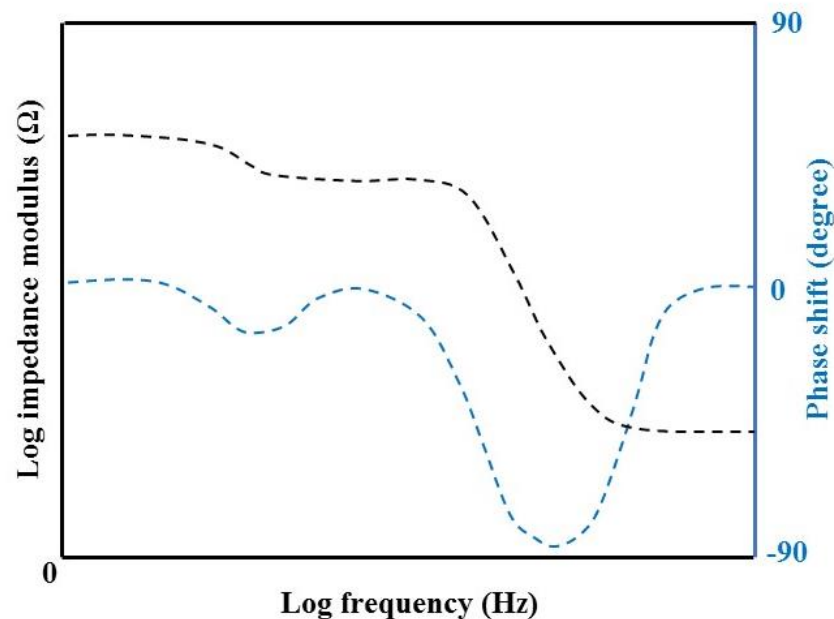


Figure 2-3 Bode plot of coating specimen

2.3.2.3 Interpretation of EIS

Even the EIS result could be roughly estimated corrosion behavior by the Nyquist and Bode plot, the result should be fitted and interpreted to equivalent circuit elements (ECs) for more information. The common equivalent circuit elements, which are usually used for fitting EIS result, include resistor, capacitor, inductor and Warburg impedance. Relations between impedance and phase shift of those are shown in table 2-1. The example equivalent circuit elements model, which well fits with the figure 2-3 and 2-4, is shown in figure 2-5. This circuit consists of 3 resistors and 2 capacitors according to the physical model of film specimen and corrosion at two interfaces. At high frequency, total impedance of this model is approximately solution resistance (R_s) as seen by constantly impedance without phase shift. When decreasing frequency, impedance of film dielectric property (C_1) increases resulting to the formation of semicircles arc in Nyquist plot, increasing of $\log |Z|$ and decreasing

phase shift. The interception at x-axis (point a) in Nyquist plot is equivalent to the sum of real impedance of solution and coating resistance (R_1). Because of degrading film during testing or pre-existing crack, some solution could penetrate through film and corrode at substrate interface. This phenomenon could be considered as current which passes over R_1 to the small circuit. The corrosion phenomenon at this interface could be explained by this small circuit consisting of capacitor of double layer (C_2) in a parallel with charge transfer resistance (R_2).

Table 2-1 Relationship of equivalent circuits to impedance and phase shift

Equivalent circles	Impedance	Phase shift (ϕ , degree)
Resistors	R_i	0
Capacitors	$-j/\omega C_i$	-90°
Inductors	$j\omega L_i$	90°
Warburg impedance	-	-

* R_i , C_i and L_i are resistance, capacitance and inductance of component i, respectively

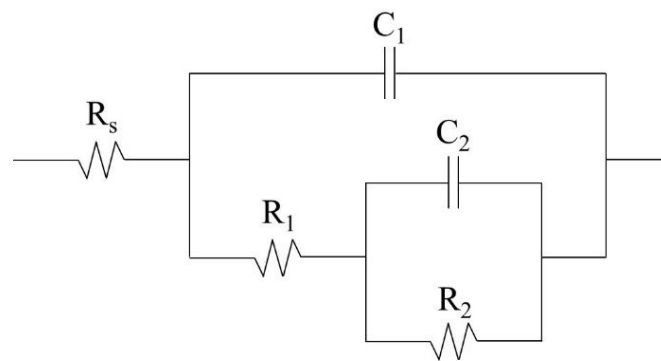
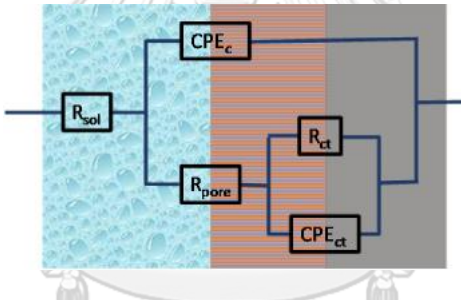
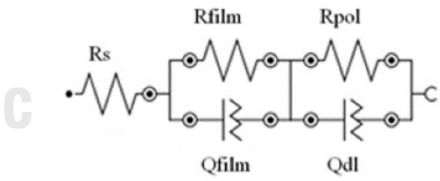


Figure 2-4 Equivalent circuits model of coating specimen

The interpretation of EIS result for film specimens have reported in many equivalent circuit models [34-36]. The example models, which have been widely used for explaining about corrosion behavior, are shown in table 2-2. The model of $[R_s([R_{film}(R_{ct}Q_{ct})]Q_{film})]$ was the popular model which provided the good chi-squared

and explanation of corrosion in coating specimens [37-39]. This circuit based on films having some pre-defects/cracks before corrosion testing. These cracks played as a direction for corrosion penetration leading to corrosion under coating. Thus, corrosion could simultaneously occur at solution/film interface and film/substrate interface. The other model is $[R_s(R_{film}Q_{film})(R_{ct}Q_{ct})]$. This model is often used in dense or pore/crack-free film [40, 41]. Thus, solution, which is considered as current, must pass through film circuit (Q_{film} and R_{film}) before reaching and corroding at film/substrate interface.

Table 2-2 The popular equivalent circuit models for film specimens

Circuit description	Circuit model	Authors
$[R([R(RQ)]Q)]$		The (Ti,Cr)O films reported by A. Bahrami <i>et al.</i> [34]
$[R(RQ)(RQ)]$		The poly(urea-formaldehyde) films by A.G. Cordeiro <i>et al.</i> [40].

2.4 Forms of corrosion in metals and metal alloys

After understanding about thermodynamics, corrosion rate and corrosion investigations, form of corrosions is another key information which should be considered and understood. Typically, corrosion in metals and metal alloys are categorized by attack mechanisms, resulting damages and authors. Each form has unique characters which lead to the different resulting damages and failures. Thus, it

is necessary to understand about corrosion forms for identification, prevention and control those corrosions. The importance forms of corrosion are listed and briefly described in the next sections.

2.4.1 Uniform corrosion

Uniform corrosion is a generally corrosion form which occurs on metals surface and mainly causes metal thinning. However, it is a preferential corrosion form because it is easy to inspection and prediction about the lifetime of services. Generally, it has more possibility to take place when corroding materials and environment are homogeneous. In addition, it was reported that nanocrystalline or amorphous materials have more tendency to corroded in uniform corrosion mode [42-44]. In the case of crystalline materials, grain boundary is a weak point for corrosion in comparison with inside grain. As result, corrosion preferentially occur at grain boundaries leading to pitting corrosion. In the case of nanocrystalline, they have higher number of grain boundaries and small distance between them. As resulting to corrosion takes place with more homogeneous and throughout the entire surface. Therefore, nanocrystalline have higher tendency to corrode in uniform corrosion mode [42, 43]. In term of amorphous materials, corrosion homogeneously occurs over surface (uniform mode) due to lacking of grain boundary or weak points [44].

2.4.2 Galvanic corrosion

Galvanic corrosion usually occurs at junction between two dissimilar metals when they are coupled with presence of electrolytes. One of them is corroded (anodes) while the other is protected (cathodes). Corroding metals could be predicted by Galvanic series or standard potential electromotive force (emf) series. The lower

galvanic potential or standard potential in emf series is preferentially corroded. Corrosion rate depends on the different potential and area of cathodes/anodes. The similar potential and small area of cathodes (comparing with anode) minimize corrosion rate.

2.4.3 Dealloying

Dealloying is a phenomenon of corroding especially alloying elements due to the lower electrochemical potentials (like galvanic corrosion). It caused to the losing of alloying elements in specimens which may affect to their strength and mechanical properties. It could be both localized and uniform corrosion depended on the distribution of alloying elements. However, localized attack is more serious damages leading to penetration in specimens.

2.4.4 Crevice corrosion

Crevice is also a localized corrosion attack which usually occurs under covers or in cavity/cracks in presence with electrolyte. Covers could be plastic, sand, metals even though their own passive films. It could occur simultaneously with galvanic corrosion leading to heavily corrosion in some cases. Because crevice corrosion occurs in cavity or small area, corrosion products (metal ions and anions) are restricted to transport away from crevice site. This leads to build up of their concentrations and rapidly corrosion. These damages hard to detection and rapidly penetrate leading to unpre-dicting failure.

2.4.5 Pitting corrosion

Pitting corrosion is a localized attack liked crevice corrosion however it could create pits by itself. It also restricted the transport of ions throughout and built up the concentration in the pits. Hence, corrosion rate in the pits is higher than on the surface and resulting to rapidly penetration. These pits might be deep, subsurface, undercut or horizontal. They could be the initial point for crack propagation and failure. Unfortunately, pits at the surface are typically small and hard to detection. Hence, corrosion preventions are needed for reducing the risk of failures.

2.5 Corrosion prevention

As previous topics, corrosion could damage metals or metal alloys, decreases lifetime of services and increases risk for failures. Hence, the corrosion prevention should be considered. It could be done by several methods depending on operation conditions. The popular corrosion preventions are listed in the next sections.

2.5.1 Environment modifications and materials selection

From essential of corrosion, it is chemical interactions between metals and their environments for stabilized those metals to equilibrium states in the environment. Some metals are immune under some certain environment conditions. Therefore, modification or monitoring the environments to suitable conditions is a way for prevention. Unfortunately, environment modifications are not practical or hardly control in some cases. Thus, materials selection is more preferential method for extending lifetime of services or preventing corrosion. It is more convenient in practical and easier than environment control/modification.

2.5.2 Cathodic protection and sacrificial anode

Cathodic protection and sacrificial anode are another method for corrosion preventions which have been widely used in many industrials like oils and gases. Both methods base on the same fundamental that corroding metals produce electrons. In the reverse way, we could prevent corrosion by supply external electrons to our metals. The key difference of cathodic protection and sacrificial anodes is the source of supplying electrons. The cathodic protection applied external currents to supporting metals specimens, whereas sacrificial anode provided electrons by corroding itself (based on galvanic corrosion). Therefore, the sacrificial metals must be lower standard potential in emf series, or more active.

2.5.3 Painting

Painting is a general method for corrosion prevention in daily life. It is easy, convenience and cheap for corrosion prevention. Insulators or low conductivity paint layers cover on the metal interfaces for restricting electrons flow and separating metals from corroding environments. However, most of paints are polymers which degraded at relatively low temperature and poorly mechanical properties. Therefore, this method is limited to use in low temperature and mechanical load.

2.5.4 Coating

Like painting, coating bases on the same fundamental which separates metals from their environments. However, this method could deposit more kind of materials than painting especially ceramic or amorphous materials. These materials are well known about the high corrosion resistance, good mechanical property and operating in evacuate temperature. Therefore, this method could prepare prevention layers for

wide operating conditions, portable specimens, and no require of material or environment control.

From the list of corrosion preventions, coating is a good, interesting candidate for prepare an anti-corrosion film. Researchers decided to use this method for preparing anti-corrosion films as previous description. In addition, an ability of corrosion prevention of this method strongly depends on coating materials. The kind of materials will be discussed in the next section.

2.6 Coating materials

As previous mentions, an ability of corrosion prevention of coating method strongly depends on coating materials. Typically, coating materials could be categorized into 2 main types including metallic and ceramic coating. Selection of materials depends on using applications and limitations such as hardness, cost, repairability, appearance etc. Metallic coating usually operates at low temperature and mechanical load while ceramic coating could operate with higher temperature and load.

2.6.1 Chromium

Chromium (Cr) is an outstanding material which has been using as corrosion prevention film due to its corrosion resistance and self-healing protective passive layer. Not only a good anti-corrosion property, it also has an economic reasonable and good appearance. Thus, it also has been widely used in many applications. However, it still has some limitations such as using in saline and reduction environment. Many researchers have developed and tailored its properties for enhancement of corrosion resistance [1-4]. Controlling crystallinity of chromium film to amorphous structure is

an outstanding technique for achieving an excellent corrosion resistance property. Amorphous materials tended to be more tolerant to corrosion than crystalline materials in the same compositions [4-6]. It was also reported that amorphous structure successfully inhibited pit formation which was the main root cause of passive film failure [7, 8].

To achieving amorphous structure in chromium film, material design by addition or alloying with other elements is an interesting method. It simultaneously provided a good corrosion resistance and showed a tendency of amorphous formation [15]. Several metal-metal binary systems has been investigated and developed by many research groups for preparing high corrosion resistance alloys e.g. K. Hashimoto (1993), D. Landolt (1998), M. Kitada (2005), B. Mallia (2007), D.P. Wang (2012), H. Skliarova (2015) and J. D. Schuler (2017) [2, 6, 9-13]. Zirconium is one of outstanding metals for combination with chromium to provide amorphous coating. It has been reported that it tended to decrease degree of crystallinity or promote an amorphization in several alloy systems, given a high corrosion and specific strength [13, 14]. Therefore, researchers have been interested to prepare amorphous chromium-zirconium film for anti-corrosion application.

From the atomic size differences (δ) calculation as expressed in equation 2-11 and 2-12 [45-47], binary system of chromium-zirconium had a tendency of amorphization in the moderate composition range as shown in figure 2-5. Amorphous film of zirconium-based prepared by DC magnetron sputtering was probably found when $\delta > 8.9$, and the high δ favored to amorphous formation [47]. Therefore, this research aimed to preparing the moderate composition of chromium-zirconium alloy for achieving amorphous film.

$$\delta = 100 \sqrt{\sum_{i=1}^n C_i \left(1 - \frac{r_i}{r}\right)^2} \quad (\text{equation 2-11})$$

$$r = \sum_{i=1}^n C_i r_i \quad (\text{equation 2-12})$$

The n , C_i , r_i and r are the number of components, atomic percentage (%at.) of i component, atomic radius of i and the average atomic radius, respectively. For this calculation, the r_{Cr} and r_{Zr} are 1.28 and 1.60 pm; respectively [47].

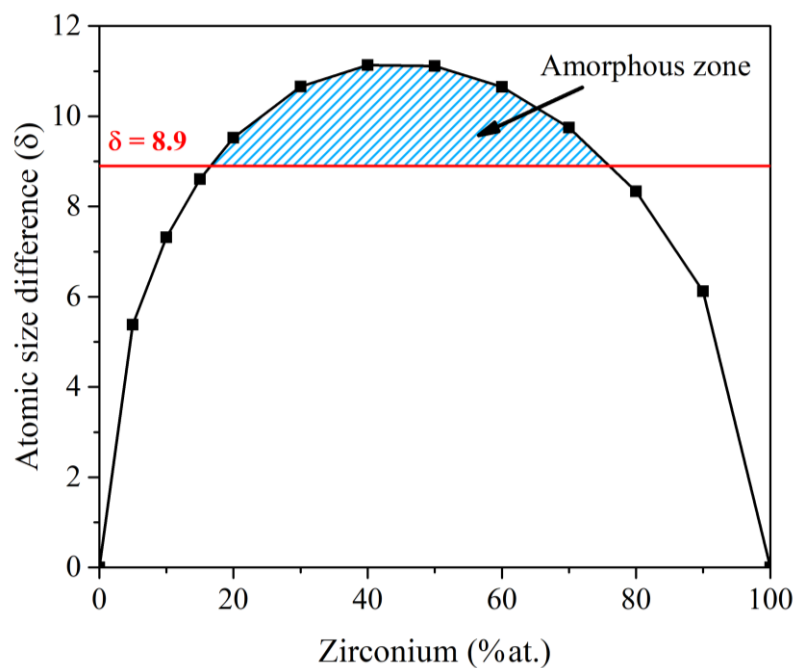


Figure 2-5 Relationship between atomic size differences (δ) and composition in chromium-zirconium system

2.6.2 Chromium nitride compounds

Not only using in metallic form, chromium was also used in form of ceramic coatings. Chromium nitride is a kind of ceramics which has been widely used in many applications including corrosion prevention layers [21, 25, 48-51]. It had higher hardness and corrosion resistance than a commercial AISI 304 stainless steels in both of 1 N H_2SO_4 and 3.5 %wt. NaCl solution [21, 51, 52]. Potentiodynamic curves of

CrN coating and AISI304 is shown in figure 2-6. Generally, chromium nitride has two polymorphous of chromium nitride (CrN, space group 225, $a_0 = 4.1490 \text{ \AA}$) and dichromium nitride (Cr_2N , space group 162, $a_0 = 4.8114 \text{ \AA}$) as seen in phase diagram of Cr-N (figure 2-7). The CrN was the higher corrosion resistance phase and was preferred for anti-corrosion application whereas the Cr_2N was the high hardness [23, 48, 50]. S. Ahn *et al.*, who compared the CrN and Cr_2N films on H13 steels, reported that the CrN film had lower corrosion current density (in 3.5 %wt. NaCl solution) and denser than Cr_2N film [23].

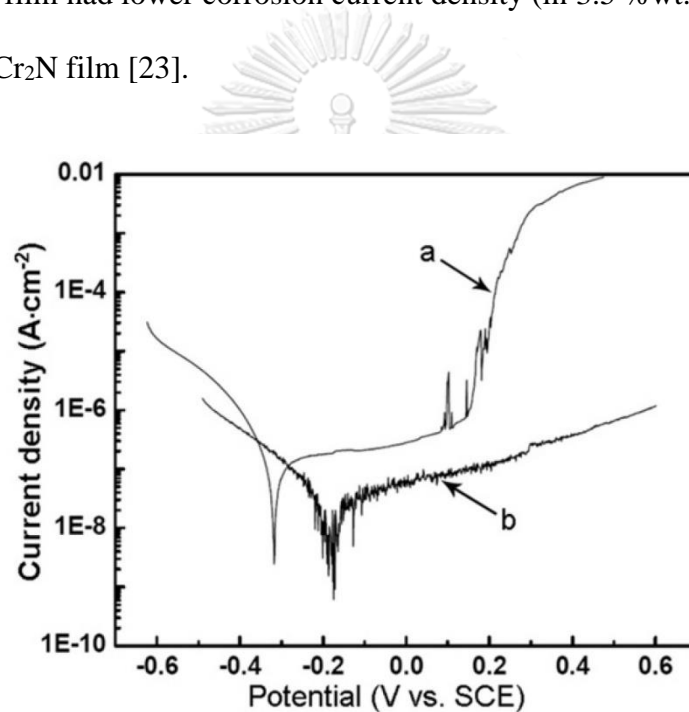


Figure 2-6 Potentiodynamic polarization curves of (a) AISI 304 stainless steels and (b) CrN coating

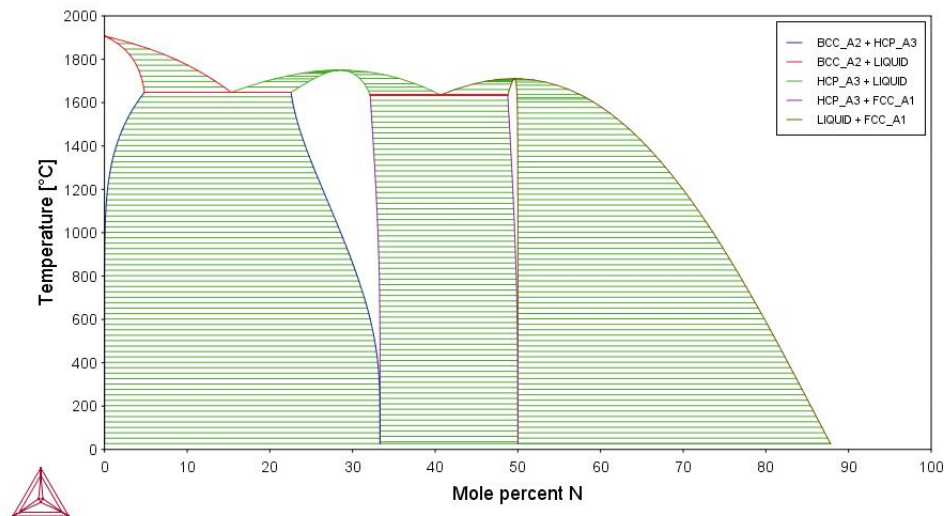


Figure 2-7 Binary phases diagram of chromium-nitrogen

Furthermore, it has been reported that the corrosion resistance of CrN film could be improved by addition of third transition metal into CrN film. Zirconium also demonstrated as good candidate for apply into CrN as well as in form of metallic. Many researchers reported that addition of zirconium into the CrN films improved corrosion resistance, wear, hardness and reduced surface roughness, grain sizes, corrosion rates [25, 27, 53, 54]. Interestingly, the higher zirconium addition tended to reduce crystallite size of complex nitride of chromium-zirconium, (Cr,Zr)N [55]. According to P. Sukkul and R. Chaithammapakorn report [56], the large of zirconium addition promoted the broaden peak in XRD result (figure 2-8) which implied to a poorly crystalline structure. As our objectives, amorphous films are expected in this research because they have high corrosion resistances and possible to corrode in uniform corrosion. Researchers also aimed to investigating the effect of zirconium on phase evolution (amorphization) and corrosion behavior of the CrZrN films.

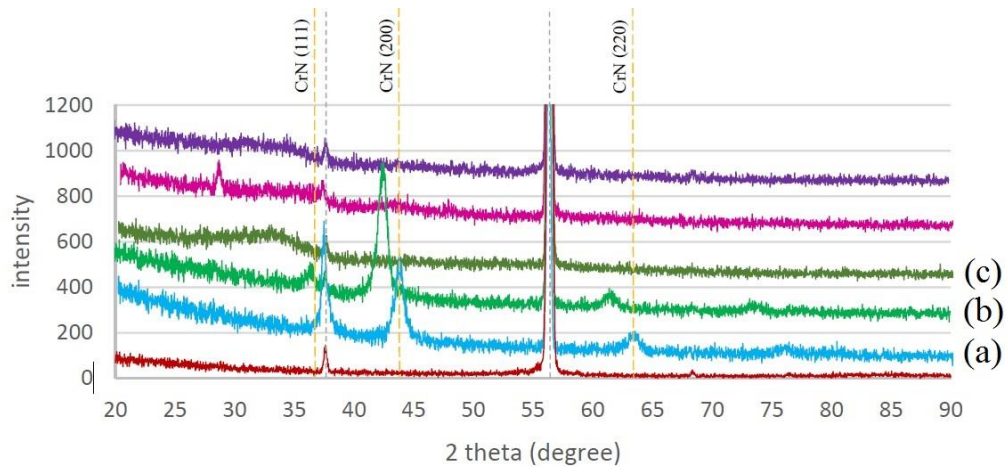


Figure 2-8 XRD patterns of CrZrN films: (a) (Cr-rich)N, (b) (Cr-Zr)N and (c) (Zr-rich)N

2.7 Coating methods

Coating were fabricated by many processes such as sol-gel spin coating, chemical vapor deposition (CVD) and physical vapor deposition (PVD) etc. [20, 29, 30]. Generally, selection of coating methods depends on coating materials, substrates and proposes of preparations. Magnetron sputtering is an outstanding PVD method for using in this research because it is convenient, reliable and could deposit many kinds of materials on many substrates including metallic, ceramic or amorphous films. Therefore, it could prepare both of metallic and nitride film of chromium-zirconium, and has potential for fabricating amorphous films.

2.7.1 Magnetron sputtering

Generally, magnetron sputtering composes with four important parts: targets (deposit materials), substrates, working gases and reactive gases. The schematic of co-magnetron sputtering chamber is shown in figure 2-9. Operation starts with chamber evacuation to base pressure, subsequently introduce working gas (usually Ar)

with/without reactive gas into chamber. Then, apply current to target (deposit materials) whereas anode (substrates holder) is grounded or bias. As a result, working gas between them discharges to positive ion (Ar^+) and strikes to target and ejection of target atoms. Those atoms deposit on substrates and/or react with reactive gas. Thus, it could fabricated both of chromium-zirconium metallic and nitride films by co-sputtering of chromium and zirconium [27, 55]. Properties of resulted film depend on operating conditions such as working pressure, applied current etc. Therefore, film properties could be designed and controlled by adjustment of instrumental parameters.

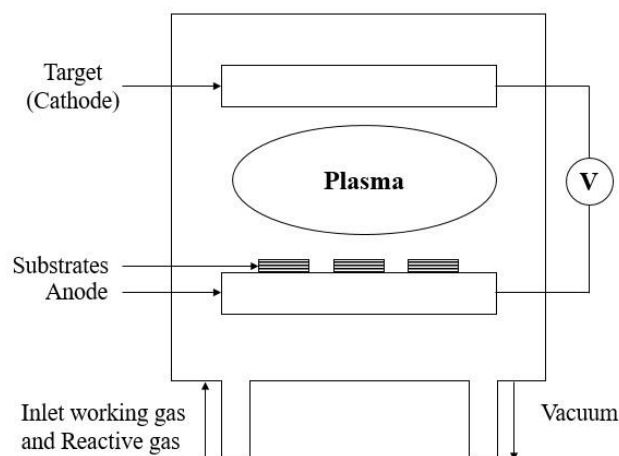


Figure 2-9 Schematic of reactive magnetron sputtering chamber

2.7.1.1 Instrumental parameters of magnetron sputtering

Achievement and controllable of films morphology, it must understand about instrumental parameters because those parameters affect to films formation and their properties. The important instrumental parameters of reactive magnetron sputtering compose with working pressure, partial pressure of reactive gas, applied current, substrates temperature. These parameters relate to energy and mobility of sputtered atoms which affect to film's morphology and microstructure.

Working pressure is an operating pressure during sputtering process. Pressure affects to adatoms mobility in term of their initially energy before approaching substrates. The high pressure increases number of atoms collision leading to sputtered atoms lose their energy. As result, adatoms have low mobility and probably form metastable phase or amorphous. In addition, L. Meng and M.P. Santos revealed amount of TiO₂ amorphous increased with higher working pressure [57]. However, over pressure might cause the unstable of plasma, thus pressure should be balanced.

Like working pressure, partial pressure of reactive gas gives similar effect to adatoms. However, it has another importance effect about an over of partial pressure of reactive gas. It causes formation of compounds on surface targets (poisoning target) leading to lower sputtering yield and non-stoichiometric of the resulted films. In the case of CrN and Cr₂N films preparation, the partial pressure of N₂ (reactive gas) also affected to film formation, amounts of CrN phase in film increased with the higher partial pressure of N₂ [22, 23, 50].

Applied current is an electrical current which supports target materials for generating negative potential. It excites a working gas to positive ions (at suitable pressure) resulting to striking of those ions at the target materials (negative potential) and emitting of target atoms. The higher applied current increases a sputtering yield and deposition rate.

Substrates temperature also affects to mobility of adatoms and film's morphology. High substrate temperature enhances energy and mobility of adatoms. As result, they could diffuse on substrates surface and seek sites for formation a stable phase. This thermal energy also increases possibility of recrystallization and grain

growth therefore it might promote equiaxed coarse grains [58]. Therefore, substrate temperature should be kept at low for restrict adatoms diffusion and inhibit crystalline formation.

2.7.1.2 Process modification

Not only adjustment of instrumental parameters but process modification also controls and affects to film's properties. It could be done in several ways e.g. multilayers coating or addition of interlayer. However, addition of interlayer is more an interesting method because it is powerful, less operating steps, could improve film's adhesion and corrosion resistance [59, 60].

Modification process by adding interlayer usually aims to tailoring above film's properties, reduces stress at interface junction (buffer layer) and improves adhesion between top film and substrate. The importance parameters, which should be considered about interlayer properties before using or selecting materials, composed of crystal structure, interfacial energy and wetting ability of substrates/interlayer and top layers/interlayer etc. The different or mismatched crystal structure, high-interfacial energy and wetting angle affects to film morphology in the similar way by adatoms favor to bond together than bond with substrates leading to form in island structure and become to balloon structure. Coarse balloon structure in films causes pores between roots of each balloon resulting to high porosity in film. In contrast, adatoms well bond with substrates and spread over substrates resulting to smooth surface and dense film when similar or matched crystal structure, low interfacial energy and wetting angle.

Furthermore, additional of interlayer has been reported that it could promote amorphous in top films [32]. Therefore, researchers are also interesting to investigate the effect of interlayer to the phase evolution of CrZrN films and possibility of amorphous films preparation.

Finally, there are several parameters which control film morphology and crystallinity as previous mention. For promoting amorphous films, it requires a low of substrate temperature and adatoms mobility for restrict diffusion process. Unfortunately, adjustment of applied current and partial pressure of reactive gas are normally limited by target materials, plasma stability even instruments. Promoting amorphization by additional of interlayers is more interesting and would be also employed in this research.

2.8 Concepts of research

Corrosion in metals is destructive reactions which bring a lot of problems to industrials and peoples e.g. instruments failure, costs of products and safety life etc. Therefore, corrosions prevention is always considered for extend the lifetime of services and make more safety operations. Coating with chromium-zirconium metallic film is the outstanding method for anti-corrosion due to the high corrosion resistance and self-healing passive layer. They also probably formed amorphous structure which provides a good anti-corrosion property. From the atomic size differences calculation, amorphization probably found in the moderate composition of chromium-zirconium binary system. Therefore, the moderate composition of chromium-zirconium was expected in this research for preparing amorphous film for using in anti-corrosion applications.

Not only using in metallic film, but chromium was also using in compound phases. Zirconium also demonstrated as a good candidate for apply to CrN. It has been reported that a slightly addition of zirconium into chromium nitride could improve corrosion resistance and hardness of CrZrN films. In addition, fine crystal structure was reported in this ternary system and amorphous structure probably found with the higher zirconium content. Therefore, researchers also aimed to investigate the effect of zirconium addition in large contents to phase evolution and possibility of amorphous formation as well as in the metallic films.

From the industrial point of view, plasma ignition in nitride film fabrication usually starts with only argon gas for preventing poisoning target and maintaining plasma stability. The metallic interlayer usually presents between nitride film and substrates. From literature review, the amorphous interlayer could promote amorphization of top nitride film. Researchers also aim to add amorphous interlayer for promoting amorphization in top CrZrN, and investigate it's effect as well.

Chapter 3

Metallic film of chromium-zirconium

3.1 Chromium-zirconium film

As previous description, this research could be divided into 2 main parts including metallic film and nitride film. It will start with chromium-zirconium metallic film part. Metallic films were categorized into 3 groups: pure chromium (Cr-film), pure zirconium (Zr-film) and mixture of chromium-zirconium (CrZr-film). All films were deposited on a disk-shape polished AISI H13 steel and (100) silicon wafer by magnetron co-sputtering of chromium and zirconium targets. Details of films preparation will be showed in the next content.

3.2 Film preparation and characterizations

3.2.1 Film preparation

Sample preparation, instruments, methods and characterizations are the importance information which directly affect to the experimental results. Therefore, these details must be clearly showed and explained. A heat-treated AISI H13 steel was cut into a dish-shape with a diameter of 25.4 mm and 2.0 mm in thickness. Those dish-shape H13 substrates were polished with a series of emery SiC papers and finishing with 1 μm diamond-suspended paste. Detail of H13 substrate preparation and heat treatment are shown in appendix A-1.

Before film deposition, substrates were cleaned ultrasonically in industrial-grade acetone. Three kind of films were prepared using a dual-head DC magnetron sputtering device with pure chromium and zirconium targets (99.95% pure, Lesker).

Prior to the deposition process, the chamber was evacuated to 9.9×10^{-4} Pa (7.5×10^{-6} Torr) as the base pressure. High-purity Ar gas (99.995% pure, Linde) was introduced at a flow rate of 20 sccm to obtain a working pressure of 0.39 Pa (3.0×10^{-3} torr). To apply an identical plasma voltage, the electrical power supplied to the chromium and zirconium targets were 100 W and 150 W. Therefore, a plasma current of zirconium target (0.50 A) was apparently higher than that of chromium target (0.31 A). During the process, the substrate holder was rotated at a speed of 4 rpm to achieve uniform thickness. All deposition processes were done without auxiliary heater and bias voltages. The temperature of the specimen was monitored using a K-type thermocouple inserted into substrate holder. All deposition parameters are listed in table 3-1. For a pure metallic chromium and zirconium, each corresponding target was ignited. On the other hand, both targets were simultaneously used for co-sputtering of a mixed chromium-zirconium film. For convenience, henceforth, the sputtering conditions will be named Cr-film, Zr-film and CrZr-film, respectively.

Table 3-1 Details of deposition parameters

Deposition parameters	Coating samples		
	Cr-film	Zr-film	CrZr-film
Working gas	Argon (99.995% purity)		
Based pressure	9.9×10^{-4} Pa		
Working pressure	0.39 Pa		
Target-sample distance	130 mm		
Substrate temperature	318-333 K		
Rotating speed	4 rpm		
Target; power/current/voltage	Cr; 100W/0.3A/320V	Zr; 150W/0.5A/306V	Cr;100W/0.3A/327V Zr;150W/0.5A/306V
Deposition time	1200 seconds (20 minutes)	600 seconds (10 minutes)	600 seconds (10 minutes)

3.2.2 Material characterizations

Surface morphology of films was firstly examined by a JEOL, JSM-7100F field-emission scanning electron microscope (FESEM) equipped with an Oxford Inca PentaFETx3 energy dispersion spectroscope (EDS) for determining bulk chemical composition. The thickness of films was measured by FESEM images using Image J software. A Veeco Dimension 3100 atomic force microscope (AFM) was used to estimate surface roughness with a scanning area of $5 \times 5 \mu\text{m}^2$.

Phase identification was performed using a Rigaku D/Max 2200P/C glancing incident angle X-ray diffractometer (GIXRD) with a $\text{Cu-K}\alpha$ source at an incident angle of 3 degrees. A focused ion beam field emission scanning electron microscope (FIB-FESEM) model Versa, FEI was used for transmission electron microscope (TEM) sample preparation. High-resolution transmission electron images (HRTEM) and electron diffraction patterns (EDP) were obtained to confirm phase and crystallinity by using a JEOL model JEM 2100.

3.2.3 Corrosion behavior analysis

The electrochemical behavior was investigated by using a Metrohm PGSTAT 302N Potentiostat/Galvanostat with three-electrode cells containing a 3.5 weight percentage (% wt.) NaCl solution at a volume of 100 cm^3 . The tests were conducted at room temperature using an Ag/AgCl electrode performed as a reference electrode (RE), a platinum rod as a counter electrode (CE) and the specimen with the exposed surface area of 1.0 cm^2 as a working electrode (WE). Firstly, the open circuit potential (OCP) was measured after immersion of a specimen into the solution for 1200 seconds. Subsequently, electrochemical impedance spectroscopy (EIS) was employed

to evaluate the response in a frequency range of 100 kHz and 10 mHz with a 1 mV amplitude AC perturbation signal. The equivalent circuit models were fitted and interpreted with NOVA 1.11 software with the standard deviations about 1 to 5×10^{-2} . Afterward, potentiodynamic polarization was performed at -500 mV with respect to their OCP values and finished at +1200 mV or current limitation (10^{-2} A/cm²). Step potential and scan rate were 1 mV and 1 mV/s, respectively. Corrosion potential (E_{corr}), corrosion current density (I_{corr}), Tafel's constant (β_a , β_c) and polarization resistance (R_p) were calculated using Tafel's extrapolation and a Stern-Geary equation provided in Nova 1.11 software. The polarization resistances (R_p) were calculated according to the equation: $R_p = \beta_a \beta_c / 2.3 I_{\text{corr}} (\beta_a + \beta_c)$ [33, 61]. To check reproducibility, at least 3 specimens for each deposition condition were used for the corrosion tests. The Tafel regions ± 50 mV with respect to the tip of the curves were selected for further evaluation. The range of standard deviations for potentiodynamic polarization was less than 1×10^{-15} . The surface morphology of corroding specimens was again observed by SEM for investigating about corrosion failure in each film. The passivated films were further analyzed with a Shimadzu Amicus X-ray photoelectron spectrometer (XPS) using a Mg-K α line as the chemical composition and oxidation states. Phase evolution of the passive layer was investigated by comparing the XPS spectra at different positions from the surface. This was done with an Ar sputtering system (30 mA emission current, 0.5 kV beam voltage) for 2 seconds prior to successive XPS measurement; the cycle was repeated 5 times.

3.3 Results and discussions

3.3.1 Microstructure and morphology

Results and discussions were started with microstructure and morphology observation. FESEM images revealed that magnetron co-sputtering successfully fabricated all films with uniform thickness as shown in figure 3-1. Deposition rate of Cr-film, Zr-film and CrZr-film was 22.4, 38.9 and 43.8 nm/min; respectively, measured by Image J software. For achieving comparative thickness, therefore, deposition time of Cr-film was increased to 20 minutes while others were 10 minutes. The Cr-film exhibited fine columnar structure in cross sectional with average columnar width 22.1 nm, and flake structure with some voids on surface as shown figure 3-1(a) and 1(b). This was a typical morphology of sputtered chromium film and the presence of voids in chromium film was explained by self-shadowing effect [62, 63]. In the case of Zr-film, FESEM images showed relatively coarse V-shape columnar structure with nodular structure on surface morphology. Herein, the correlation between cross-sectional V-shape columns and surface nodules could be clearly seen. This microstructure was from competitive growth during film formation due to the high applied voltages. The structure of pure chromium and zirconium film were classified to Thornton's structure zone model (SZM) in zone I and T, respectively [64]. On the contrary, as illustrated in figure 3-1(e) and 1(f), the binary alloy of CrZr-film had featureless cross sections with smooth surfaces which it was suggested be due to a low degree of crystallinity or amorphousness [65]. The featureless of this film was also confirmed by the TEM images as shown in figure 3-2.

Nevertheless, phase and crystallinity of films will be again discussed in more details using XRD, HRTEM and EDP results in the following section.

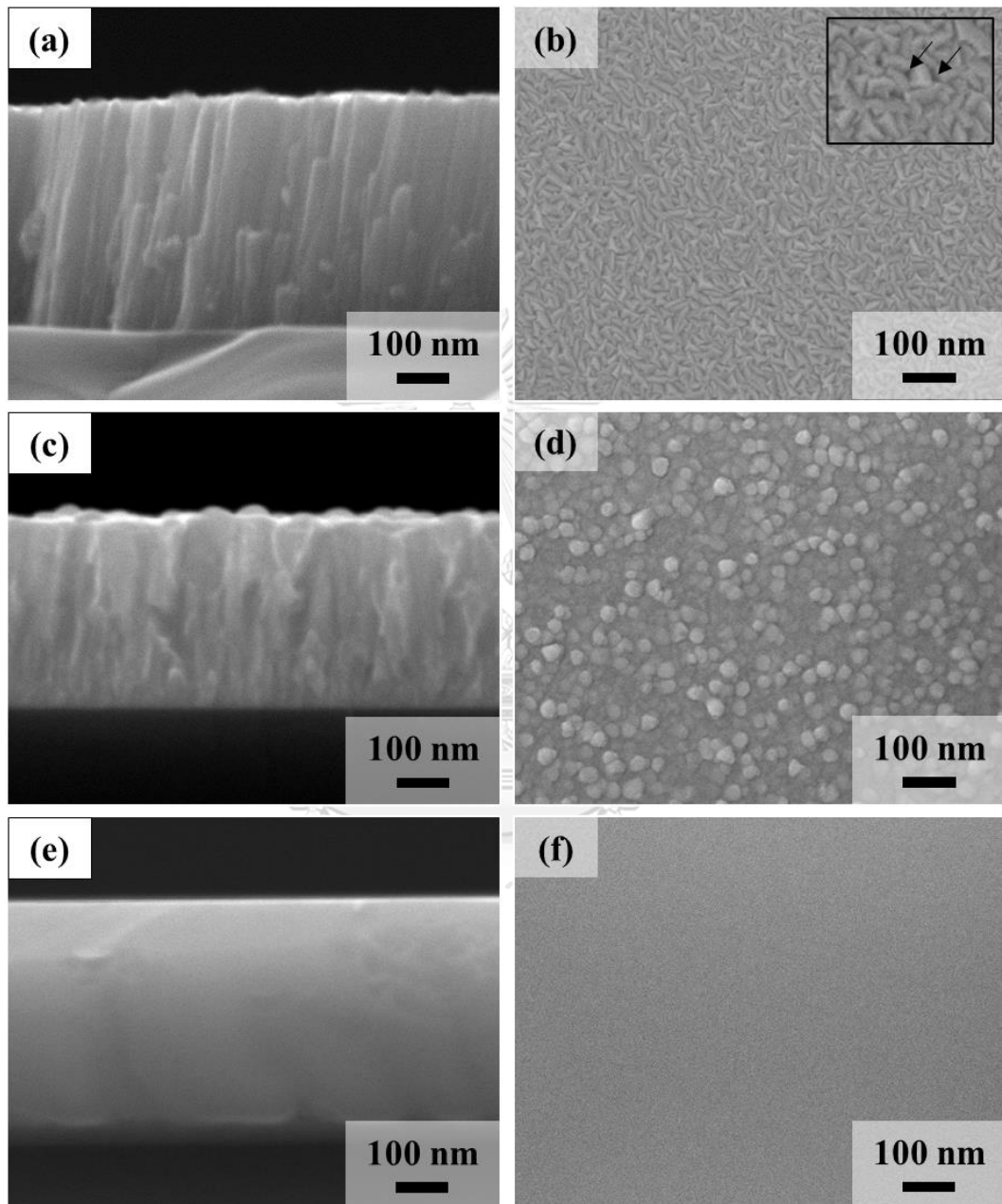


Figure 3-1 FESEM images of metallic films (a) - (b) Cr-film, (c) - (d) Zr-film and (e) - (f) CrZr-film

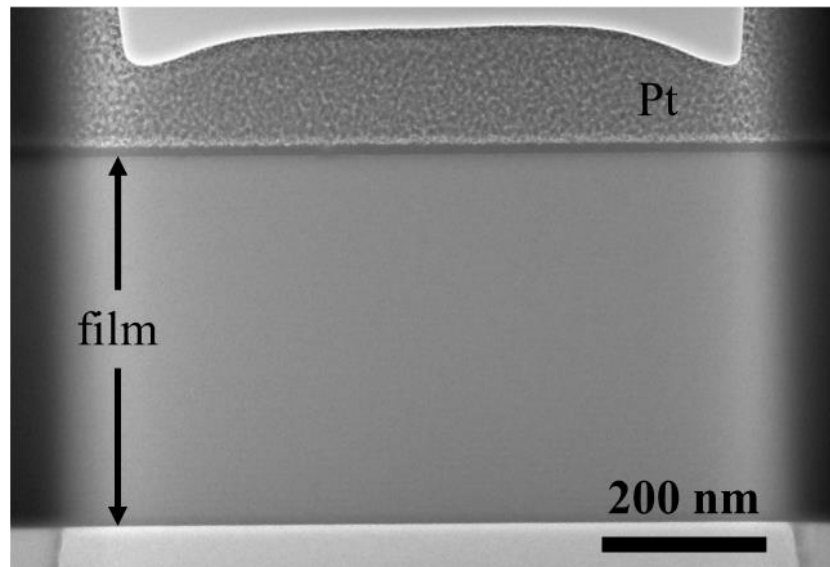


Figure 3-2 TEM images of the FIB specimen of CrZr-film

Topographic images of films by AFM are shown in figure 3-3. The result well correlated with the previous FESEM images and film morphology. All films exhibited smooth surface in a nanoscale as listed in table 3-1. The Zr-film showed the highest average surface roughness (R_a) according to its microstructure, the coarser columnar attributed to a rougher surface [64]. Nonetheless, several reports revealed that the effect of surface roughness on corrosion properties was weakened with smoother surface. The R_a in nanoscale was insignificant and could be negligible [66-68]. Therefore, the effect of surface roughness was negligible in this research.

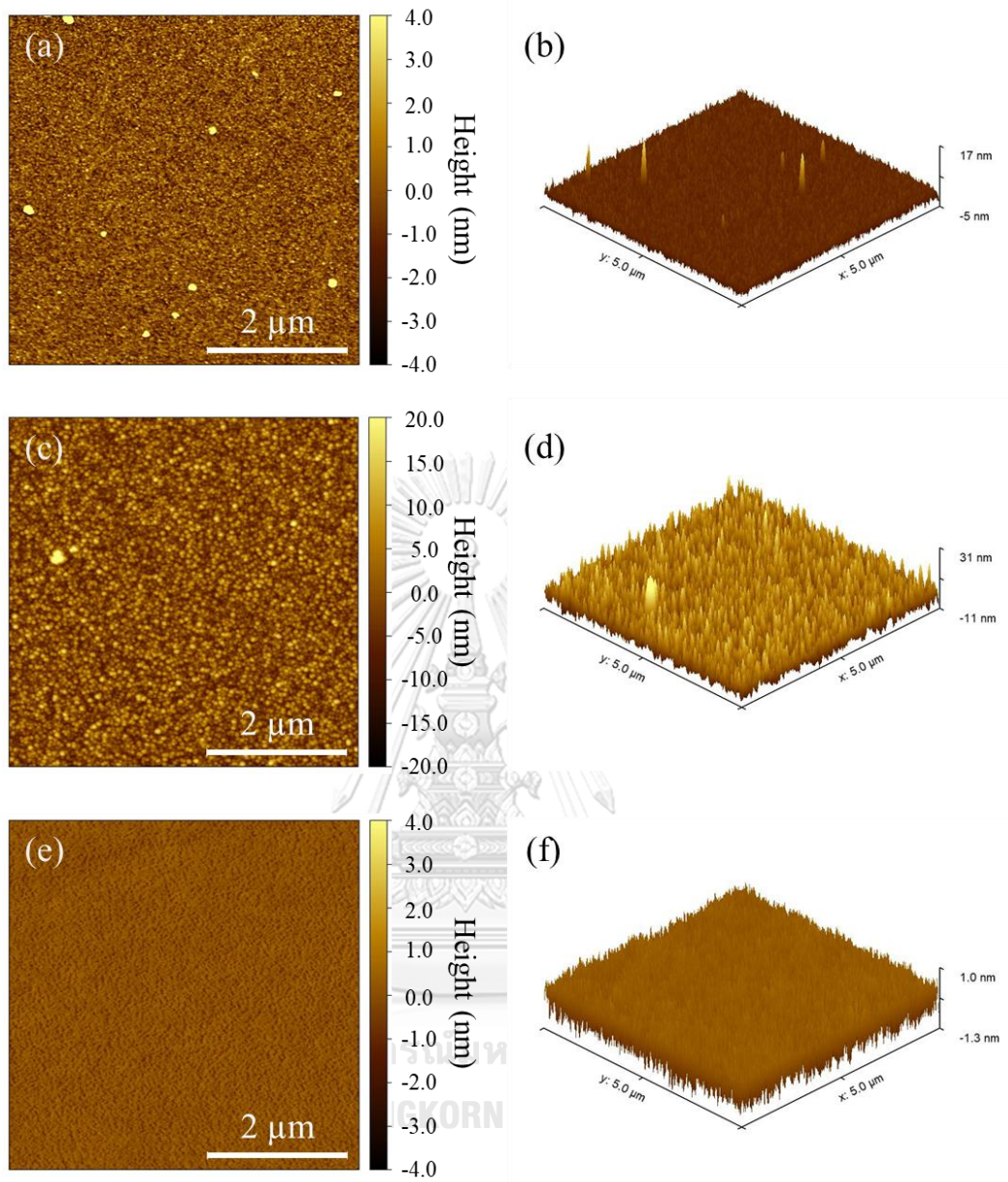


Figure 3-3 Topographic images of films by AFM (a) - (b) Cr-film, (c) - (d) Zr-film and (e) - (f) CrZr-film

Table 3-2 Surface roughness of films measured by AFM

Specimens	R_a (nm)	R_{rms} (nm)
Cr-film	0.82	1.29
Zr-film	3.57	4.45
CrZr-film	0.27	0.34

3.3.2 Phase, chemical composition and crystallinity

After understanding about film's microstructure and surface morphology, films were identified their phases and crystallinity by GIXRD. From the XRD patterns (figure 3-4), the single-component films exhibited characteristic of crystalline structure. The pattern of Cr-film matched with BCC-chromium (ICSD 01-085-1336) while the Zr-film's pattern attributed to HCP-zirconium (α -Zr, ICSD 01-089-4892) coexisting with a small amount of monoclinic-zirconium dioxide (m-ZrO₂, ICSD 01-086-1449). Formation of m-ZrO₂ was feasible during deposition process due to the significantly low standard of free energy of formation for ZrO₂ (-1,040 kJ) comparing with -702 kJ of Cr₂O₃, evaluated on basis of a molar O₂ [69]. This implied that zirconium needed lower based pressure for preventing oxidation. For the CrZr-film, it composed of zirconium-based with 40 %wt. or 54 %at. of chromium measured by EDS. Noteworthy, the XRD pattern of CrZr-film did not show any evidence of crystallinity in film; conversely, it showed a character of amorphous structure as seen by a broadly diffracted pattern near 38°. According to atomic size differences (δ) calculation [45-47], amorphous structure probably found in this composition as show in figure 3-5. Therefore, the chemical composition of this CrZr-film was desired for prepare amorphous metallic film.

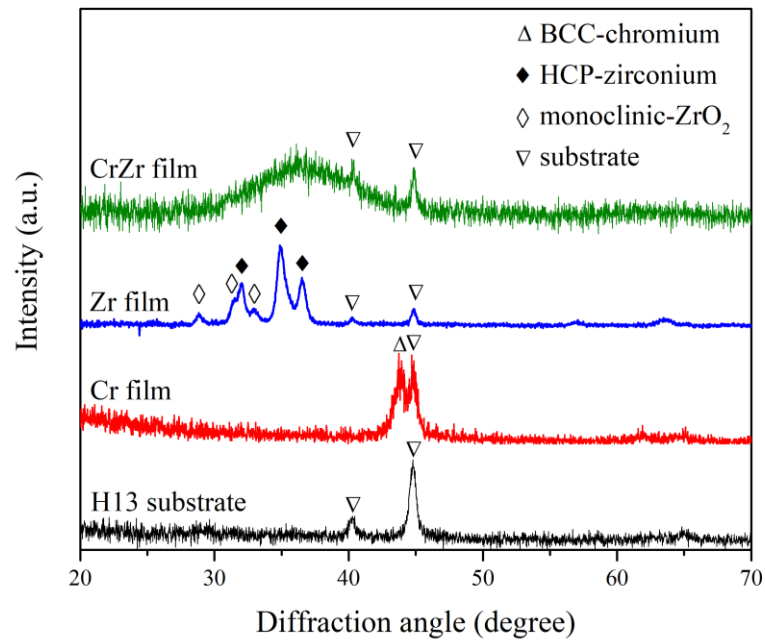


Figure 3-4 XRD patterns of metallic films and substrate

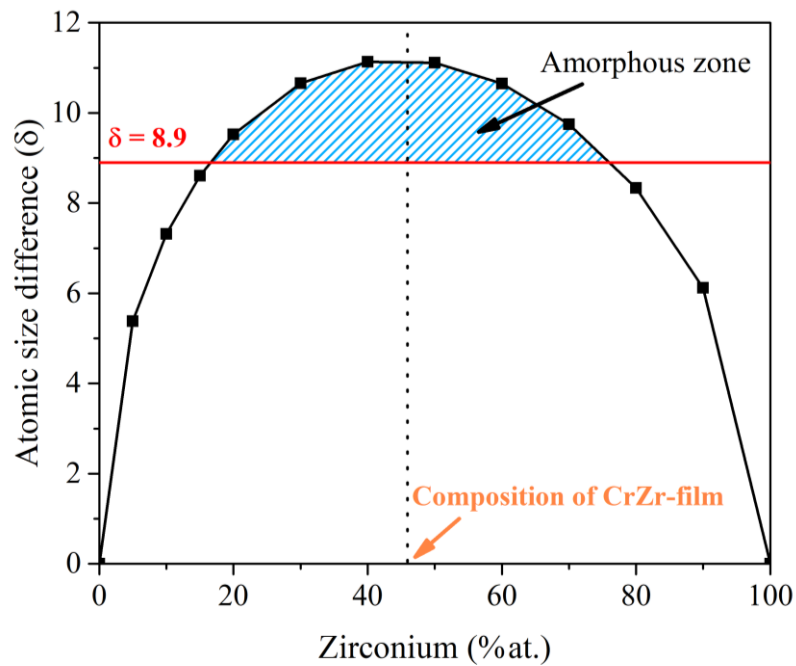


Figure 3-5 Prediction of amorphous formation zone in chromium-zirconium binary system and composition of the CrZr-film

This amorphous structure in the CrZr-film was confirmed by the HRTEM image and EDP (figure 3-6), they revealed a random atomic arrangement and a

diffuse ring. The diffuse ring was calculated for accounting into real space by equation 3-1. The polycrystalline gold (Au) particles were employed for correcting the camera constant (αL) with Au, ICSD 00-004-784. The d_{hkl} and R_i represented the d-spacing of hkl plane and reciprocal distance. This diffuse ring corresponded to 2.1-2.7 Å according to diffraction angle approximately 34.1-42.8°. This range accorded to the position of broaden peak in precious XRD result. Therefore, it was reasonable to confirm that the CrZr-film was the amorphous film. It was important to note that a moderate composition was required for an amorphous formation. From phase diagram of chromium-zirconium in figure 3-7 [70], the composition of CrZr-film located in between α -Cr₂Zr and α -Zr. Both showed the low solid solubility limit as resulting to nuclei needed the suitable composition in the narrow range. Incorporating with the low energetic adatoms due to low sputtering power, adatoms were retarded to diffuse and form a stable phase, in a way similar to frozen atoms like amorphization [71-73].

$$d_{hkl} = \frac{\alpha L}{R} \quad (\text{equation 3-1})$$

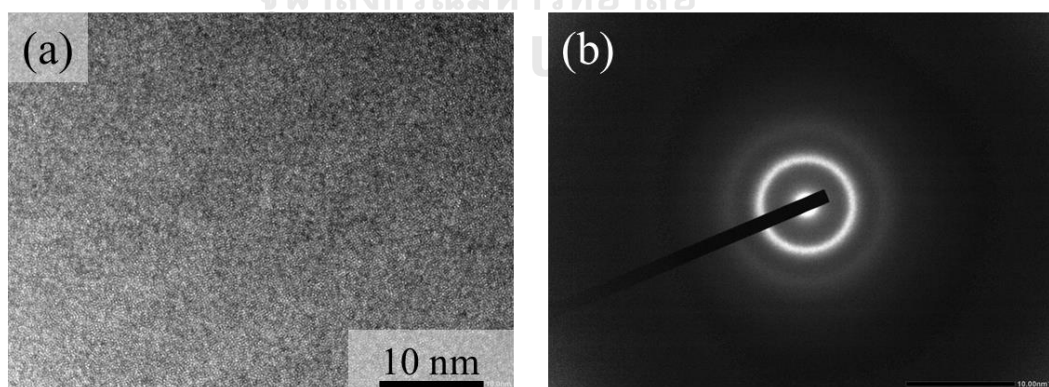


Figure 3-6 HRTEM image (a) and EDP (b) of the CrZr-film

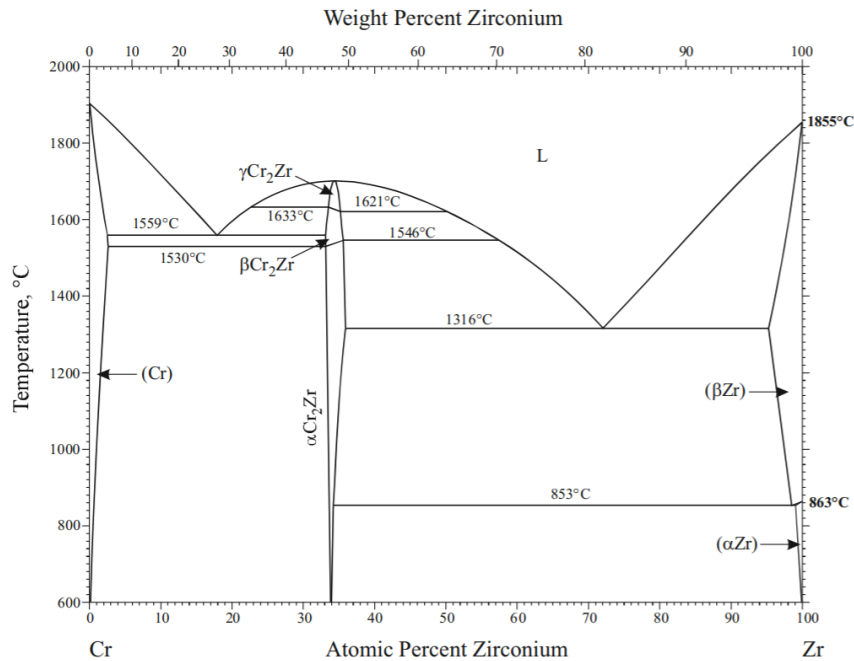


Figure 3-7 Binary phase diagram of chromium and zirconium

3.3.3 Corrosion behavior

In this research, corrosion investigation started with open circuit monitoring, EIS measurement and equivalent circuit (ECs) modelling, and potentiodynamic polarization in the last. All investigations were performed in 100 cm³ of 3.5 %wt. NaCl solution in ambient air. Open circuit monitoring was employed for investigate about corrosion stability as a function of immersion time, EIS and ECs modelling for understanding about corrosion reaction at equilibrium corrosion potential, and potentiodynamic polarization for stability and durability under bias-voltage situations.

3.3.3.1 Open circuit monitoring

Corrosion of films on H13 substrate and bare H13 substrate were initially investigated by OCP monitoring as shown in figure 3-8. The OCP of all films slightly decreased due to the partial dissolution of pre-immersion oxides/hydroxides on

surface, before reaching their equilibrium states [74]. The equilibrium potential (average OCP in last 5 seconds) of H13, Cr-film, Zr-film and CrZr-film were -639, -430, -463 and -356 mV, respectively. All films showed the higher equilibrium potential than H13 substrate, and the CrZr-film had the highest value. This implied that all films were nobler than H13 steel, and the CrZr film had the highest corrosion stability after immersion for 1200 seconds. However, the OCP measurement did not reflect the corrosion rate or corrosion behavior of those films. For this purposes, further investigation by EIS measurement and potentiodynamic polarization were discussed in the next section.

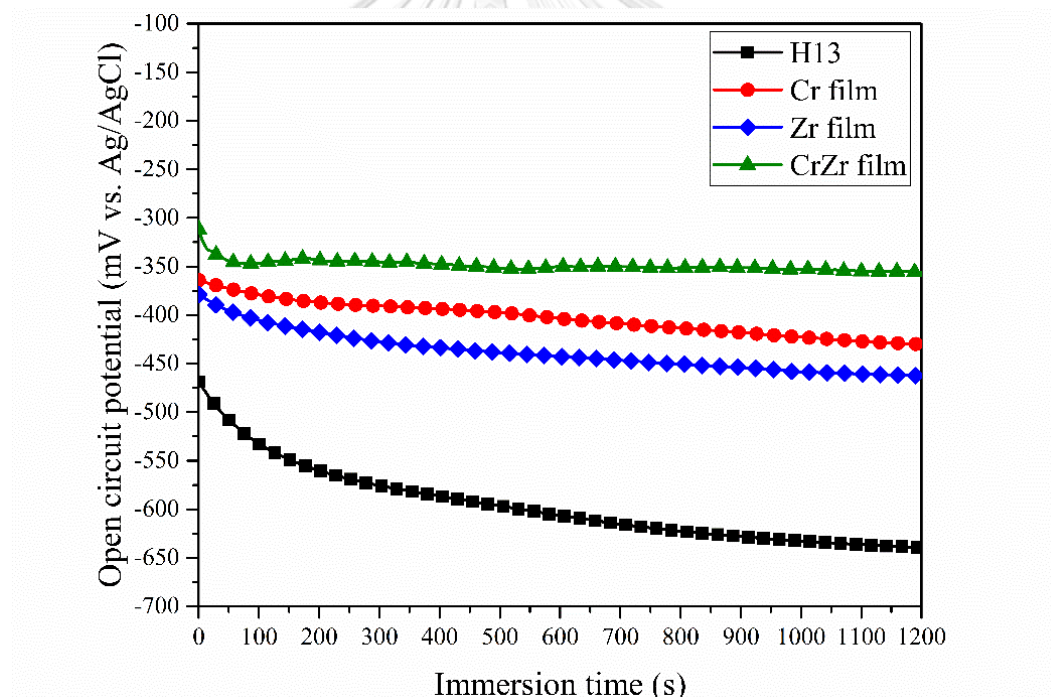


Figure 3-8 OCP monitoring with a function of immersion time

3.3.3.2 Impedance measurement

After OCP monitoring, impedance response of specimens were performed by EIS at their OCP. The Zr-film and CrZr-film exhibited higher and wider phase shift than the Cr-film and H13 substrate as seen in figure 3-9. Maximum phase shift of the

Zr-film and CrZr-film reached to 80° while the Cr-film and H13 were approximately 60° . The high and wide phase shift peak of Zr-film and CrZr-film exhibited to the capacitance property of the films, allowing retarded corrosion [36]. This agreed with the Bode modulus plot in figure 3-10. The Zr-film and CrZr-film had higher impedances that were two orders magnitude greater than those of Cr-film and bare H13 specimens at 0.01 Hz.

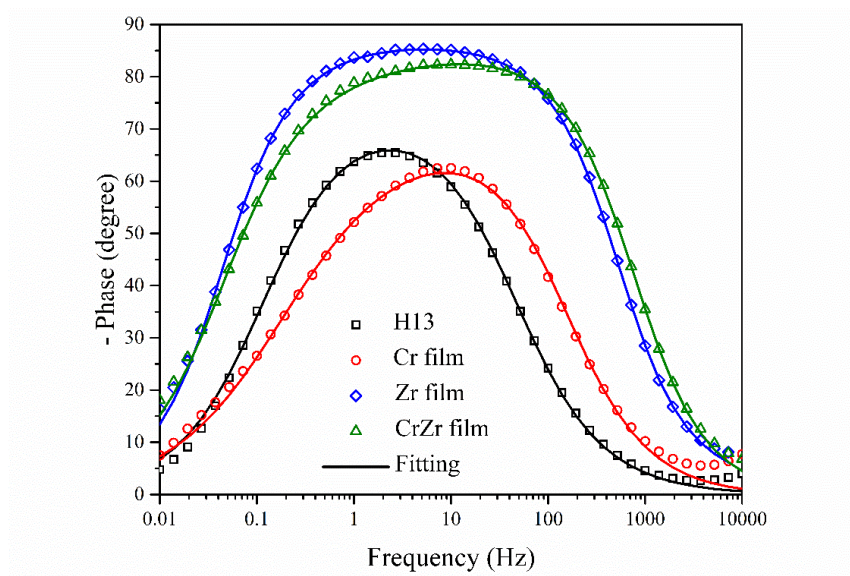


Figure 3-9 Bode phase of metallic films

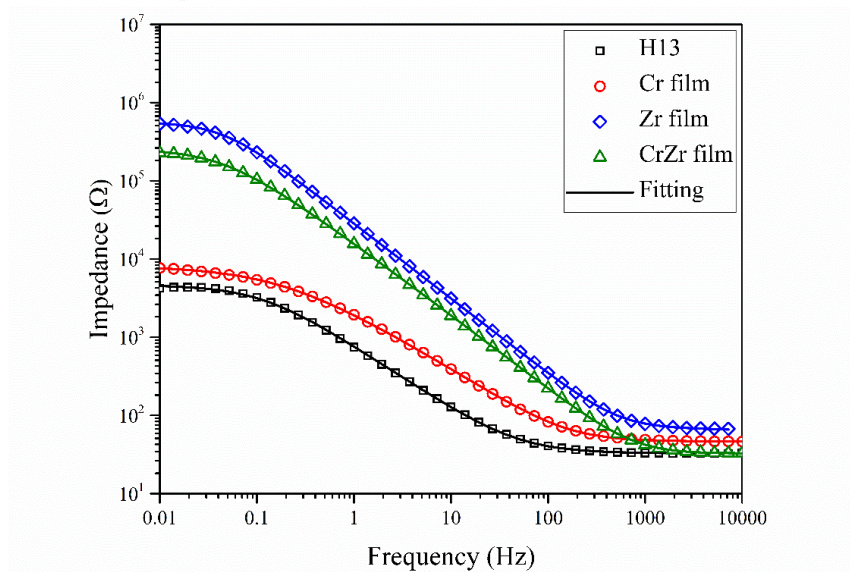


Figure 3-10 Bode modulus of metallic films

In term of Nyquist plot (figure 3-11), it revealed the depressed semicircles without tail for all specimens. The characteristic of depressed semicircle was resulted from surface heterogeneity [75]. The Zr-film and CrZr-film showed significantly larger semicircle than others, and the Zr-film was the largest semicircle. The large semicircle attributed to the high degree of protectiveness in film.

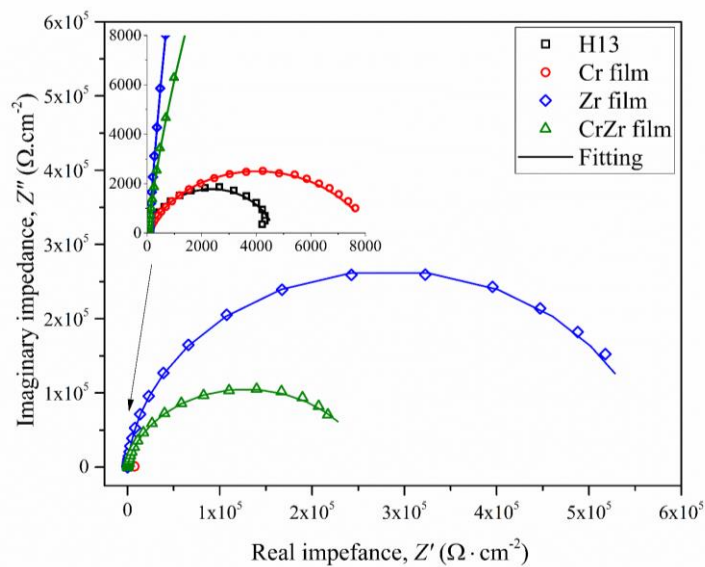


Figure 3-11 Nyquist plot of metallic films

In order to understand corrosion behavior, their impedance responds were interpreted to equivalent circuit elements (ECs) model. After fitting with several ECs models, the best ECs models, which provided the best chi-square (χ^2) and correspond to their physical model, are shown in figure 3-12. In this circuit, constant phase element (Q) was employed instead of capacitance (C) due to surface heterogeneity and for achieving better chi-square [37-39]. The impedance of Q (Z_Q) is defined as equation 3-2, where j is an imaginary number ($j^2 = -1$). The Y_0 , ω and n are an admittance (Mho), angular frequency (rad/s) and constant phase angle (rad) of Q. The Q preforms as ideal resistor and capacitor when n is 0 and 1, respectively.

$$Z_Q = \frac{1}{Y_0(j\omega)^n} \quad (\text{equation 3-2})$$

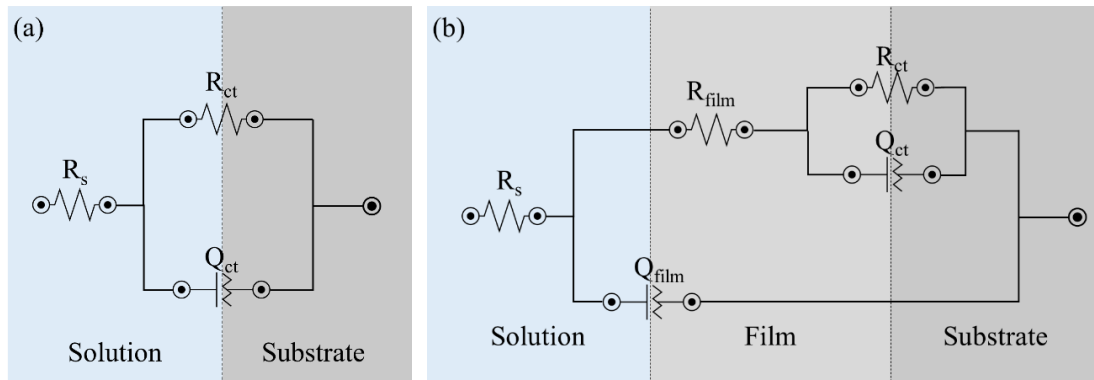


Figure 3-12 Equivalent circuit models (a) bare H13 substrate and (b) films on H13 substrate

The fitting equivalent elements are listed in table 3-3. The H13 substrate was well fitted with one time-constant ECs model of $[R_s(R_{ct}Q_{ct})]$ as shown in figure 3-12(a) while the film specimens corresponded to two time-constant model, $[R_s([R_{film}(R_{ct}Q_{ct})]Q_{film})]$ in figure 3-12(b). The two time-constant circuit was associated with corrosion at two interfaces: the solution/film interface and film/substrate interface [34-36]. Herein, the R_s represented to solution resistance which were no significant difference ($\pm 30 \Omega \cdot \text{cm}^2$) for all testing [76].

Table 3-3 Summarized of equivalent circuit model

Samples	OCP	R_s	R_{film}	Q_{film}	R_{ct}	Q_{ct}	
	(mV)	($\Omega \cdot \text{cm}^2$)	($\Omega \cdot \text{cm}^2$)	Y_0 (Mho)		n	Y_0 (Mho)
H13	-639	32	-	-	4.66	2.75×10^{-4}	0.83
Cr film	-430	45	4393	9.16×10^{-5}	0.81	2.97×10^{-4}	0.62
Zr film	-463	66	4244	4.91×10^{-6}	0.98	1.20×10^{-6}	0.80
CrZr film	-356	32	5328	9.38×10^{-6}	0.95	3.32×10^{-6}	0.72

Corrosion at solution/film interface could be explained by film capacitance (Q_{film}) and film resistance (R_{film}). The Q_{film} attributed to reactions occurring at the solution/film interface while the R_{film} attributed to film restriction of solution penetration. The Q_{film} elements of Zr-film and CrZr-film exhibited high n values of

0.98 and 0.95; respectively, which could be considered as an ideal capacitor as their n values were higher than 0.93 [77]. The ideal capacitor behavior with low Y_0 indicated that corrosion reactions at the surface of Zr-film and CrZr-film were retarded. This was due to the formation of a stable zirconium oxide film on the surface, which will be described in the next section.

In term of R_{film} , it was associated to restriction of solution penetration through film. It was found that the value of R_{film} strongly depended on film crystallinity and microstructure. The CrZr-film with featureless amorphous structure exhibited the highest value of R_{film} since there was no susceptible points for corrosion attack [78]. Conversely, crystalline Cr-film and Zr-film having a columnar structure and intercolumnar area were susceptible to penetration of corrosion media resulting in low values of R_{film} .

After solution successfully penetrated through the film and reached to H13 interface, corrosion at film/substrate interface could be explained by a parallel of charge transfer-capacitance (Q_{ct}) and -resistance (R_{ct}). None of these films had the n of Q_{ct} exceeded 0.93 which indicated to non-ideal capacitor behavior [77]. This suggested that there was no/ineffective protective film forming at the solution/substrate interface. Furthermore, the R_{ct} increased with increased zirconium content in the film, according to their natural electrical resistivity (ρ ; $\rho_{\text{Zr}} = 421 \text{ n}\Omega\cdot\text{m}$ and $\rho_{\text{Cr}} = 145 \text{ n}\Omega\cdot\text{m}$) [79, 80]. This gave high impedance of small circuit resulting in superior corrosion resistance even after the solution partially reached to substrate.

Considering the overall corrosion processes at both interfaces, controlling film structure as an amorphous solid enhanced the stability and the quality of the

solution/film interface, as could be seen by the high values of OCP, n of Q_{film} , R_{film} , and low Y_0 in the CrZr-film. The addition of zirconium in film could improve corrosion resistance especially at film/substrate interface as seen by the high impedance of a parallel of Q_{ct} and R_{ct} in the Zr-film and CrZr-film. The Zr-film and CrZr-film had high total impedance over the Cr-film at their average OCP.

3.3.3.3 Potentiodynamic polarization

To consider application of the films, the duration and stability of the films must be considered. Therefore, potentiodynamic polarization was performed for corrosion investigation in wide potential range as shown in figure 3-13. Corrosion potential (E_{corr}), corrosion current density (I_{corr}) and other important parameters were calculated from NOVA 1.11 software and are listed in table 3-4. The amorphous-featureless of CrZr-film showed the highest E_{corr} among all specimens representing to the highest degree of corrosion stability which was expected for anti-corrosion application. The E_{corr} result agreed with the previous R_{film} result, which revealed that the CrZr-film was the highest due to the absent of susceptible points [78, 81].

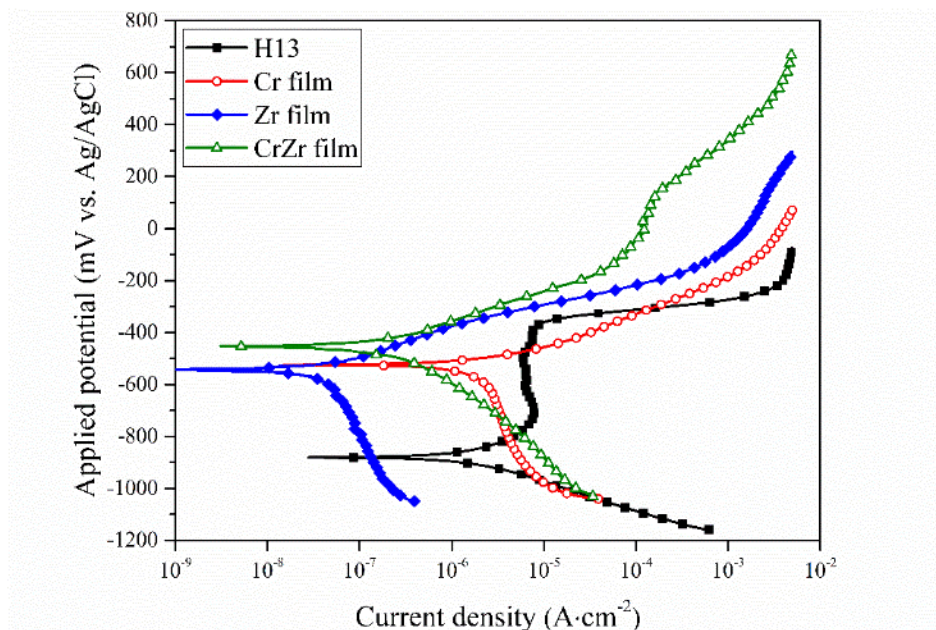


Figure 3-13 Potentiodynamic polarization of metallic film and substrate

Table 3-4 Corrosion parameters of specimens

Sample	E_{corr} (mV)	I_{corr} ($A \cdot cm^{-2}$)	β_a ($mV \cdot dec^{-1}$)	β_c ($mV \cdot dec^{-1}$)	R_p ($k\Omega$)	E_{pass} (mV)	I_{pass} ($A \cdot cm^{-2}$)	$E_{pitting}$ (mV)
H13	-880	2.28×10^{-6}	128.3	191.7	14.62	-779	7.70×10^{-6}	-355
Cr film	-521	1.25×10^{-6}	231.5	65.5	17.66	-	-	-
Zr film	-543	2.20×10^{-8}	99.7	68.1	797.64	-	-	-
CrZr film	-453	4.12×10^{-8}	48.6	39.0	227.39	-134	6.31×10^{-4}	137

Considering in term of I_{corr} , it was found that the I_{corr} tended to decrease with a zirconium fraction in film. The trend of I_{corr} was an inverse relationship to R_{ct} as well as other reports [82-84]. Because of the higher anodic current in H13 substrate, corrosion preferentially occurred at substrate instead of film surface after solution reaching to substrate. This phenomenon associated to the description of R_{ct} ; therefore, addition of zirconium affected to I_{corr} and R_{ct} as previous mention.

When increasing test potentials, the CrZr-film exhibited spontaneous passivation with passive current density (I_{pass}) approximately $10^{-4} A/cm^2$. This was suggested that it was due to the shortest active region (E_{corr} to E_{pass}) with lowest

anodic current density in the CrZr-film. This implied that the corrosion in CrZr-film took place in shortest period with the lowest metal dissolution rate. As a result, the CrZr-film had low damages before passivation (as shown in active region II). For this reason, passive film in the CrZr-film could form and cover the entire surface as shown in figure 3-14. According to other studies, passivation over damaged surface led to a low quality or high I_{pass} of passive film [85, 86]. Therefore, the CrZr-film had an ability to form the effective passive film.

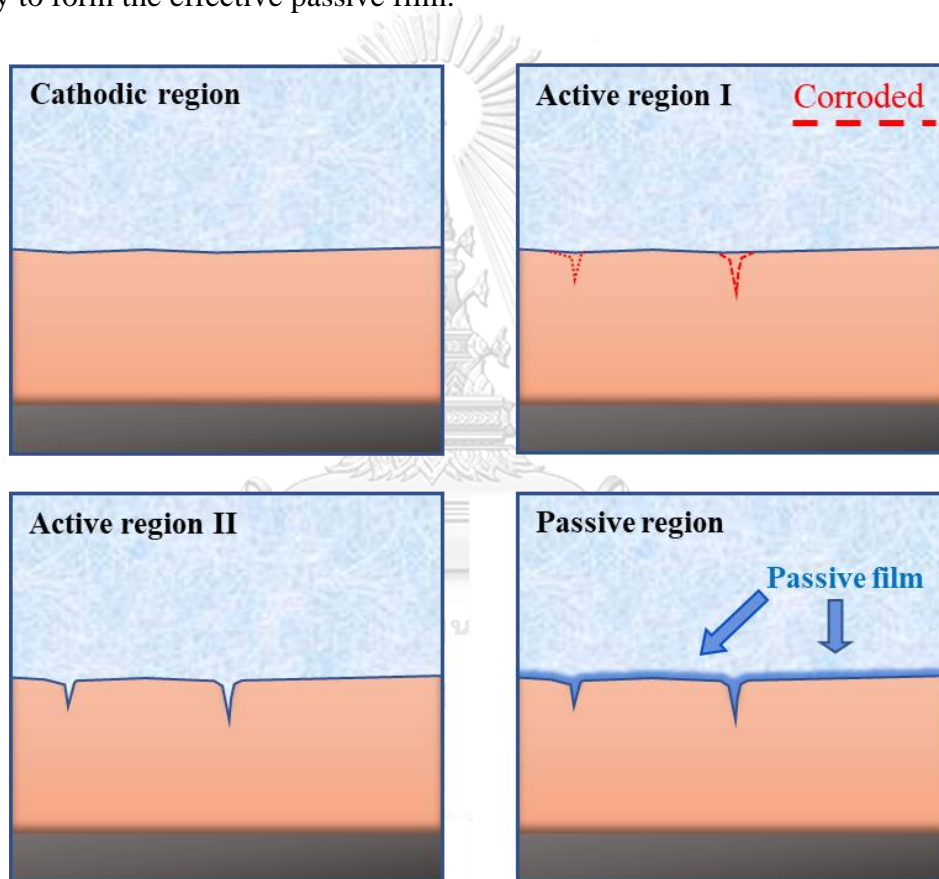


Figure 3-14 Illustration of corrosion process and passivation on the CrZr-film

Although the Cr-film and Zr-film seem to show ability to passivation, the formation of passive layer at such high current density values (over than 10^{-3} A/cm²) could not be considered as effective passivation. Because of wide active region and having columnar structure in the Cr-film and Zr-film, these films had more damages

before passivation especially at intercolumnar area. These damages among columnar could perform as direct path for solution penetration, caused some solution penetrated to substrate in a short period of time. Though the passive layer could be later formed on top of the Cr-film and Zr-film, the corrosion would mainly take place at the film/substrate interface instead of film/solution interface as shown in figure 3-15. As a result, protection by these passive layers to achieve a low I_{pass} could not be accomplished. The higher I_{pass} in Cr-film, in comparison with Zr-film, was a result of the higher degree of porosity as seen in the microstructure (figure 3-1).

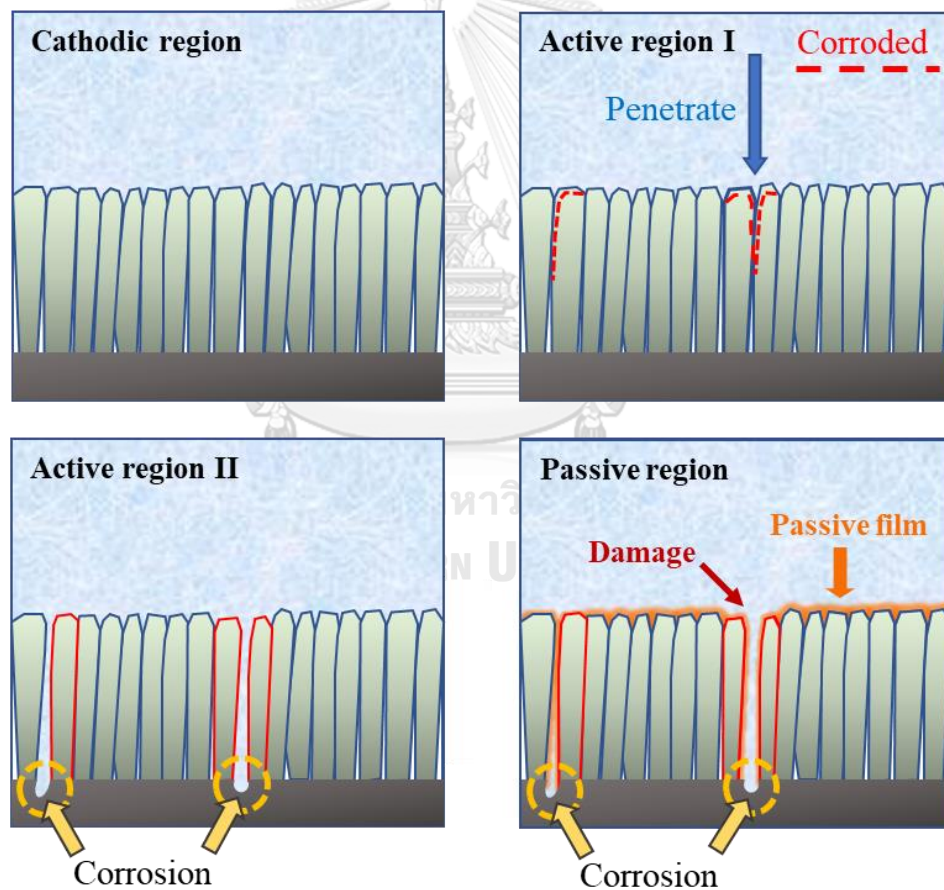


Figure 3-15 Illustration of corrosion process and passivation on columnar films

3.3.4 SEM observation of corroding films

After corrosion testing, films were again observed their morphology as shown in figure 3-16. All films suffered from pitting corrosion especially the Cr-film and Zr-film because pits preferentially formed at grain boundary and intercolumnar space [86]. Pits were initial points for solution penetration leading to film failure and corrosion under coating. The difference of corrosion failures in films caused by their microstructure. Columnar structure in the Cr-film and Zr-film were susceptible to expansion of corrosion product under coating (especially in parallel with columnar direction), leading to film delamination. In contrast, the CrZr-film still covered almost substrate surface though the filiform corrosion was found in some area as seen by thread-bulge structure in figure 3-16(c). Because of the single-dense layer without columnar structure, it was more tolerable to expansion of corrosion products including in perpendicular direction.

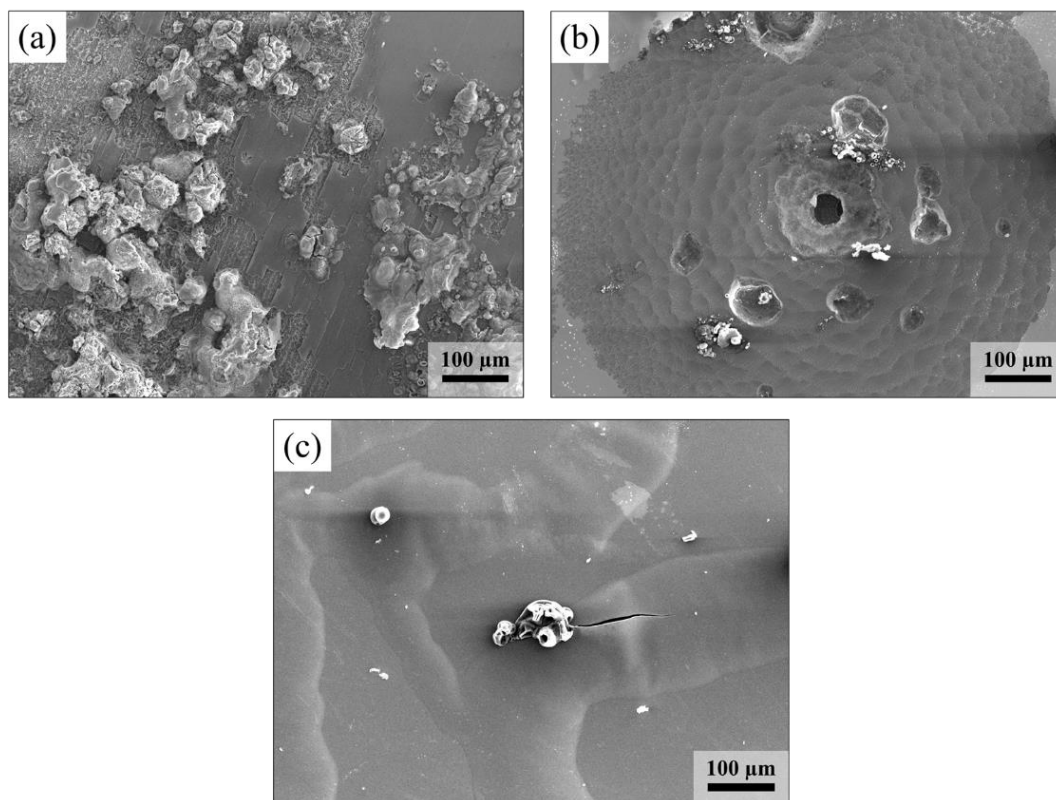


Figure 3-16 SEM after potentiodynamic polarization testing (a) - (c) Cr-film, Zr-film and CrZr-film.

3.3.5 XPS analysis of corroding film

Afterward, corroding specimens were investigated their chemical states and compounds by XPS analysis. The investigation was performed on specimen surface and beneath by etching with Ar sputtering every 2 seconds from 0 to 10 seconds. The XPS analyses were separated into 3 subtopics according to 3 kinds of films.

3.3.4.1 XPS analysis of Cr-film

XPS analysis of Cr-film consisted of the Cr 2p and O 1s spectra as shown in figure 3-17. Without sputtering, the Cr 2p spectra were deconvoluted into 2 pair of peaks. This implied that there were co-existences of two oxidation states on surface. These binding energy (b.e.) associated to Cr 2p_{1/2} and Cr 2p_{3/2} spin-orbital splitting of

Cr^{6+} (b.e. = 588.4 and 578.7 eV for Cr 2p_{1/2} and Cr 2p_{3/2}) and Cr^{3+} (b.e. = 586.4 and 576.7 eV for Cr 2p_{1/2} and Cr 2p_{3/2}). The doublet peaks of Cr^{6+} and Cr^{3+} denoted the presence of CrO_3 , $\text{Cr}(\text{OH})_3$ and Cr_2O_3 [87-91]. According to the O 1s result, it revealed the O^{2-} peak of adsorbed water at 533.2 eV, $\text{Cr}(\text{OH})_3$ at 532.0 eV and at 530.5 eV for chromium oxide compounds (CrO_3 , Cr_2O_3) on surface [87-89]. The presence of adsorbed water correlated to moisture from air. Binding energy of those compounds are listed in table 3-5.

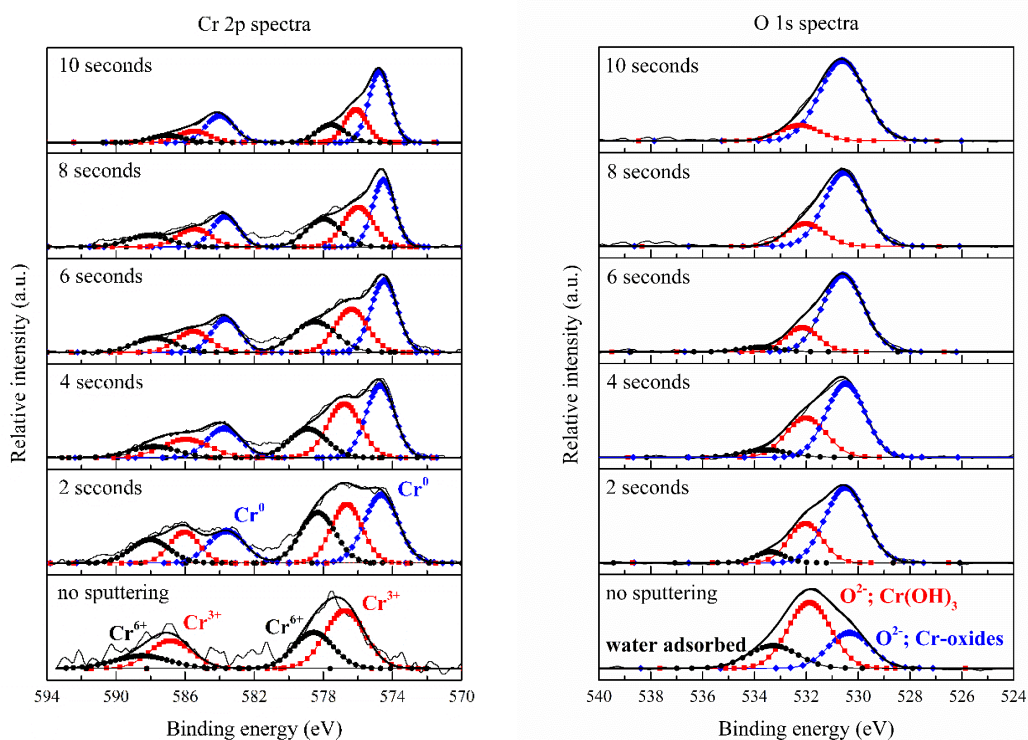


Figure 3-17 XPS evolution of Cr 2p and O 1s spectra in Cr-film

Table 3-5 Deconvolution of XPS spectra in the Cr-film

Compounds	Deconvoluted peak spectra (eV)		
	Cr 2p _{1/2}	Cr 2p _{3/2}	O 1s
CrO ₃	588.1±0.3	578.3±0.4	530.5±0.2
Cr ₂ O ₃	585.9±0.5	576.4±0.3	530.5±0.1
Cr(OH) ₃	585.9±0.5	576.4±0.3	532.0±0.3
Cr-metallic	583.7±0.2	574.6±0.1	-
Adsorbed water	-	-	533.4±0.2

After sputtering for 2 seconds, the doublet peaks of metallic chromium (Cr⁰) were detected and became the predominant peaks at 583.6 and 574.5 eV [89]. From the O 1s spectra, the intensity of hydroxide compound noticeably decreased, as a result, peak of oxide compound became the predominance instead. This implied that almost of Cr(OH)₃ formed on surface and its amount decreased with sputtering time as shown in figure 3-18.

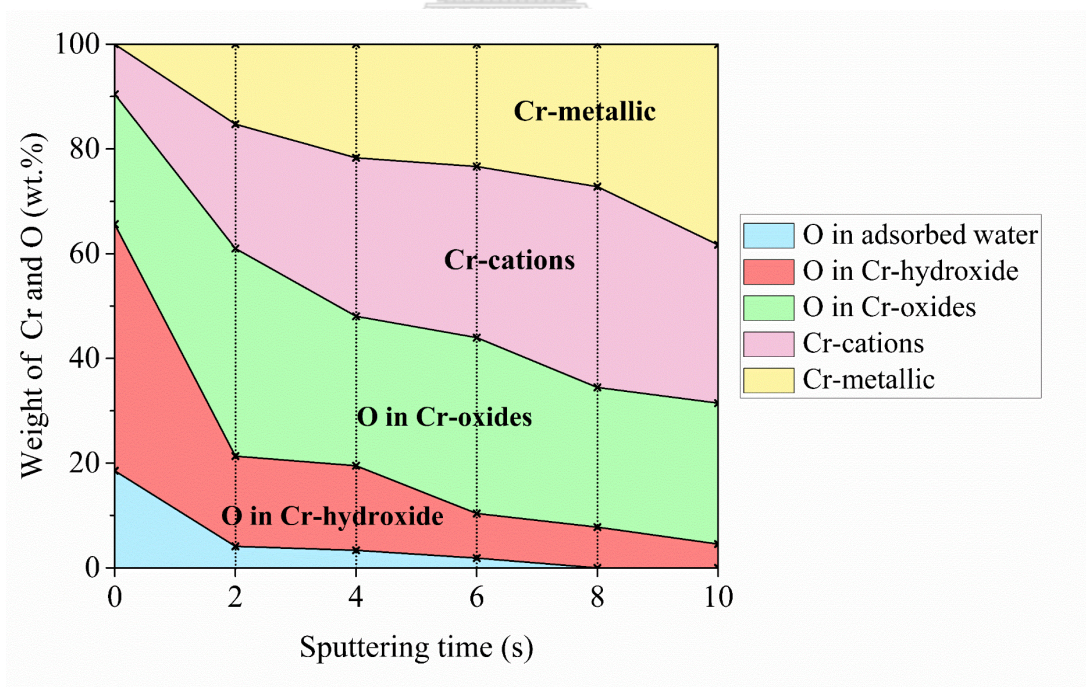


Figure 3-18 Compounds profiles of Cr-film with sputtering time

3.3.4.2 XPS analysis of Zr-film

The XPS spectra of Zr-film after corrosion tests, are shown in figure 3-19. The two splitting peaks at 185.3 and 183.0 eV, corresponding to Zr 3d_{3/2} and Zr 3d_{5/2} of Zr⁴⁺, were found on the surface [92-96]. The high intensities of these two peaks implied that Zr⁴⁺ is the predominant oxidation state at the surface. It could be in the form of zirconium oxide (ZrO₂) or zirconium hydroxide, Zr(OH)₄, or a mixture of the two. This ambiguity was distinguished by the O1s spectra. It was well deconvoluted into 3 peaks at 533.8, 532.6 and 531.1 eV, which corresponds to O²⁻ adsorbed water, Zr(OH)₄, and ZrO₂, respectively [94-97]. This result confirmed the coexistence of both ZrO₂ and Zr(OH)₄ on the top surface. The fraction of compounds is shown in figure 3-20.

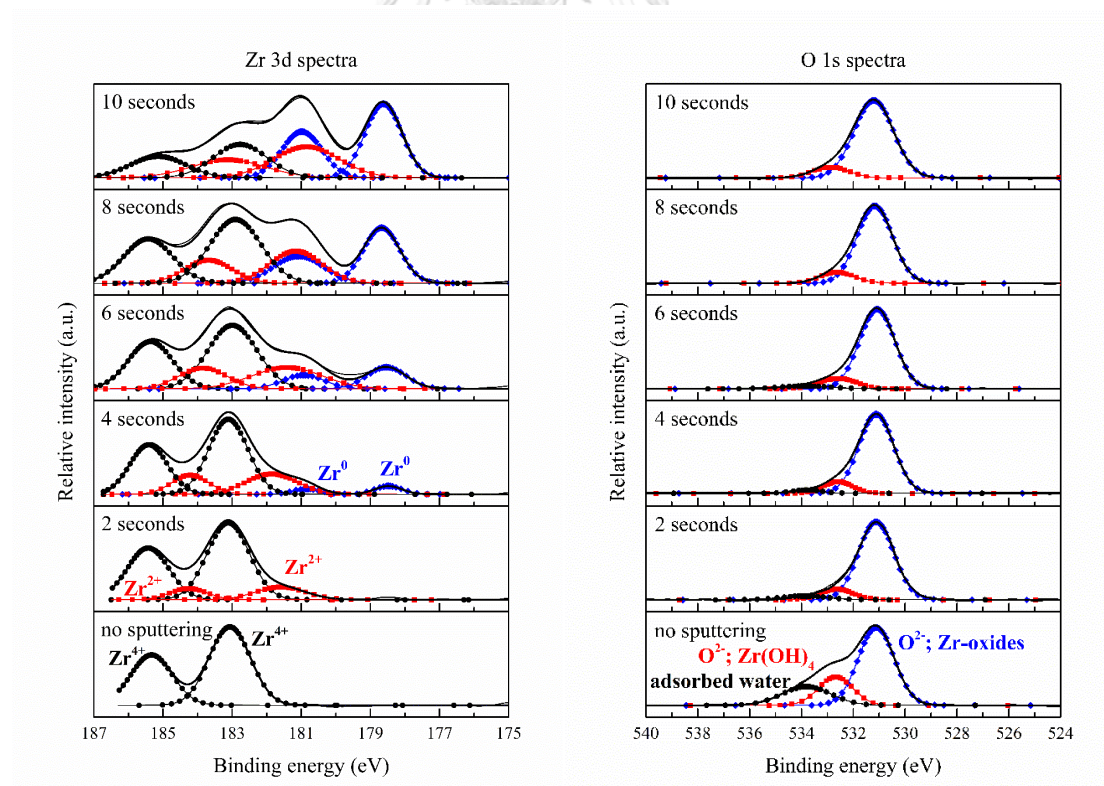


Figure 3-19 XPS evolution of Zr 3d and O 1s spectra in Zr-film

Table 3-6 Deconvolution of XPS spectra in the Zr-film

Compounds	Deconvoluted peak spectra		
	Zr 3d _{3/2} (eV)	Zr 3d _{5/2} (eV)	O 1s (eV)
ZrO ₂	185.3±0.1	183.0±0.1	531.1±0.1
ZrO _x , x<2	183.6±0.6	181.1±0.4	531.1±0.1
Zr(OH) ₄	185.3±0.1	183.0±0.1	532.7±0.2
Zr-metallic	180.9±0.2	178.6±0.1	-
Adsorbed water	-	-	533.8±0.2

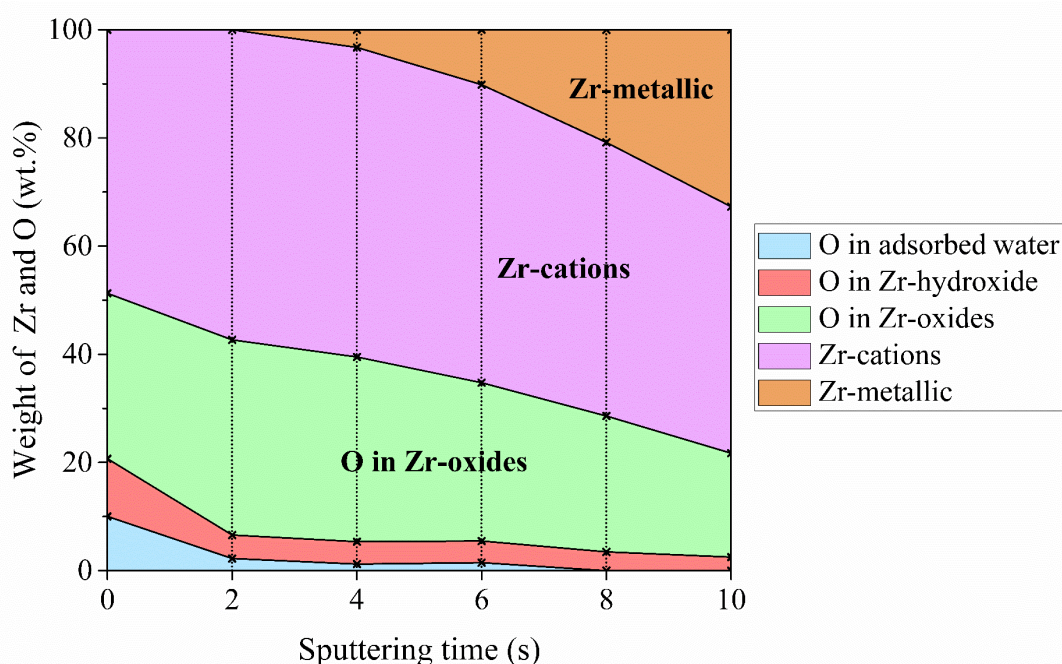


Figure 3-20 Compounds profile of Zr film with sputtering time

After sputtering for 2 seconds, Zr⁴⁺ was found to be a dominant oxidation state together with small amount of lower oxidation state zirconium (Zr²⁺) as seen by low intensity peaks at 184.2 and 181.5 eV. The Zr²⁺ peaks were denoted as zirconium oxide (ZrO). After more sputtering, a slight shift of Zr²⁺ peaks to the lower binding energy was observed and reached to 183.1 and 180.4 eV when sputtering for 10 seconds. This was suggested to be the formation of non-stoichiometric zirconium oxide (ZrO_x, x<1) beneath the ZrO layer [98-102]. From this it could be concluded

that formation of zirconium oxide was in the form of ZrO_{2-x} , in which the value of x increased from 0 at the surface to a value greater than 1 after 10 seconds of sputtering due to the slow diffusion of oxygen through the zirconium oxide layer [101]. The metallic zirconium peaks (Zr^0) were detected at 180.9 and 178.6 eV [102], after 4 seconds of sputtering.

Furthermore, the intensity of adsorbed water peak significantly decreased after 2 seconds of sputtering. This indicated that water could penetrate through film in a limited distance comparing with the deeper penetration in Cr-film. The Zr-film had SZM T structure which was considerably denser than the SZM I structure of Cr-film, and was more effective in preventing water penetration into the film.

3.3.4.3 XPS analysis of CrZr-film

The XPS spectra of CrZr-film consisted of Cr 2p, Zr 3d and O 1s spectra as shown in figure 3-21. The Cr 2p spectra of CrZr-film had three doublet peaks, attributed to 3 oxidation states of chromium; Cr^{6+} in CrO_3 , Cr^{3+} in $Cr_2O_3/Cr(OH)_3$ and metallic Cr^0 , which were the same as the detected peaks in Cr-film. When sputtering for 2 seconds, the intensities of Cr^{6+} and Cr^{3+} in oxide and hydroxide peaks decreased, as a result, the Cr^0 doublet peaks were the predominance. Likewise, most of the zirconium was fully oxidized to Zr^{4+} at and near surface, and was significantly decreased by sputtering for 4 seconds as shown in figure 3-22. This indicated that oxide/hydroxide compounds were preferentially formed only as a thin layer on top of the surface, and would be removed by sputtering. In addition, the binding energy of deconvoluted peaks are listed in table 3-7.

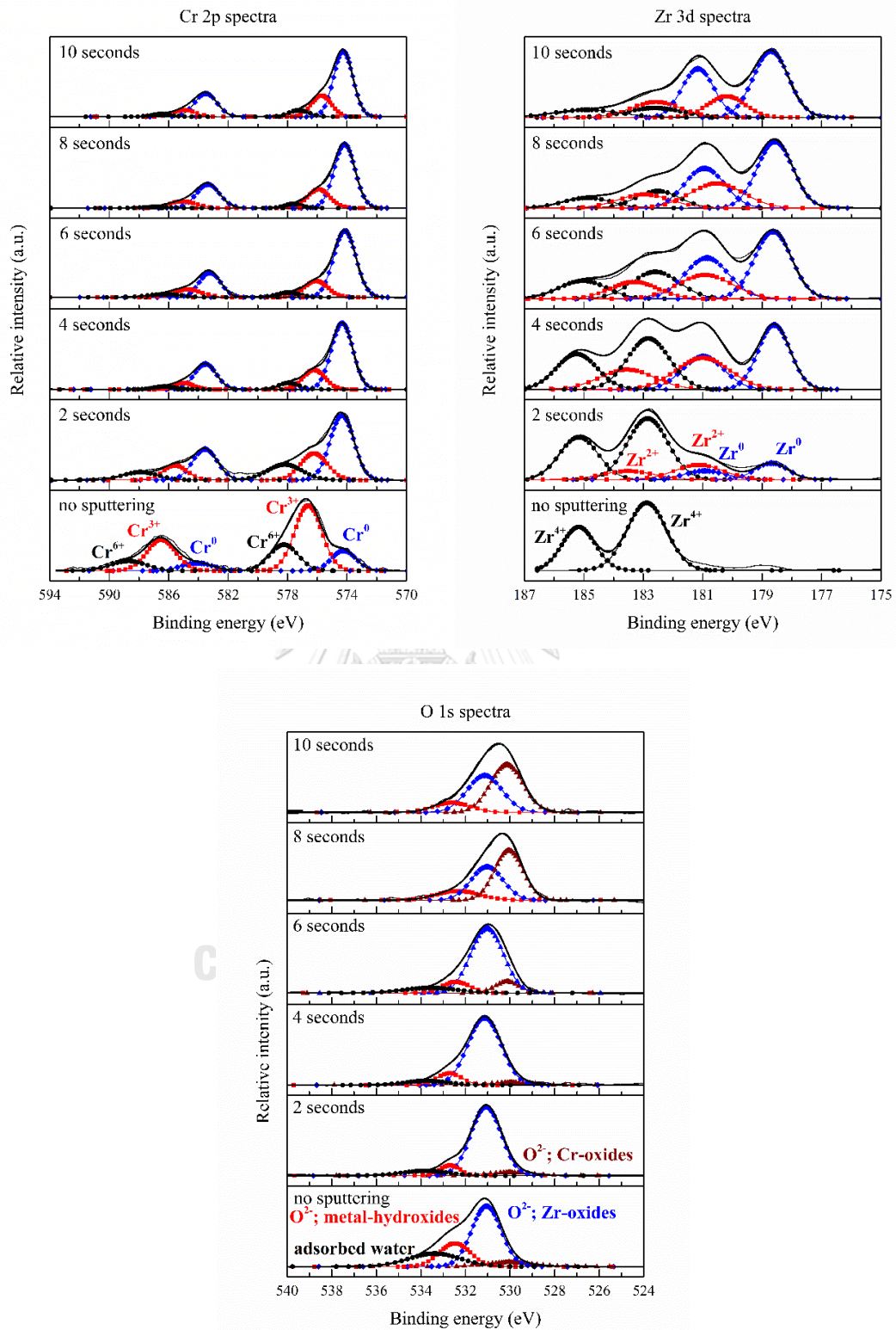


Figure 3-21 XPS evolution of Cr 2p, Zr 3d and O 1s of CrZr-film

Table 3-7 Deconvolution of XPS spectra in the CrZr-film

Compounds	Deconvoluted peak spectra (eV)				
	Cr 2p _{1/2}	Cr 2p _{3/2}	Zr 3d _{3/2}	Zr 3d _{5/2}	O 1s
CrO ₃	588.1±0.3	578.3±0.4	-	-	530.1±0.2
Cr ₂ O ₃	585.9±0.5	576.4±0.3	-	-	530.1±0.2
Cr-metallic	583.7±0.2	574.6±0.1	-	-	-
ZrO ₂	-	-	185.2±0.1	182.8±0.2	531.1±0.1
ZrO _x , x<2	-	-	183.2±0.3	180.8±0.4	531.1±0.1
Zr-metallic	-	-	178.6±0.1	181.0±0.1	-
Metal-hydroxides	-	-	-	-	532.5±0.2
Adsorbed water	-	-	-	-	533.4±0.2

Because this film composed of two metals and had an ability to passivation, the ambiguity about oxide compounds in passive film must be distinguished by the O 1s spectra. It was well deconvoluted into 4 peaks attributing to adsorbed water, metal-hydroxides, Zr-oxides, and Cr-oxides. The adsorbed water peak occurred only at the top surface as can be seen by peak at 533.4 eV, and significantly reduced after only 2 seconds sputtering. Though there were existence of Cr-oxides and Zr-oxides along the testing depth, the fraction of zirconium oxide was higher than chromium oxide at/near surface. Therefore, it could confirm that zirconium oxides were the main oxide compound for the passivation on the top surface of CrZr-film as seen by the high fraction at/near surface. It could believe that ZrO₂ was the main compound in passive layer of the CrZr-film as seen in the Zr 3d spectra result. Amount Zr-oxides implying to passive layer tended to decrease with sputtering time, as a result to clearly observe the peak of chromium oxide in the O1s spectra.

Furthermore, the CrZr-film also contained a lower amount of hydroxide than other films. Unfortunately, they could not be clearly distinguish about fraction of

$\text{Cr}(\text{OH})_3$ and $\text{Zr}(\text{OH})_4$ due to the close binding energy of them. Hence, they were considered as only a hydroxide compound. It has been reported that hydroxide compound had poorer corrosion resistance than oxide compound [103, 104]. This directly affected to film's corrosion property; therefore, the oxides/hydroxide ratio in each film would be discussed in the next section.

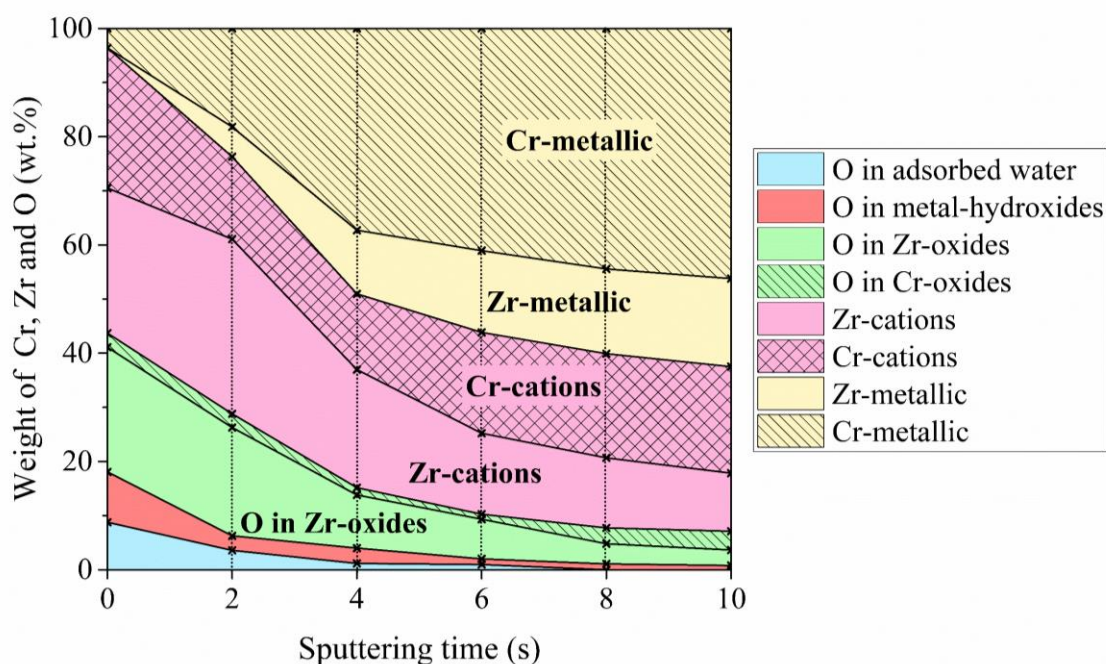


Figure 3-22 Compounds profile of CrZr-film with sputtering time

3.3.6 Effect of the oxide/hydroxide ratio on corrosion property

As previous results, the compounds in passive films directly affected to corrosion property. From the XPS result, the films were composed of oxide and hydroxide compounds in different ratios as shown in figure 3-23. The CrZr-film had higher values of oxide/hydroxide ratio than other films especially at 2 seconds of sputtering. It was known that an oxide film provides a better passivation layer than hydroxide film [103, 104]. Therefore, the higher oxide/hydroxide ratio on CrZr-film yielded better corrosion resistance than other films.

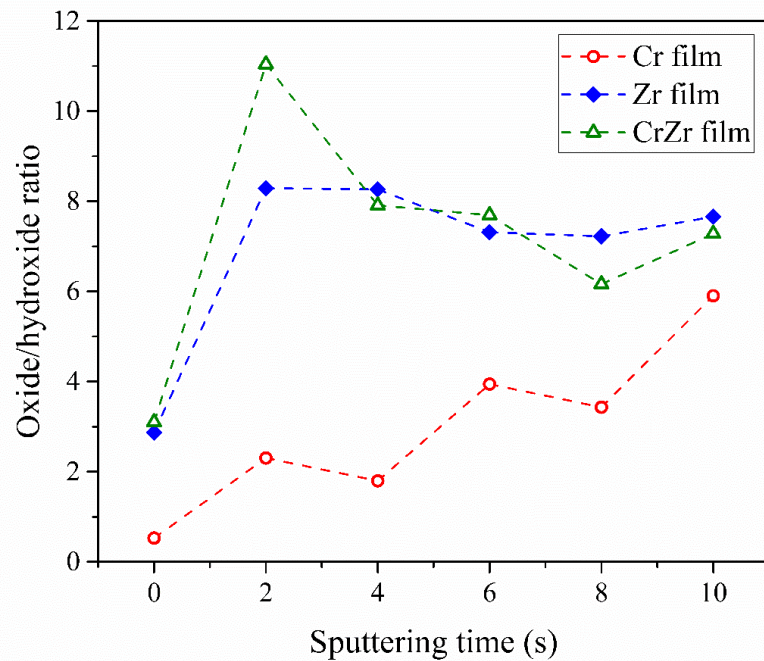
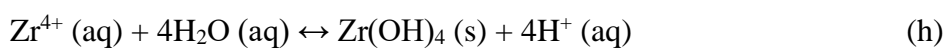
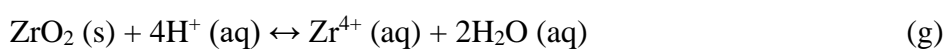
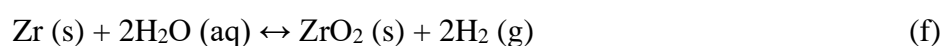
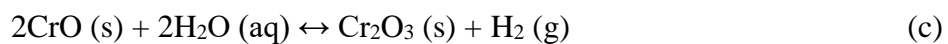
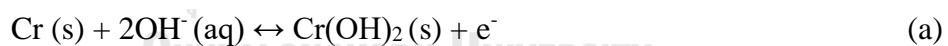


Figure 3-23 Oxide/hydroxide ration with sputtering time

In terms of the dissolution of films in 3.5 %wt. NaCl solution during the tests, the plausible reactions related to oxide and hydroxide formation of Cr-film, Zr-film and CrZr-film are listed below [77, 103-105].

Equations:



Chromium metal reacted with hydroxide ion (OH^-), water (H_2O) and oxygen (O_2) in the solution to form hydroxide and oxide compounds as seen from reactions (a) to (e). Under pH values between 6 to 7 in the tests and data from the Ellingham diagram, it was found that both chromous hydroxide ($\text{Cr}(\text{OH})_2$) and $\text{Cr}(\text{OH})_3$ could be formed by reaction (a) and (e), respectively [106]. Although, the $\text{Cr}(\text{OH})_2$ did not exist on the surface as confirmed by XPS analysis, it was able to transform into Cr_2O_3 as shown by reaction (b), (c) and (d). In Zr-film, reactions to form hydroxide and oxide compounds are shown in reaction (f), (g) and (h). Reaction (g) described the possibility of zirconium oxide (ZrO_2) dissolution in acid solution ($\text{pH} < 7$). Dissolution of ZrO_2 in reaction (g) increased Zr^{4+} content in the solution which promoted the formation of $\text{Zr}(\text{OH})_4$ by reaction (h). In the case of CrZr-film, all reactions listed above occurred simultaneously. Due to the intimate random mixing of chromium and zirconium in the amorphous film, as seen in the FESEM and TEM images, all reactions occurred uniformly on the entire film surface. On the CrZr film-surface, the formation of $\text{Cr}(\text{OH})_2$ released an electron as can be seen in reaction (a). This one electron could react with a hydrogen ion (H^+) to form H_2 gas, according to the reaction, $2\text{H}^+(\text{aq}) + 2\text{e}^- \leftrightarrow \text{H}_2(\text{g})$. Depletion of H^+ due to this reaction enhanced ZrO_2 stability in the passive layer by limiting the dissolution of the ZrO_2 compound according to reaction (g), resulting in a better passivity of the CrZr-film comparing to the Cr-film and Zr-film. Moreover, lowering the hydrogen content at the specimen surface improved its corrosion resistance. It has been reported that reduction of hydrogen effectively decreases the corrosion rate of metal including zirconium as reported by several research groups [107-109]. Oxide formed in a low hydrogen content solution was thin and had the form of tetragonal zirconium oxide (t- ZrO_2)

which was known for its superior corrosion resistance. When the content of hydrogen in the solution increased, thick ZrO_2 with monoclinic structure occurred resulting in low corrosion resistance. This explanation is in accordance with the results found by XPS analysis showing that the CrZr-film has thinner ZrO_2 layer than Zr-film.

3.4 Summary

Magnetron sputtering of chromium and zirconium targets could fabricate a pure chromium (Cr-film), pure zirconium (Zr-film), and mixture of them (CrZr-film). They covered the entire surface with smooth surface (R_a in 2-5 nm) and uniform thickness in the range of 380-450 nm. Noteworthy, the mixture film showed amorphous-featureless structure while the pure film exhibited crystalline-columnar structure. Amorphization in the CrZr-film was promoted by low energetic adatoms due to low discharge sputtering power, and suitable composition (moderate range composition).

From corrosion test, all films significantly improved corrosion resistance of H13 substrate especially in the Zr-film and CrZr-film. The CrZr-film exhibited the highest protectiveness among the films as seen by the highest E_{corr} , low I_{corr} and passivation ability. It could improve E_{corr} from -881 mV of H13 to -453 mV, and greatly reduced I_{corr} from 10^{-6} to 10^{-8} A/cm². The good at corrosion property of this film was supported by featureless-amorphous structure. The featureless structure retarded solution penetration through film and amorphous reduced susceptible points for corrosion attack, leading to the highest film resistance (R_{film}) in the equivalent circuit. In contrast, the penetration of solution through intercolumnar paths in pure films was anticipated resulting in low R_{film} . Although the pure films had an ability to

passivation at higher potentials, corrosion preferentially occurred at substrate interface instead of film surface after solution reaching to substrate interface. Therefore, the crystalline-columnar structure of pure films had lower protectiveness than the featureless-amorphous structure in the CrZr-film.

Equivalent circuits together with surface compound analysis by XPS clarified the role of zirconium on the corrosion behaviors of the films. Zirconium in the film played an important role in the formation of a protective layer in the form of zirconium oxide film. The formation of zirconium oxide as a protective layer was more effective than the formation of chromium oxide due to its natural property. The formation of zirconium oxide delayed the corrosion reaction on the film/solution interface as seen from low values of Y_0 and high values of n (close to unity) in film capacitance (Q_{film}) of the Zr-film and CrZr-film. In contrast, the Cr-film exhibited a high Y_0 value and low n value (less than 0.93). This indicated that the protective layer on the surface of the Cr-film was not effective. XPS revealed that there were oxide and hydroxide compounds on the surfaces of all films. A high ratio of oxide/hydroxide was found in the CrZr-film providing better protective properties to the film. Chromium content in the CrZr-film plausibly reduced dissolution of zirconium oxide that formed on the CrZr-film surface resulting in a high ratio of oxide/hydroxide.

Chapter 4

Chromium-zirconium nitride film

4.1 Chromium-zirconium nitride film

After successfully fabricated thin amorphous film in chromium-zirconium binary system as shown in the previous chapter, it revealed that addition of zirconium into chromium film could promote amorphization and improve corrosion resistance of films. Therefore, addition of zirconium was integrated to tailor properties of chromium-zirconium nitride (CrZrN) film. Generally, chromium nitride (CrN) is a kind of materials which has been widely used in many applications especially in coating, given its high hardness, good corrosion resistance and low friction coefficient [20-24]. Zirconium also demonstrated a good potential for addition into CrN as well as in metallic film, because of possibility to improve both thermal stability and hardness [25, 27]. However, published reports stated that the addition amount of zirconium was only in small percentages and did not investigate in detail about phase nature of the CrZrN film with a high degree of zirconium addition. Hence, this research aimed to investigate the effect of zirconium addition with a high amount on phase evolution of CrZrN film.

4.2 Film preparation and characterizations

4.2.1 Film preparation

Nitride films were also fabricated by dual-head DC magnetron sputtering with a nitrogen (N_2) as a reactive gas. Films were categorized into three specimens varies on zirconium content according to low zirconium (Low-Zr), medium zirconium

(Med-Zr) and high zirconium (High-Zr). It was controlled by adjusting ratio of applied current of the chromium and zirconium targets as described in table 4-1. Before deposition process, (100) silicon substrates were cleaned ultrasonically in industrial-grade acetone for 600 seconds and placed on substrate holder. Then, the chamber was evacuated to base pressure at 1.33×10^{-2} pascal. High-purity Ar and N₂ (99.995% pure, Linde) were introduced into chamber simultaneously with flow rate of 40 and 4 sccm to obtain a working pressure at 1.13 pascal. A plasma of Ar and N₂ mixture was ignited by using chromium and zirconium targets as cathodes while the chamber served as an anode. The deposition time was kept constant for all nitride films at 3600 seconds. All deposition processes were done without auxiliary heater and bias voltages, and all deposition parameters are listed in table 4-1.

Table 4-1 Details of deposition parameters

Deposition parameters	Coating samples		
	Low-Zr	Med-Zr	High-Zr
Working gas	Argon (99.995% purity), 40 sccm		
Reactive gas	Nitrogen (99.995% purity), 4 sccm		
Based pressure	1.33×10^{-2} Pa		
Working pressure	1.13 Pa		
Target-sample distance	150 mm		
Substrate temperature	318-333 K		
Applied current chromium target (A)	0.4 A	0.4 A	0.3 A
Applied current zirconium target (A)	0.4 A	0.7 A	0.7 A
Deposition time	3600 seconds	3600 seconds	3600 seconds

4.2.2 Material characterizations

Nitride films were firstly observed their cross-sectional microstructure by a JEOL, JSM-7100F field-emission scanning electron microscope (FESEM). The thickness of films was measured by FESEM images using Image J software. Energy dispersion spectroscopy (EDS, Oxford Inca PentaFETx3) was performed for determining bulk chemical composition of films. A Veeco Dimension 3100, atomic force microscope (AFM), was used to observe surface morphology and measure surface roughness with a scanning area of $5 \times 5 \mu\text{m}^2$. Phasic evolution of CrN due to zirconium addition was clarified by using a Rigaku D/Max 2200P/C glancing incident angle X-ray diffractometer (GIXRD) with a $\text{Cu-K}\alpha$ source at an incident angle of 3 degrees, and X-ray photoelectron spectroscopy (XPS, ULVAC-PHI Versa-Probe II) at energy step 0.05 eV using $\text{Al-K}\alpha$ X-ray source. Range of operation was between 20-70° with scan speed 1°/minute.

4.3 Results and discussions

4.3.1 Microstructure and morphology

As well as metallic films, the result of nitride film started with microstructure observation. Reactive magnetron sputtering successfully fabricated nitride films with uniform thickness. Cross-sectional microstructure of nitride films is shown in figure 4-1. They exhibited fine, uniform columnar structure through film thickness without micropores or microcracks for all coating conditions. Thickness of all films measured by image J software was in the range of 1.01-1.30 μm according to deposition rate in the ranged of 0.28 to 0.36 nm/s. The thickest film was found in the Med-Zr condition since the highest total current was applied to both chromium and zirconium target in

order to maintain plasma stability and avoid poisoning target. This high current caused high sputtering rate on targets resulting in slightly higher deposition rate of Med-Zr film comparing to Low-Zr and Med-Zr.

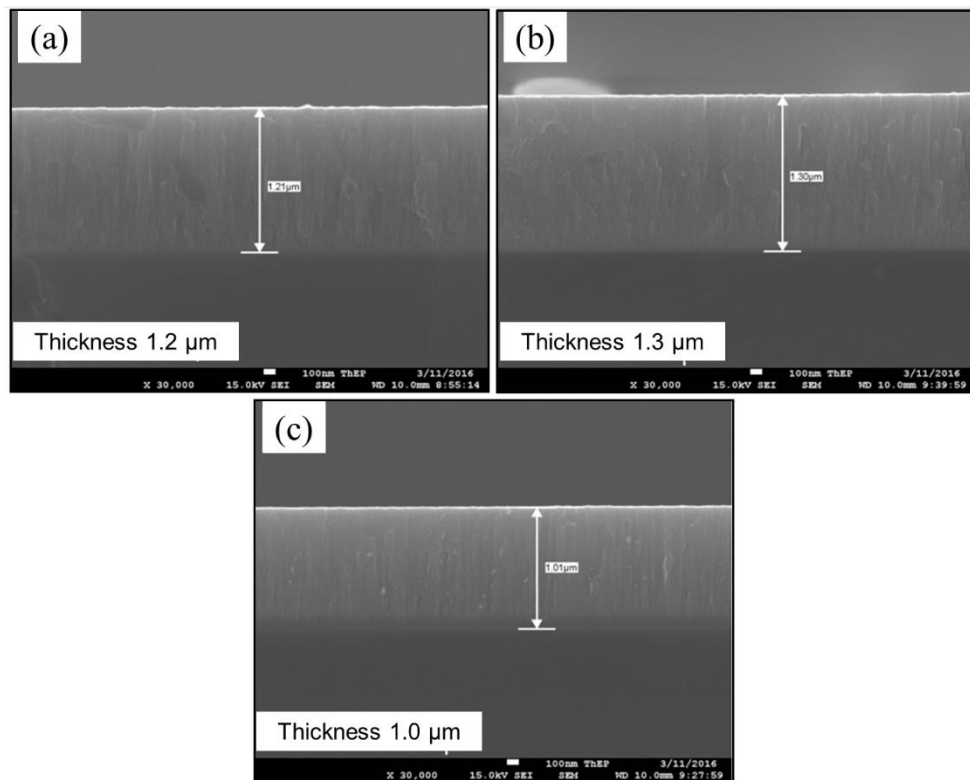


Figure 4-1 Cross-sectional FESEM images of nitride films; (a) Low-Zr, (b) Med-Zr and (c) High-Zr

Surface morphology of nitride films was also investigated by AFM with scanning area $5 \times 5 \mu\text{m}^2$ as shown in figure 4-2. All nitride films exhibited smooth surface with nanoscale of R_a and R_{rms} as listed in table 4-2. Surface of nitride film was slightly smoother with higher zirconium fraction. The details of smoother surface will be discussed in in the further section.

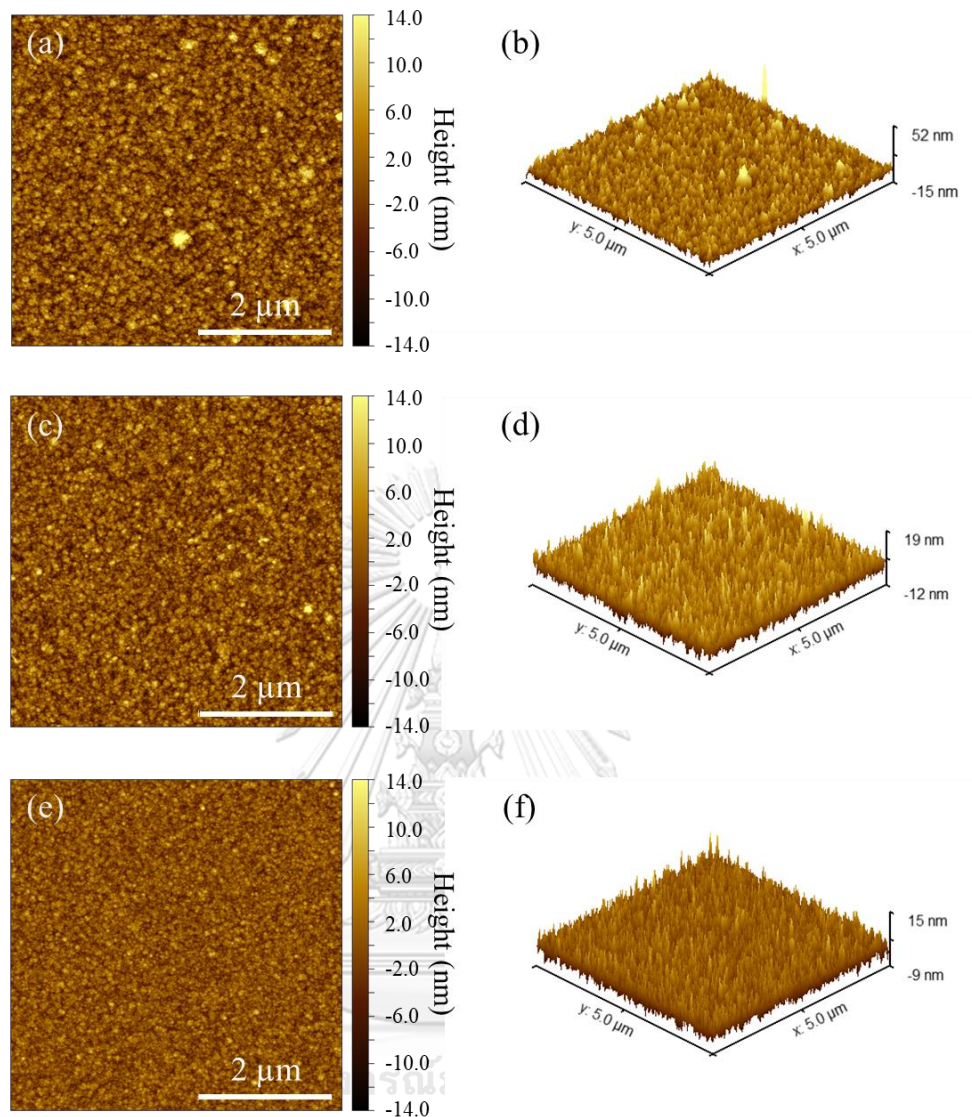


Figure 4-2 AFM topographic images of nitride films

Table 4-2 Surface roughness and chemical compositions of nitride films

Sample	Surface roughness		Composition (%at.)		Zr fraction(x)
	R _a (nm)	R _{rms} (nm)	chromium	zirconium	
Low-Zr	2.8	3.7	32.41	7.29	0.183
Med-Zr	2.5	3.2	22.66	18.21	0.445
High-Zr	1.9	2.4	16.04	22.01	0.578

Chemical composition of the nitride films was measured by EDS analysis as described in table 4-2. Total of chromium and zirconium for all films was

approximately 40 %at. and the rest was light elements of nitrogen and oxygen.

Zirconium fraction (x , $x = \frac{\% \text{at. Zr}}{\% \text{at. Cr} + \% \text{at. Zr}}$) in films increased from 0.183 of Low-Zr to

0.578 of High-Zr. This indicated that zirconium was successfully doped into the

nitride films. Though amount of nitrogen could be achieved by EDS analysis,

reliability of quantitative analysis for light element by EDS was considerably low.

Hence, phasic analysis must be done by other methods such as GIXRD or XPS

analysis.

4.3.2 Phase, chemical composition, and crystallinity

Phase evolution of nitride were investigated by GIXRD and their patterns are shown in figure 4-3. The dominate pattern in all films corresponded to CrN (ICSD 01-076-2494) although those peak positions shifted toward lower degree. Those peaks approached to the positions of ZrN (ICSD 03-065-0972) when increasing zirconium fraction in films. Because they had the same crystal structure (rock salt structure), they could share the sites of cation in lattice and formed as complex nitride of chromium-zirconium, denoted as (Cr,Zr)N. A shift of those peak positions caused by an increasing of zirconium cations in the (Cr,Zr)N lattice. This was supported by the expansion of lattice parameter (a_0) which was calculated by Bradley-Jay extrapolation as shown in figure 4-4. The result revealed that a_0 of (Cr,Zr)N increased with zirconium fraction in film and all calculated a_0 values were between a_0 of CrN and ZrN references. Due to the bigger size of zirconium cation, it expanded base crystal structure of (Cr,Zr)N resulting in the increasing of a_0 in (Cr,Zr)N with Zr fraction in film.

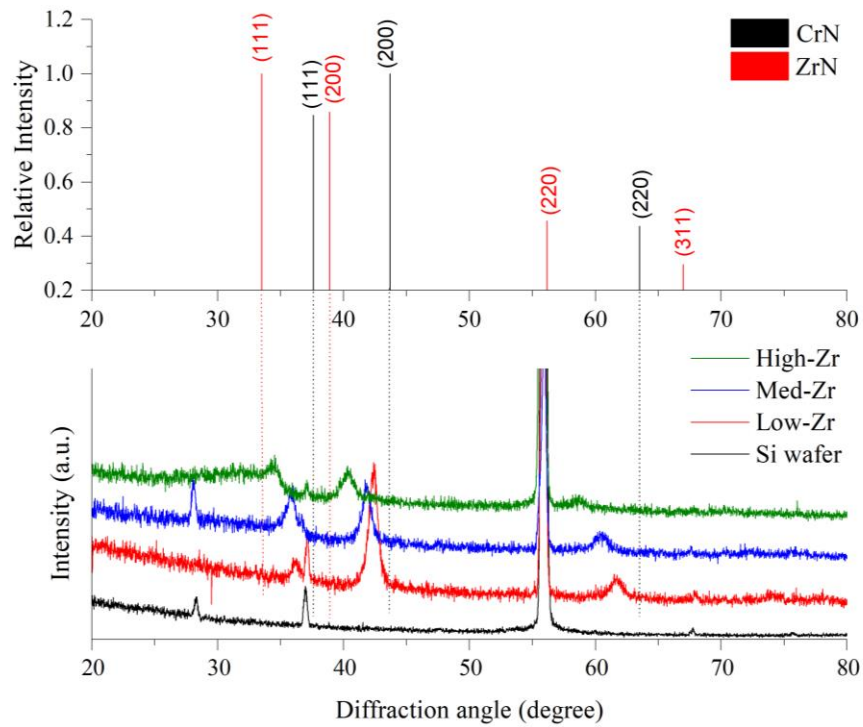


Figure 4-3 XRD patterns of nitride films

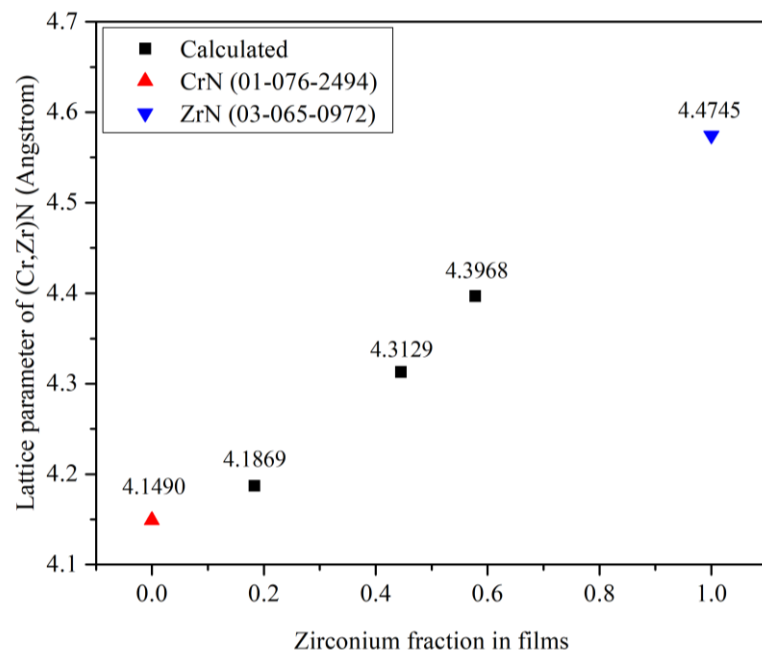


Figure 4-4 Lattice parameter of (Cr,Zr)N with a zirconium fraction in nitride film

Average crystallite size of (Cr,Zr)N was calculated from plane (200) by Scherrer's equation. Crystallite size of Low-Zr, Med-Zr and High-Zr films were 10.2, 9.9 and 7.7 nm; respectively, which slightly decreased with zirconium fraction. Since chromium ion was substituted by zirconium ion, lattice parameter of (Cr,Zr)N was expanded from the equilibrium. From the nano-strain (ϵ) in film calculation as expressed in equation 4-1 [110], strain in all nitride films increased with lattice parameter or zirconium fraction. The a_i represented to distortion lattice parameter and $a_{0,ref}$ is the lattice parameter of CrN (4.1409 Å). The higher number of substituted zirconium ions expanded crystal and created strain energy which limited crystal growth of the (Cr,Zr)N [111]. This was also supported by the AFM result and Ohring, that refine structure led to smoother surface [64]. Hence, smoother surface of the CrZrN film could be achieved by increasing zirconium fraction.

$$\epsilon = \frac{a_i - a_{0,ref}}{a_{0,ref}} \quad (\text{equation 4-1})$$

Furthermore, the High-Zr film had one more broaden peak (27-34°) among (Cr,Zr)N peaks which could not clearly identify by XRD. To investigate phase evolution and distinguish this broaden peak in more details, XPS was employed for examine these films due to the higher sensitivity than XRD. The XPS investigation of nitride films were performed in the range of Cr 2p_{3/2}, Zr 3d, N 1s and O 1s spectra. All spectra were collected after surface sputtering for eliminating contaminants, and were calibrated with carbon 1s (285.0 eV). The Cr 2p_{3/2} spectra of all nitride films could be deconvoluted into two peaks as shown in figure 4-5, attributing to the binding energy of Cr 2p_{3/2} in Cr₂O₃ at 576.4±0.1 eV and CrN at 574.5±0.2 eV [28, 89, 112, 113]. Herein, the binding energy of CrN represented to bonding of Cr-N in

(Cr,Zr)N. The presence of Cr_2O_3 peak was plausibly from reaction of chromium and residual oxygen in chamber during film deposition. Amount of Cr_2O_3 slightly decreased with increasing zirconium fraction in film, as seen by a decreasing of Cr_2O_3 intensity. This result agreed with Ellingham's diagram, revealed that Cr_2O_3 could be reduced by zirconium.

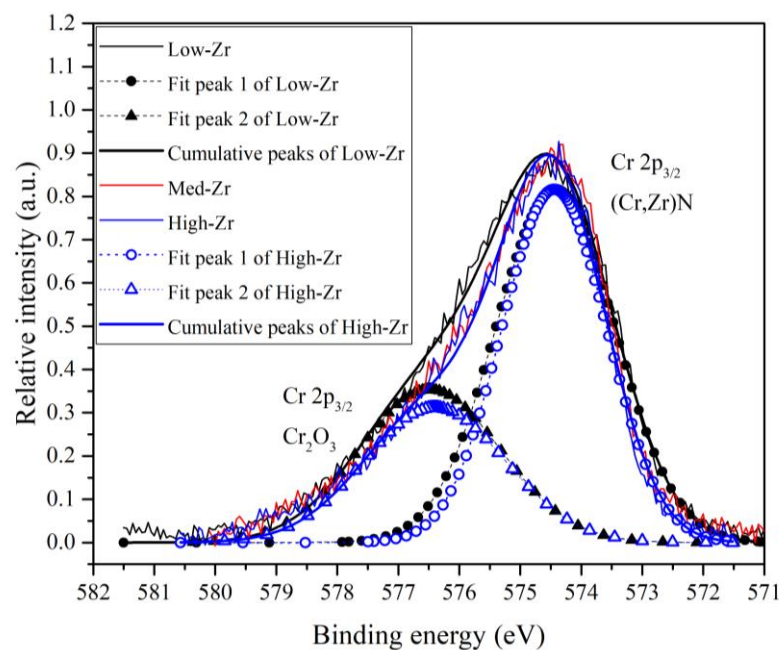


Figure 4-5 XPS spectra of $\text{Cr } 2p_{3/2}$ in nitride films

In the case of Zr 3d spectra (figure 4-6), they could be deconvoluted into four peaks corresponding to binding energy of ZrN ($\text{Zr } 3d_{5/2} = 180.4 \text{ eV}$ and $\text{Zr } 3d_{3/2} = 183.3 \text{ eV}$) and zirconium oxynitride (Zr_2ON_2 ; $\text{Zr } 3d_{5/2} = 181.5 \text{ eV}$ and $\text{Zr } 3d_{3/2} = 184.3 \text{ eV}$). Binding energy of ZrN presented to the bonding of Zr-N in (Cr,Zr)N as well as in the $\text{Cr } 2p_{3/2}$ spectra. The values of (Cr,Zr)N and Zr_2ON_2 in this report were in agreement with another reports [114, 115]. The formation of Zr_2ON_2 was from the reaction of zirconium with residual gas during film deposition. Noteworthy, the XPS result revealed that zirconium preferentially formed in Zr_2ON_2 although the Zr_2ON_2

peak could not be detected in the XRD result. The absence of Zr_2ON_2 peak in the XRD patterns might be due to the nature of amorphous structure and a small amount of the oxynitride. At this point, it could be concluded that added zirconium would form in two compounds as in crystalline- $(Cr,Zr)N$ and amorphous- Zr_2ON_2 . Amount of these phases was discussed in further section.

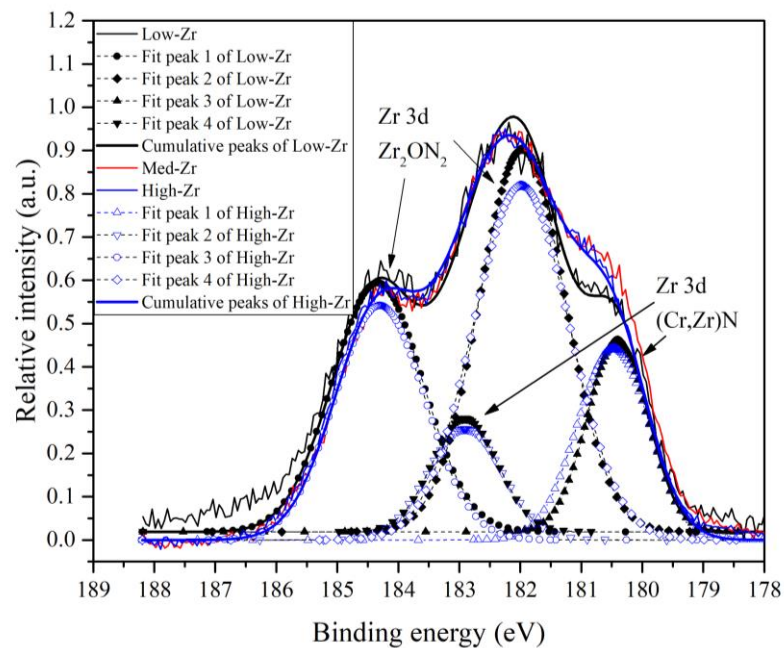


Figure 4-6 XPS spectra of Zr 3d in nitride films

The XPS of N 1s spectra was the other key for phase investigation because it was an elemental of the $(Cr,Zr)N$ and Zr_2ON_2 . It was found that the profiles of N 1s slightly translated from high to low binding energy as shown in figure 4-7. According to literature reviews, the binding energy of N 1s in CrN, ZrN and Zr_2ON_2 was 396.7, 395.9 and 395.5 eV, respectively [116, 117]. This implied that the amount of nitrogen in form of Zr_2ON_2 and bonding of Zr-N in $(Cr,Zr)N$ increased with zirconium fraction in film. This was in good agreement with the Zr 3d spectra which revealed that amount of Zr_2ON_2 and number of dissolved zirconium in $(Cr,Zr)N$ increased with

zirconium fraction. In addition, XPS spectra of O 1s also demonstrated to the presence of Cr_2O_3 and Zr_2ON_2 as seen by well deconvoluted of two peaks attributing to O 1s of Cr_2O_3 (531.2 eV) and Zr_2ON_2 (529.6 eV), as shown in figure 4-8. These values agreed with another reports [113, 118], and correlated well with other XPS results.

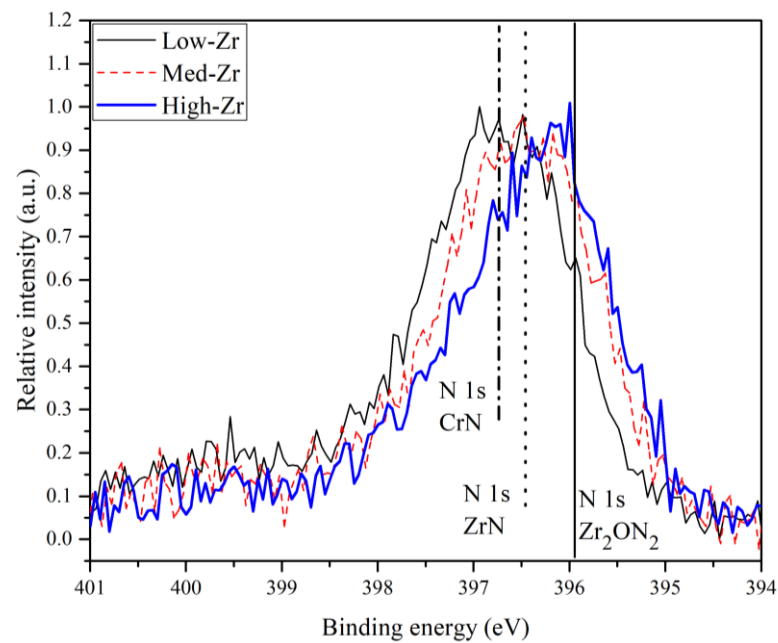


Figure 4-7 XPS spectra of N 1s in nitride films

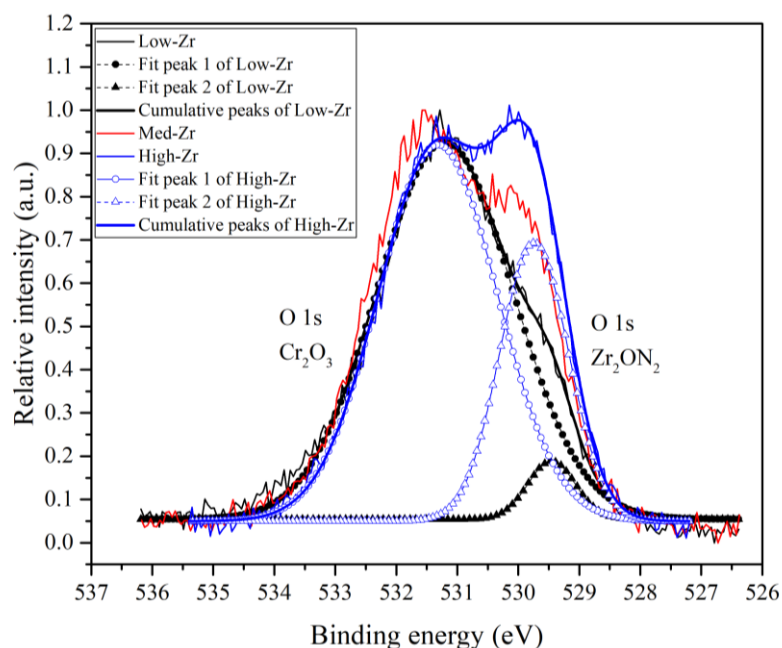


Figure 4-8 XPS spectra of O 1s in nitride films

Integrating the XPS results of Zr 3d and Cr 2p_{3/2} spectra with quantitative analysis by EDS, amount of zirconium in (Cr,Zr)N and Zr₂ON₂ could be calculated as shown in table 4-3. As previously described that zirconium formed in both of (Cr,Zr)N and Zr₂ON₂. The amount of zirconium in form of Zr₂ON₂ was about 1.5-2.5 times of zirconium in form of (Cr,Zr)N. Therefore, it confirmed that zirconium preferentially form in amorphous-Zr₂ON₂, while chromium preferentially formed in (Cr,Zr)N and was the predominant elemental cation in (Cr,Zr)N.

Table 4-3 Amount of chromium and zirconium in each compound calculated by EDS and XPS results

Sample	Amount of chromium (%at.)		Amount of zirconium (%at.)	
	(Cr,Zr)N	Cr ₂ O ₃	(Cr,Zr)N	Zr ₂ ON ₂
Low-Zr	25.28	7.13	2.00	5.29
Med-Zr	17.68	4.98	7.07	11.14
High-Zr	12.52	3.52	8.72	13.29

Finally, from the calculation of EDS and XPS, it could be concluded that all nitride films composed of 3 compounds: Cr_2O_3 , $(\text{Cr,Zr})\text{N}$ and Zr_2ON_2 . Amounts of cations in these compounds was calculated and showed in figure 4-6. The $(\text{Cr,Zr})\text{N}$ was the dominant compound existing with Cr_2O_3 and Zr_2ON_2 for all nitride films. Only the Zr_2ON_2 from all, its amount increased with zirconium fraction in films. Therefore, it was reasonable that the low intensity boarded peak in XRD result of High-Zr film was belonged to the Zr_2ON_2 compound. Addition of zirconium into CrZrN film refined crystallite size of $(\text{Cr,Zr})\text{N}$ and also promoted amorphization of Zr_2ON_2 .

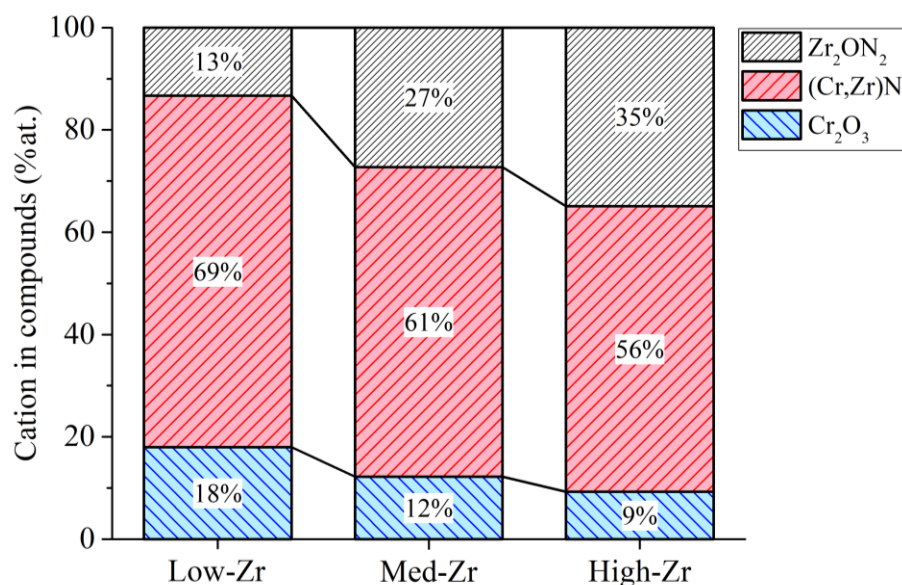


Figure 4-9 Compound fraction in nitride films

4.3.3 Effect of interlayer addition and corrosion property

From the industrial film preparation point of view, plasma ignition in deposition process usually starts from only a working gas then introducing a reactive gas into chamber. This process causes to a presence of thin metal film between the top nitride film and substrate. Therefore, researchers decided to apply an interlayer and

investigate its effect to a possibility of amorphization in the CrZrN film. It has been reported that amorphous interlayer could promote amorphous structure in the top layer [32, 56]. Hence, the moderate mixture of chromium and zirconium film, which exhibited amorphous structure, could be employed as amorphous interlayer for promoting amorphous structure in the CrZrN film. The Med-Zr film was chosen for representative of the top nitride film due to no evidence of amorphous in this film. The specimen of this chromium-zirconium interlayer with the top Med-Zr film is denoted as Int.-MedZr. Deposition parameters of the interlayer and top-nitride film are summarized in table 4-4. The interlayer (CrZr-interlayer) was firstly deposited on substrates by magnetron co-sputtering with only argon gas for 15 minutes, then introduced nitrogen gas for prepare the top nitride film for 60 minutes.

Table 4-4 Deposition parameters of Int.-MedZr

Layers	Cr target	Zr target	Deposition	Ar flow	N ₂ flow
CrZr-interlayer	0.4 A	0.7 A	15 minutes	20 sccm	-
Med-nitride	0.4 A	0.7 A	60 minutes	20 sccm	4 sccm

The FESEM images (figure 4-10) clearly demonstrated that film covered the entire surface with uniform thickness. Featureless structure could be observed in both of interlayer and nitride layer as shown in figure 4-10(a). The junction between them was clearly distinguished by back scattering electron (BSE) image in figure 4-10(b). The average thickness of interlayer and nitride were 234 and 828 nm, respectively. Topographic images of the Int.-MedZr film by AFM are presented in figure 4-11. This film exhibited very smooth surface with R_a at 2.2 nm and R_{rms} at 2.8 nm. There was no significantly difference in surface roughness between the MedZr film and Int.-MedZr.

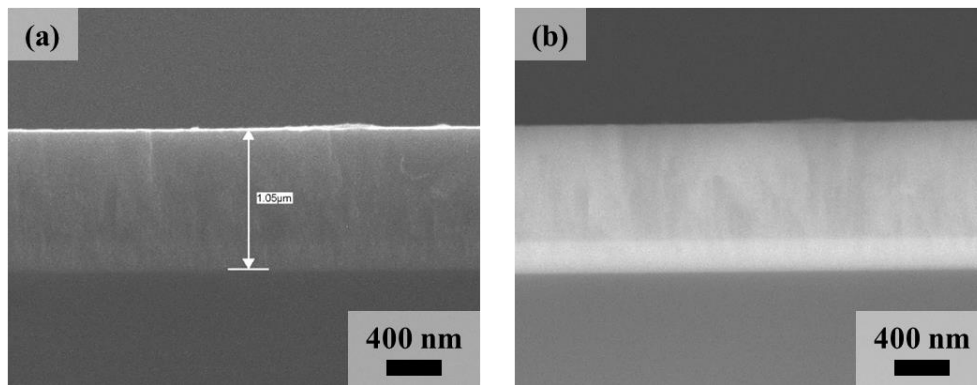


Figure 4-10 FESEM images of the Int.-MedZr film: (a) SEM image and (b) BSE image

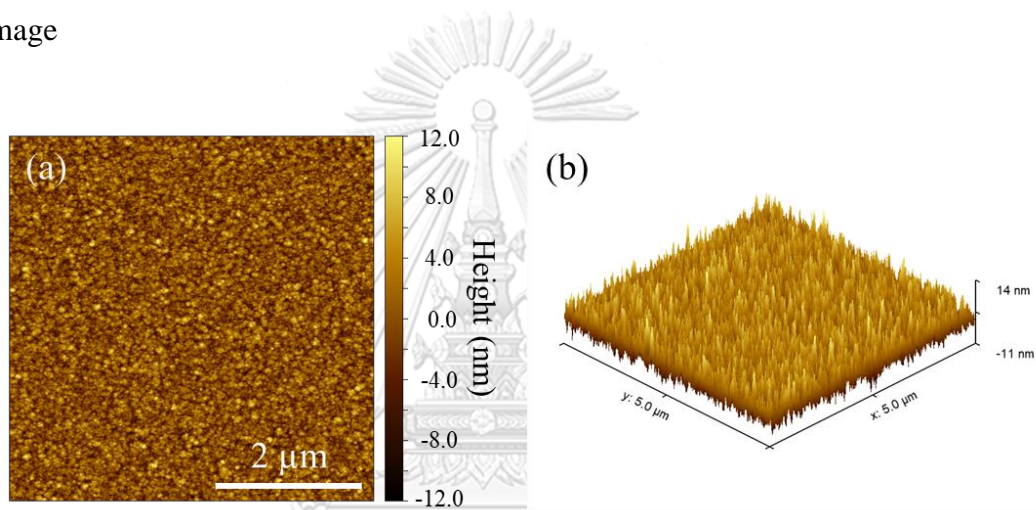


Figure 4-11 AFM Topographic images of the Int.-MedZr film

Phase and crystallinity of the Int.-MedZr film were also performed by GIXRD and comparing to the Med-Zr film (no interlayer). Interestingly, the XRD pattern of the Int.-MedZr film showed the characteristic of amorphous structure (broaden peak) instead of crystalline structure like the Med-Zr film as shown in figure 4-12. This result showed that amorphous of CrZrN film could be promoted by addition of chromium and zirconium interlayer.

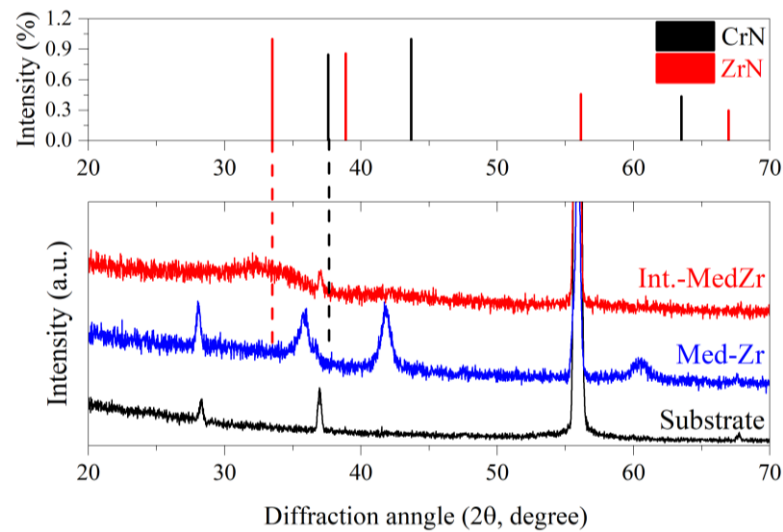


Figure 4-12 XRD patterns of Int.-Med-Zr film and Med-Zr

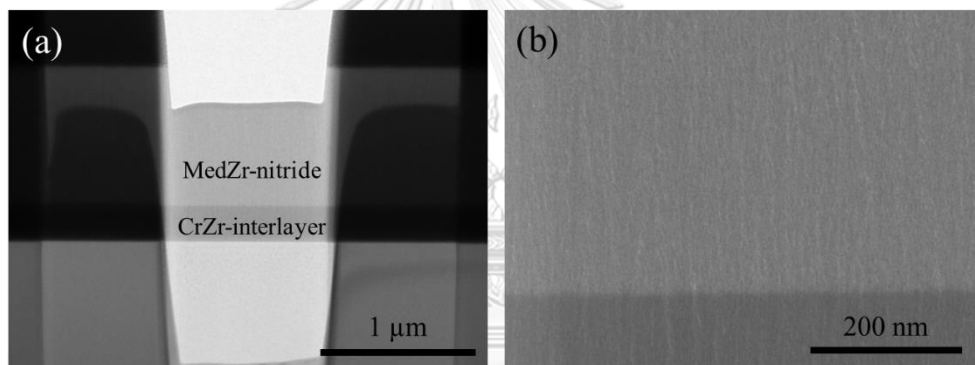


Figure 4-13 Out-view TEM image of the Int.-MedZr film

To confirm crystallinity of both interlayer and top nitride layer, the Int.-MedZr film was investigated by TEM and EDP. Out-view TEM image of the Int-MedZr film clearly demonstrated the junction between interlayer and nitride by contrast of each layer as shown in figure 4-13. Their thicknesses were agreed with the FESEM result. No evidence of columnar structure was found in the TEM image (figure 4-13(b)) as well as in the FESEM image. Close-up HRTEM image at the junction is shown in figure 4-14. The nitride layer grew on the interlayer without explicit interface. This suggested that nitride layer continuously growth from the interlayer surface.

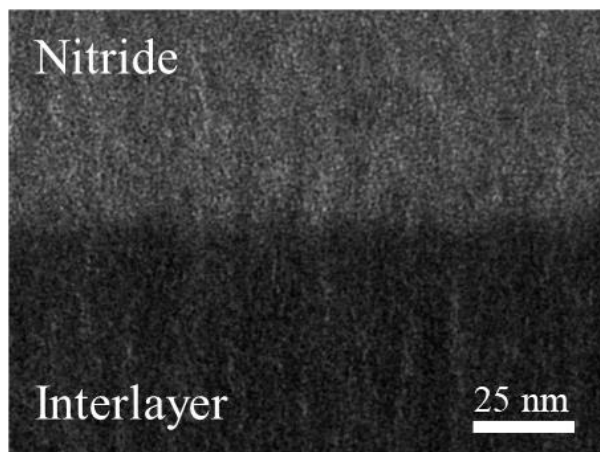


Figure 4-14 HRTEM image at junction between interlayer and nitride of the Int.-MedZr

Crystallinity of interlayer was confirmed by selected area of HRTEM and EDP. The HRTEM image of interlayer (figure 4-15(a)) revealed only a random atomic arrangement attributing to characteristic of amorphous structure. According to the EDP in figure 4-15(b), it revealed only the diffuse ring corresponding to amorphous structure. It could be concluded that the CrZr-interlayer was amorphous structure as well as the result in chapter 3.

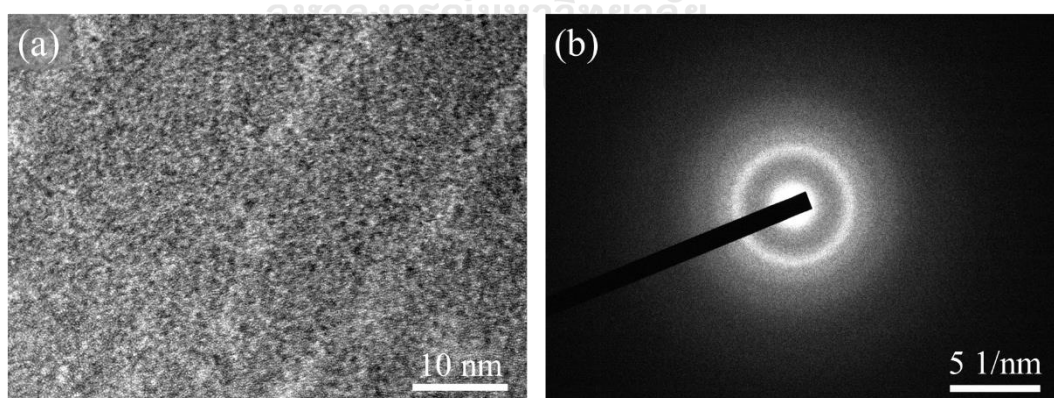


Figure 4-15 HRTEM image and EDP in the interlayer area of Int.-MedZr film

The HRTEM image and EDP in the nitride area of Int.-MedZr film are shown in figure 4-16 and 17. Almost of nitride film exhibited amorphous structure as shown

in figure 4-16(a) and (b). However, the selected area in nitride film exhibited a diffuse ring existing with spots and crystalline ring as shown in figure 4-17. It revealed a few areas of ordering arrangement embedded in amorphous matrix. These implied to a short-range order structure existing with amorphous matrix in the top nitride layer.

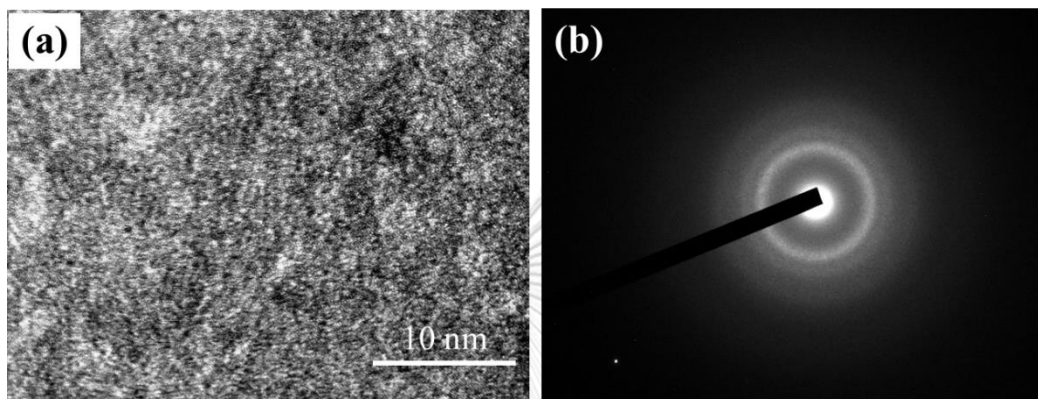


Figure 4-16 HRTEM image and EDP in the nitride area of Int.-MedZr film

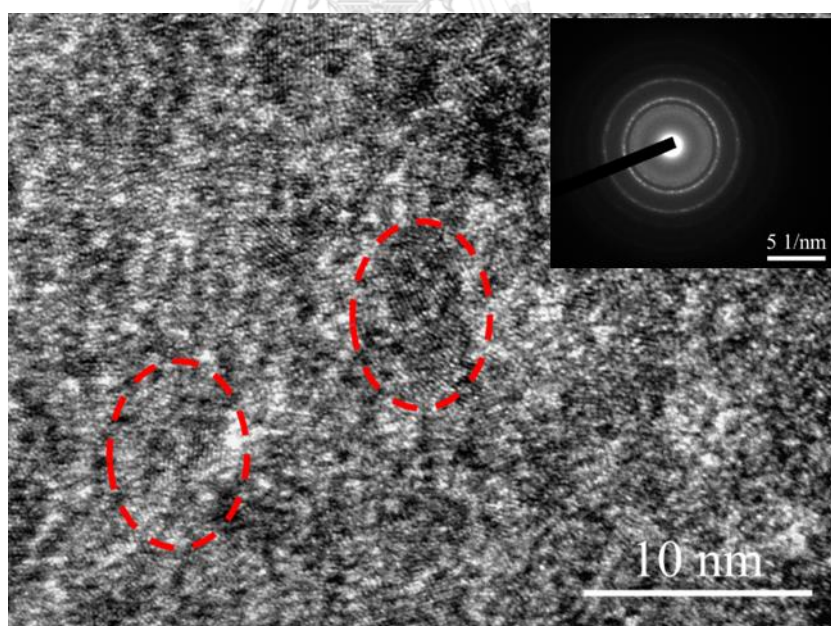


Figure 4-17 HRTEM image in the nitride area of Int.-MedZr film

The reciprocal space of EDP in figure 4-17 was calculated and displayed in figure 4-18. The real space and diffraction angle of diffuse ring corresponded to the broaden peak in the previous XRD result. The first and second crystalline rings

corresponded to the (200) and (220) peak of (Cr,Zr)N. Therefore, it was reasonable that the ordering arrangement area in figure 4-17 corresponded to the area of a crystalline structure of (Cr,Zr)N.

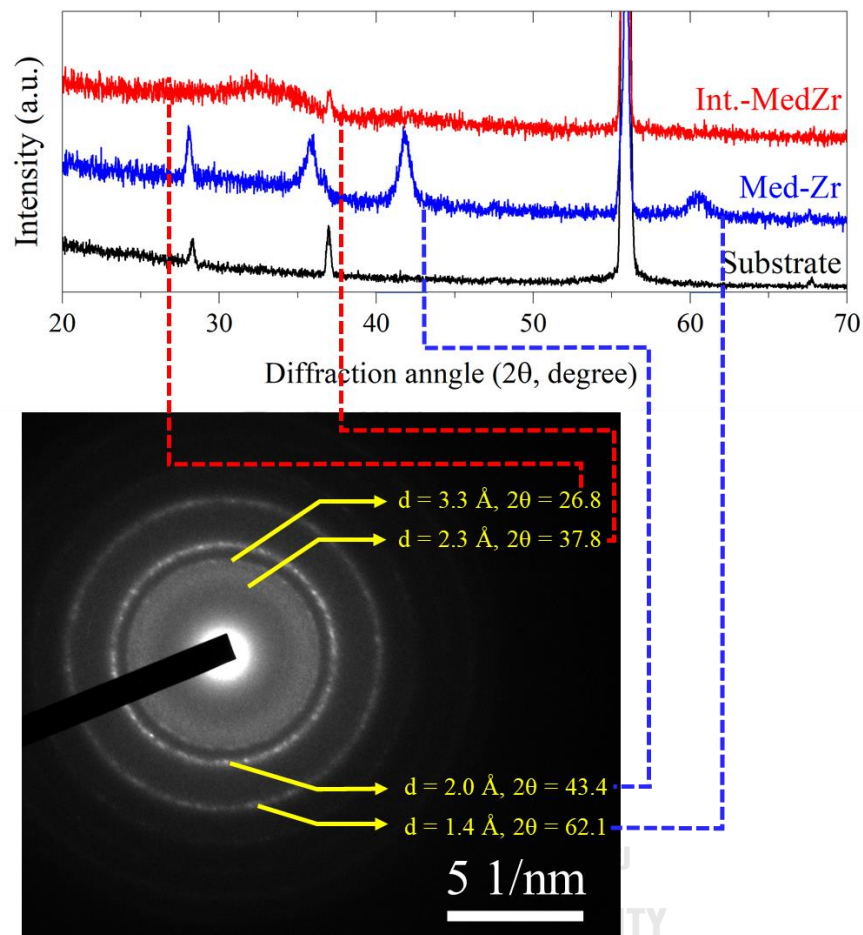


Figure 4-18 EDP of the top nitride and calculated real space

Therefore, addition of amorphous CrZr-interlayer could promote amorphous structure in the top nitride layer of CrZrN although there was presence of a few ordering arrangement of (Cr,Zr)N in some area. It was suggested that the amorphous interlayer performed as a “random arrangement template” for the top nitride deposition. Incorporating with the near chemical compositions between interlayer/nitride layer and low adatoms mobility, adatoms in the nitride deposition period continuously growth from the random arrangement template. As a result, the

top nitride film (Med-Zr) preferred to being amorphous structure in instead of being as a crystalline film.

Corrosion of the Int.-MedZr film was also investigated by potentiodynamic polarization under 3.5 %wt. NaCl solution. The Int.-MedZr greatly reduced the I_{corr} from 2.28×10^{-6} of bare H13 substrate to 3.12×10^{-9} A/cm² and improved E_{corr} to -354 mV as shown in figure 4-19. In addition, it also had a better anti-corrosion property than the amorphous CrZr-film and other nitride films in several reports [25, 77, 119-121]. The good anti-corrosion property of this film plausibly obtained from the amorphous formation in top nitride film and the presence of a good anti-corrosion property of CrZr-interlayer. Although partially corrosive solution penetrated through the top nitride film, it was again retarded by interlayer which also had a good corrosion property. Therefore, the Int.-MedZr film was the best anti-corrosion film among other film in this research.

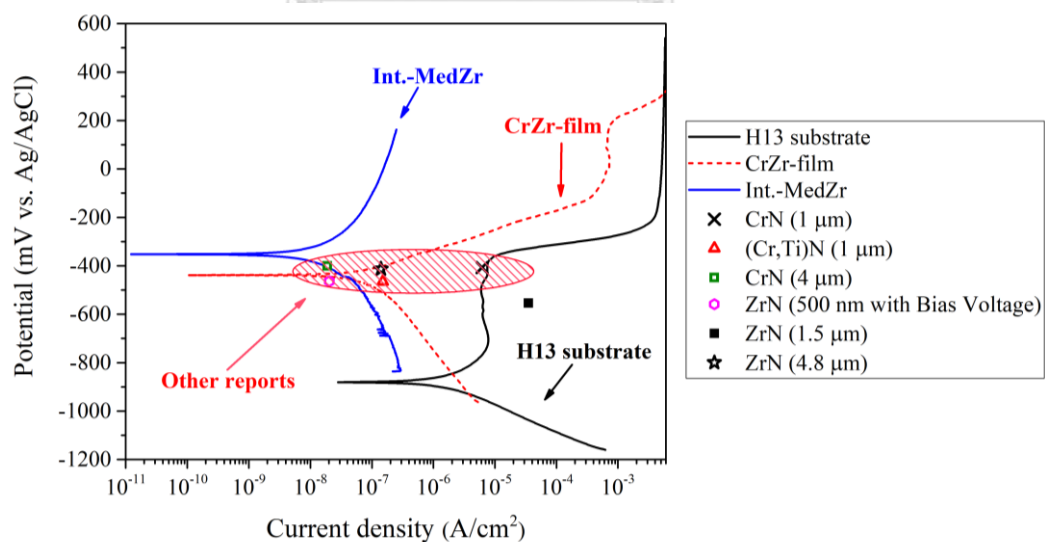


Figure 4-19 Potentiodynamic polarization of Int.-MedZr comparing with other reports

4.4 Summary

Nitride film of CrZrN exhibited columnar structure through uniform thickness in 1.0-1.3 μm and nanoscale surface roughness. By material design, addition of zirconium refined the crystalline size of (Cr,Zr)N which was the predominant phase of this nitride films existing with Cr_2O_3 and amorphous Zr_2ON_2 . The higher addition of zirconium more refined the crystallite size of (Cr,Zr)N from 10.2 to 7.7 nm due to lattice distortion (strain energy), and simultaneously promoted formation of amorphous Zr_2ON_2 . Addition of zirconium at 0.578 atomic fraction significantly promoted amorphous structure in nitride film which was enough for detected by XRD as seen by the broaden peak.

By addition of amorphous CrZr-interlayer or interface modification, this specimen composed uniform thickness of interlayer and nitride for 234 and 828 nm; respectively, with nanoscale surface roughness. There was no evidence of columnar structure (featureless) in both of interlayer and nitride layer. For phase identification, addition of amorphous interlayer could promote amorphization in the top Med-Zr nitride film. The amorphous interlayer performed as a “random arrangement template” for sequentially nitride layer. Because of the near chemical compositions between interlayer/nitride layer and low adatoms mobility, adatoms in the nitride deposition period continuously grew up from the random arrangement template of interlayer. As a result, this top nitride film (Med-Zr) preferred to being amorphous structure instead of being as a crystalline film.

In term of corrosion testing, the Int.-MedZr film greatly reduced I_{corr} and improved E_{corr} of bare H13 substrate and showed the best anti-corrosion film over the

amorphous CrZr-film and other reported films. The excellent anti-corrosion property of the Int.-MedZr film plausibly obtained from the amorphous featureless structure in both of top nitride film and CrZr-interlayer. Corrosive solution hardly penetrated through the top nitride film. Consequently, the Int.-MedZr film was the best anti-corrosion film among other film in this research.



Chapter 5

Conclusions

5.1 Chromium-zirconium metallic film

Thin metallic films of chromium, zirconium, and mixture of them were successfully fabricated by magnetron co-sputtering. All films covered substrate with uniform thickness in the range of 390-450 nm and nanoscale surface roughness. The pure component films exhibited a characteristic of columnar-crystalline structure while the moderate mixture film was featureless-amorphous structure. Phase identification performing by GIXRD indexed that the Cr-film was BCC-chromium and the Zr-film corresponded to HCP-zirconium with a small amount of ZrO_2 .

Corrosion behavior of all specimens were investigated by OCP measurement, EIS with equivalent circuit interpretation and potentiodynamic polarization in 3.5 % wt. NaCl solution. Microstructure and crystallinity of films strongly affected to film resistance (R_{film}), corrosion potential (E_{corr}) and passivation ability. The featureless-amorphous CrZr-film showed the best anti-corrosion properties among other films due to the low susceptible point such as grain boundary and intercolumnar, leading to the highest film resistance (R_{film}) and corrosion potential (E_{corr}). Moreover, the featureless (no intercolumnar) in this film could retard a solution penetration leading to successful and effective passivation. In contrast, columnar structure in the Cr-film and Zr-film poorly retarded a penetration because solution could directly penetrate through film via intercolumnar. As a result, although the Cr-film and Zr-film had an ability to passivation after increasing potential, corrosion favorably took place at substrate surface instead of film after it reached to substrate. Therefore, their passive

films were not effective as seen by the high passive current (I_{pass}) which were higher than 10^{-3} A/cm².

Furthermore, zirconium played the important role to pre-native oxide film on surface as seen by the high impedance of film capacitance (Q_{film}) in Zr-film and CrZr-film. The formation of zirconium oxide as a protective layer is more effective than chromium oxide. This attributed to a retarding yield of corrosion reaction at solution/film interface as could be seen from the low values of admittance (Y_0) and high n (close to unity). In contrast, the Cr-film exhibited a high Y_0 with low n (less than 0.93) indicating to a low protectiveness.

XPS analysis revealed that there were presence of oxide and hydroxide compounds after corrosion testing in all films. However, the highest oxide/hydroxide ratio was found in the CrZr-film providing a better protective property to this film. The presence of chromium in the CrZr-film plausibly reduced dissolution of zirconium oxide that formed on this surface resulting in the high ratio of oxide/hydroxide compounds and a good anti-corrosion property of the CrZr-film.

5.2 Chromium-zirconium nitride film

Chromium-zirconium nitride films were also successfully fabricated by magnetron co-sputtering with argon and nitrogen as a working gas and reactive gas. The composition of chromium and zirconium in nitride films could be adjusted by controlling of applied current as seen by the zirconium fraction in Low-Zr, Med-Zr and High-Zr film. All nitride films showed columnar structure through films with uniform thickness in the range of 1.0-1.3 micron and nanoscale surface roughness.

From phase identification, complex nitride of chromium and zirconium denoted as (Cr,Zr)N, was the predominant phase existing with a small amount of amorphous zirconium oxynitride (Zr_2ON_2). Addition of zirconium refined crystallite size of (Cr,Zr)N from 10.2 to 7.7 nm with the higher zirconium fraction due to lattice disorder (strain energy) from size difference of dissolving zirconium ion. This strain confined crystal growth resulting in a smaller crystallite size.

By XPS analysis, amorphous Zr_2ON_2 was presence in all nitride films and its amount increased with zirconium fraction. With a higher zirconium fraction, an amount of undissolving zirconium was greater and reacted with residual gas forming to amorphous oxynitride. Therefore, amorphous Zr_2ON_2 and fined crystalline (Cr,Zr)N could be achieved by addition of zirconium into chromium nitride. Addition of zirconium at 0.578 atomic fraction significantly promoted amorphous structure in nitride film as seen by the broaden peak in XRD pattern of High-Zr film.

Furthermore, addition of amorphous CrZr-interlayer could promote amorphous structure in the top Med-Zr nitride film. The amorphous interlayer performed as a “random arrangement template” for sequentially nitride layer. Because of the near chemical compositions between interlayer/nitride layer and low adatoms mobility, adatoms in the nitride deposition period continuously grew up from the random arrangement template of interlayer. As a result, the top nitride film (Med-Zr) with interlayer preferred to being amorphous structure instead of being as a crystalline film.

Corrosion of the Int.-MedZr film was also investigated by potentiodynamic polarization. The Int.-MedZr film greatly reduced I_{corr} and improved E_{corr} of bare H13

substrate and showed the best anti-corrosion film over the amorphous CrZr-film. The excellent anti-corrosion property of the Int.-MedZr film plausibly obtained from the amorphous structure in both of top nitride film and CrZr-interlayer. Even if, partially corrosive solution penetrated through the top nitride film, it was still retarded by interlayer which also had a good corrosion property. Consequently, the Int.-MedZr film was the best anti-corrosion film among other film in this research.



REFERENCES

- [1] Y. Tsustumi, H. Doi, N. Nomura, M. Ashida, P. Chen, A. Kawasaki, *et al.*, "Surface Composition and Corrosion Resistance of Co-Cr Alloys Containing High Chromium," *Materials Transactions*, vol. 57, pp. 2033-2040, 2016.
- [2] K. Hashimoto, N. Kumagai, H. Yoshika, J. H. Kim, E. Akiyama, H. Habazaki, *et al.*, "Corrosion-resistant amorphous surface alloys," *Corrosion Science*, vol. 35, pp. 363-370, 1993.
- [3] M.S. Idora, M.M. Rahman, M. Ismail, and W. B. W. Nik, "Effect of Zinc Coating Thickness on Corrosion Performance of Mild Steel in Atmospheric and Seawater Environment," *Applied Mechanics and Materials*, vol. 554, pp. 213-217, 06/01 2014.
- [4] V. Schroeder, C. J. Gilbert, and R. O. Ritchie, "Comparison of the corrosion behavior of a bulk amorphous metal, $Zr_{41.2}Ti_{13.8}Cu_{12.5}Ni_{10}Be_{22.5}$, with its crystallized form," 1998-04-14 1998.
- [5] L. Sziráki, E. Kuzmann, K. Papp, C. U. Chisholm, M. R. El-Sharif, and K. Havancsák, "Electrochemical behaviour of amorphous electrodeposited chromium coatings," *Materials Chemistry and Physics*, vol. 133, pp. 1092-1100, 2012/04/16/ 2012.
- [6] D. P. Wang, S. L. Wang, and J. Q. Wang, "Relationship between amorphous structure and corrosion behaviour in a Zr–Ni metallic glass," *Corrosion Science*, vol. 59, pp. 88-95, 2012/06/01/ 2012.
- [7] Z. M. Wang, J. Zhang, X. C. Chang, W. L. Hou, and J. Q. Wang, "Structure inhibited pit initiation in a Ni–Nb metallic glass," *Corrosion Science*, vol. 52, pp. 1342-1350, 2010/04/01/ 2010.
- [8] B. P. Zhang, A. Kawashima, H. Habazaki, K. Asami, and K. Hashimoto, "The effect of structural heterogeneity on the pitting corrosion behavior of melt-spun amorphous Ni–Zr alloys," *Corrosion Science*, vol. 39, pp. 2005-2018, 1997/10/01/ 1997.
- [9] D. Landolt, C. Robyr, and P. Mettraux, "Microstructure and Corrosion Resistance of Sputter-Deposited Titanium-Chromium Alloy Coatings," *Corrosion*, vol. 54, 10/01 1998.
- [10] M. Kitada and F. Kirino, "Effects of Sputter Order and Oxide Layer on Amorphous Formation of Zr-Ni Thin Film System," *MATERIALS TRANSACTIONS*, vol. 46, pp. 277-280, 2005.
- [11] B. Mallia and P. A. Dearnley, "The corrosion–wear response of Cr–Ti coatings," *Wear*, vol. 263, pp. 679-690, 2007/09/10/ 2007.
- [12] J. D. Schuler and T. J. Rupert, "Materials selection rules for amorphous complexion formation in binary metallic alloys," *Acta Materialia*, vol. 140, pp. 196-205, 2017/11/01/ 2017.
- [13] H. Skliarova, O. Azzolini, R. R. Johnson, and V. Palmieri, "Co-sputtered amorphous Nb–Ta, Nb–Zr and Ta–Zr coatings for corrosion protection of cyclotron targets for [18F] production," *Journal of Alloys and Compounds*, vol. 639, pp. 488-495, 2015/08/05/ 2015.
- [14] T. L. Yau and V. E. Annamalai, "Corrosion of Zirconium and its Alloys," in *Reference Module in Materials Science and Materials Engineering*, ed: Elsevier, 2016.

- [15] F. Ali, M. Mehmood, A. M. Qasim, J. Ahmad, R. Naeem ur, M. Iqbal, *et al.*, "Comparative study of the structure and corrosion behavior of Zr-20%Cr and Zr-20%Ti alloy films deposited by multi-arc ion plating technique," *Thin Solid Films*, vol. 564, pp. 277-283, 2014/08/01/ 2014.
- [16] M. Sandhyarani, N. Rameshbabu, K. Venkateswarlu, D. Sreekanth, and C. Subrahmanyam, "Surface morphology, corrosion resistance and in vitro bioactivity of P containing ZrO₂ films formed on Zr by plasma electrolytic oxidation," *Journal of Alloys and Compounds*, vol. 553, pp. 324-332, 2013/03/15/ 2013.
- [17] B. Wang, K. K. Xu, X. H. Shi, M. Zhang, J. W. Qiao, C. H. Gao, *et al.*, "Electrochemical and chemical corrosion behaviors of the in-situ Zr-based metallic glass matrix composites in chloride-containing solutions," *Journal of Alloys and Compounds*, vol. 770, pp. 679-685, 2019/01/05/ 2019.
- [18] R.-r. Sun, S.-t. Xu, M.-y. Yao, J. Zhang, X. Dai, J. Huang, *et al.*, "Effect of dissolved oxygen on corrosion behavior of Zr-0.85Sn-0.16Nb-0.37Fe-0.18Cr alloy in 500 °C and 10.3 MPa super-heated steam," *Transactions of Nonferrous Metals Society of China*, vol. 30, pp. 701-709, 2020/03/01/ 2020.
- [19] C. L. Qin, J. J. Oak, N. Ohtsu, K. Asami, and A. Inoue, "XPS study on the surface films of a newly designed Ni-free Ti-based bulk metallic glass," *Acta Materialia*, vol. 55, pp. 2057-2063, 2007/04/01/ 2007.
- [20] S. Khamseh and H. Araghi, "A study of the oxidation behavior of CrN and CrZrN ceramics thin films prepared in a magnetron sputtering system," *Ceramics International*, vol. 42, pp. 9988-9994, 2016.
- [21] Jacek Jagielski, A.S. Khanna, Jacek Kucinski, D.S. Mishra, P. Racolta, Piran Sioshansi, *et al.*, "Effect of chromium nitride coating on the corrosion and wear resistance of stainless steel," *Applied Surface Science*, vol. 156, pp. 47-64, 2000.
- [22] A. Barata, L. Cunha, and C. Moura, "Characterisation of chromium nitride films produced by PVD techniques," *Thin Solid Films*, vol. 398-399, pp. 501-506, 2001.
- [23] S.H. Ahn, Y.S. Choi, J.G. Kim, and J. G. Han, "A study on corrosion resistance characteristics of PVD Cr-N coated steels by electrochemical method," *Surface and Coatings Technology*, vol. 150, pp. 319-326, 2002.
- [24] Y. Mizuno, T. Nakayama, H. Suematsu, and T. Suzuki, "Characterization of CrN-based hard coating materials with addition of GaN," *Materials Transactions*, vol. 59, pp. 1574-1577, 2018.
- [25] Z.G. Zhang, O. Rapaud, N. Bonasso, D. Mercs, and C. Coddet, "Microstructures and corrosion behaviors of Zr modified CrN coatings deposited by DC magnetron sputtering," *Vacuum*, vol. 82, pp. 1332-1336, 2008.
- [26] S.-F. Chen, Y.-C. Kuo, C.-J. Wang, S.-H. Huang, J.-W. Lee, Y.-C. Chan, *et al.*, "The effect of Cr/Zr chemical composition ratios on the mechanical properties of CrN/ZrN multilayered coatings deposited by cathodic arc deposition system," *Surface & Coatings Technology*, vol. 231, pp. 247-252, 9/25/ 2013.
- [27] C. Chantharangsi, S. Denchitharoen, S. Chaiyakun, and P. Limsuwan, "Structure and Surface Morphology of Cr-Zr-N Thin Films Deposited by Reactive DC Magnetron Sputtering," *Procedia Engineering*, vol. 32, pp. 868-874, 2012.
- [28] C. Chantharangsi, S. Denchitharoen, S. Chaiyakun, and P. Limsuwan,

- "Structure and Surface Morphology of Cr-Zr-N Thin Films Deposited by Reactive DC Magnetron Sputtering," *Procedia Engineering*, vol. 32, pp. 868-874, 2012/01/01/ 2012.
- [29] Andreas Kafizas, Claire J. Carmalt, and I. P. Parkin, "CVD and precursor chemistry of transition metal nitrides," *Coordination Chemistry Reviews*, vol. 257, pp. 2073–2119, 2013.
- [30] Kumpon Leelaruedee, Patama Visuttiptikul, and N. Yongvanich, "Effect of the Added Polyethylene Glycol Molecular Weight and Calcination Heating Rate on the Morphology of TiO₂ Films Formed by Sol-Gel," *Materials Transactions*, vol. 58, pp. 465-470, 2017.
- [31] Daiane Roman, Juliane Bernardi, Cintia L.G. de Amorim, Fernando S. de Souza, Almir Spinelli, Cristiano Giacomelli, *et al.*, "Effect of deposition temperature on microstructure and corrosion resistance of ZrN thin films deposited by DC reactive magnetron sputtering," *Materials Chemistry and Physics*, vol. 130, pp. 147–153, 2011.
- [32] P.C. Wang, T.C. Cheng, H.C. Lin, M.J. Chen, K.M. Lin, and M. T. Yeh, "Effects of pre-sputtered Al interlayer on the atomic layer deposition of Al₂O₃ films on Mg–10Li–0.5Zn alloy," *Applied Surface Science*, vol. 270, pp. 452-456, 2013.
- [33] D. A. Jones, *Principles and prevention of corrosion*, 2 ed. Upper Saddle River, NJ 07458: Prentice Hall, 1995.
- [34] A. Bahrami, A. Delgado, C. Onofre, S. Muhl, and S. E. Rodil, "Structure, mechanical properties and corrosion resistance of amorphous Ti-Cr-O coatings," *Surface and Coatings Technology*, vol. 374, pp. 690-699, 2019/09/25/ 2019.
- [35] J.-Z. Kong, T.-J. Hou, Q.-Z. Wang, L. Yin, F. Zhou, Z.-F. Zhou, *et al.*, "Influence of titanium or aluminum doping on the electrochemical properties of CrN coatings in artificial seawater," *Surface and Coatings Technology*, vol. 307, pp. 118-124, 2016/12/15/ 2016.
- [36] D. Kek Merl, P. Panjan, and J. Kovač, "Corrosion and surface study of sputtered Al–W coatings with a range of tungsten contents," *Corrosion Science*, vol. 69, pp. 359-368, 2013/04/01/ 2013.
- [37] Y.-S. Choi, Y.-H. Yoo, J.-G. Kim, and S.-H. Kim, "A comparison of the corrosion resistance of Cu–Ni–stainless steel multilayers used for EMI shielding," *Surface and Coatings Technology*, vol. 201, pp. 3775-3782, 2006/12/04/ 2006.
- [38] J. E. G. González, a. F. J. H. Santana, and J. C. Mirza-rosca, "Effect of bacterial biofilm on 316 SS corrosion in natural seawater by eis," *Corrosion Science*, vol. 40, pp. 2141-2154, 1998/12/01/ 1998.
- [39] J.-B. Jorcin, M. E. Orazem, N. Pébère, and B. Tribollet, "CPE analysis by local electrochemical impedance spectroscopy," *Electrochimica Acta*, vol. 51, pp. 1473-1479, 2006/01/20/ 2006.
- [40] A. G. Cordeiro Neto, A. C. Pellanda, A. R. de Carvalho Jorge, J. B. Floriano, and M. A. Coelho Berton, "Preparation and evaluation of corrosion resistance of a self-healing alkyd coating based on microcapsules containing Tung oil," *Progress in Organic Coatings*, vol. 147, p. 105874, 2020/10/01/ 2020.
- [41] A. Zeng, E. Liu, I. F. Annergren, S. N. Tan, S. Zhang, P. Hing, *et al.*, "EIS capacitance diagnosis of nanoporosity effect on the corrosion protection of DLC

- films," *Diamond and Related Materials*, vol. 11, pp. 160-168, 2002/02/01/ 2002.
- [42] S.K. Ghosh, G.K. Dey, R.O. Dusane, and A. K. Grover, "Improved pitting corrosion behaviour of electrodeposited nanocrystalline Ni-Cu alloys in 3.0 wt.% NaCl solution," *Journal of Alloys and Compounds*, vol. 426, pp. 235-243, 2006.
- [43] R. Mishra and R. Balasubramaniam, "Effect of nanocrystalline grain size on the electrochemical and corrosion behavior of nickel," *Corrosion Science*, vol. 46, pp. 3019-3029, 2004.
- [44] C.L. Li, P. Wang, S.Q. Sun, K.T. Voisey, and D. G. McCartney, "Corrosion behaviour of Al_{86.0}Co_{7.6}Ce_{6.4} glass forming alloy with different microstructures," *Applied Surface Science*, vol. 384, pp. 116-124, 2016.
- [45] A. Obeydavi, A. Rezaeian, A. Shafyei, P. Kameli, and J.-W. Lee, "Prediction of amorphous phase formation by thermodynamic and kinetic analysis, a Fe-based thin film metallic glass deposited by direct current magnetron sputtering," *Materials Research Express*, vol. 6, p. 096407, 2019/07/01 2019.
- [46] Y. Zhang, Z. P. Lu, S. G. Ma, P. K. Liaw, Z. Tang, Y. Q. Cheng, *et al.*, "Guidelines in predicting phase formation of high-entropy alloys," *MRS Communications*, vol. 4, pp. 57-62, 2014.
- [47] X. Feng, K. Zhang, Y. Zheng, H. Zhou, and Z. Wan, "Effect of Zr content on structure and mechanical properties of (CrTaNbMoV)Zr_x high-entropy alloy films," *Nuclear Instruments and Methods in Physics Research Section B: Beam Interactions with Materials and Atoms*, vol. 457, pp. 56-62, 2019/10/15/ 2019.
- [48] G. Bertrand, H. Mahdjoub, and C. Meunier, "A study of the corrosion behaviour and protective quality of sputtered chromium nitride coatings," *Surface and Coatings Technology*, vol. 126, pp. 199-209, 2000.
- [49] S.K. Pradhan, C. Nouveau, A. Vasin, and M.-A. Djouadi, "Deposition of CrN coatings by PVD methods for mechanical application," *Surface & Coatings Technology*, vol. 200, pp. 141-145, 2005.
- [50] P. Hones, R. Sanjines, and F. Lévy, "Characterization of sputter-deposited chromium nitride thin films for hard coatings," *Surface and Coatings Technology*, vol. 94-95, pp. 398-402, 1997.
- [51] Q. Chen, Y. Cao, Z. Xie, T. Chen, Y. Wan, H. Wang, *et al.*, "Tribocorrosion behaviors of CrN coating in 3.5 wt% NaCl solution," *Thin Solid Films*, vol. 622, pp. 41-47, 2017.
- [52] Wen-Jun Chou, Ge-Ping Yu, and J.-H. Huang, "Corrosion resistance of ZrN films on AISI 304 stainless steel substrate," *Surface & Coatings Technology*, vol. 167, pp. 59-67, 2003.
- [53] GwangSeok Kim, BomSok Kim, SangYul Lee, and J. Hahn, "Structure and mechanical properties of Cr-Zr-N films synthesized by closed field unbalanced magnetron sputtering with vertical magnetron sources," *Surface & Coatings Technology*, vol. 200, pp. 1669-1675, 2005.
- [54] S.M. Kim, B.S. Kim, G.S. Kim, S.Y. Lee, and B. Y. Lee, "Evaluation of the high temperature characteristics of the CrZrN coatings," *Surface & Coatings Technology*, vol. 202, pp. 5521-5525, 2008.
- [55] Stefanie Spitz, Michael Stueber, Harald Leiste, Sven Ulrich, and H. J. Seifert, "Phase formation and microstructure evolution of reactively r.f. magnetron sputtering Cr-Zr oxynitride thin films," *Surface & Coatings Technology*, vol.

- 237, pp. 149-157, 2013.
- [56] P. Sukkul and R. Chaithammapakorn, "Effect of Zr and (Zr,Cr) interlayer on adhesion property of coating layers on H13 steel," Bachelor degree, Metallurgical engineering, Chulalongkorn university, Chulalongkorn university, 2015.
- [57] Li-Jian Meng and M. P. d. Santos, "Investigations of titanium oxide films deposited by d.c. reactive magnetron sputtering in different sputtering pressures," *Thin Solid Films*, vol. 226, pp. 22-29, 1993.
- [58] Li-jian Meng, M. Andritschky, and M. P. d. Santos, "The effect of substrate temperature on the properties of d.c. reactive magnetron sputtered titanium oxide films," *Thin Solid Films*, vol. 223, pp. 242-247, 1993.
- [59] S. Han, J.H. Lin, S.H. Tsai, S.C. Chung, D.Y. Wang, F.H. Lu, *et al.*, "Corrosion and tribological studies of chromium nitride coated on steel with an interlayer of electroplated chromium," *Surface and Coatings Technology*, vol. 133-134, pp. 460-465, 2000.
- [60] J. Creus, H. Idrissi, H. Mazille, F. Sanchette, and P. Jacquot, "Improvement of the corrosion resistance of CrN coated steel by an interlayer," *Surface and Coatings Technology*, vol. 107, pp. 183–190, 1998.
- [61] M. G. Fontana, *Corrosion Engineering*. Singapore: McGraw-Hill, 1986.
- [62] J. Lintymer, J. Gavaille, N. Martin, and J. Takadoum, "Glancing angle deposition to modify microstructure and properties of sputter deposited chromium thin films," *Surface and Coatings Technology*, vol. 174-175, pp. 316-323, 2003/09/01/ 2003.
- [63] T. Yanagitani and M. Suzuki, "Significant shear mode softening in a c-axis tilt nanostructured hexagonal thin film induced by a self-shadowing effect," *Scripta Materialia*, vol. 69, pp. 724-727, 2013/11/01/ 2013.
- [64] M. Ohring, *Materials Science of Thin Films*: Academic press, Inc., 1992.
- [65] M. Sheikhattar, H. Attar, S. Sharafi, and W. M. Carty, "Influence of surface crystallinity on the surface roughness of different ceramic glazes," *Materials Characterization*, vol. 118, pp. 570-574, 2016/08/01/ 2016.
- [66] Y. Li and Y. F. Cheng, "Effect of surface finishing on early-stage corrosion of a carbon steel studied by electrochemical and atomic force microscope characterizations," *Applied Surface Science*, vol. 366, pp. 95-103, 2016/03/15/ 2016.
- [67] W. Li and D. Y. Li, "Influence of surface morphology on corrosion and electronic behavior," *Acta Materialia*, vol. 54, pp. 445-452, 2006/01/01/ 2006.
- [68] B. Sivakumar, L. C. Pathak, and R. Singh, "Role of surface roughness on corrosion and fretting corrosion behaviour of commercially pure titanium in Ringer's solution for bio-implant application," *Applied Surface Science*, vol. 401, pp. 385-398, 2017/04/15/ 2017.
- [69] M. W. Chase, *NIST-JANAF Thermochemical Tables 2 Volume-Set (Journal of Physical and Chemical Reference Data Monographs)*. Maryland: American Institute of Physics, 1998.
- [70] H. Okamoto, "Supplemental Literature Review of Binary Phase Diagrams: B-Fe, Cr-Zr, Fe-Np, Fe-W, Fe-Zn, Ge-Ni, La-Sn, La-Ti, La-Zr, Li-Sn, Mn-S, and Nb-Re," *Journal of Phase Equilibria and Diffusion*, vol. 37, pp. 621-634, 2016/10/01 2016.

- [71] X. Yang and Y. Zhang, "Prediction of high-entropy stabilized solid-solution in multi-component alloys," *Materials Chemistry and Physics*, vol. 132, pp. 233-238, 2012/02/15/ 2012.
- [72] S. V. Ketov, X. Shi, G. Xie, R. Kumashiro, A. Churyumov, A. Bazlov, *et al.*, "Nanostructured Zr-Pd Metallic Glass Thin Film for Biochemical Applications," *Scientific Reports*, vol. 5, p. 7799, 01/15 2015.
- [73] S. V. Ketov, X. Shi, G. Xie, R. Kumashiro, A. Y. Churyumov, A. I. Bazlov, *et al.*, "Nanostructured Zr-Pd Metallic Glass Thin Film for Biochemical Applications," *Scientific Reports*, vol. 5, p. 7799, 2015/01/15 2015.
- [74] S. Ren, C. Du, Z. Liu, X. Li, J. Xiong, and S. Li, "Effect of fluoride ions on corrosion behaviour of commercial pure titanium in artificial seawater environment," *Applied Surface Science*, vol. 506, p. 144759, 2020/03/15/ 2020.
- [75] F. Vargas, H. Ageorges, P. Fauchais, M. E. López, and J. A. Calderon, "Permeation of saline solution in Al₂O₃-13wt.% TiO₂ coatings elaborated by atmospheric plasma spraying," *Surface and Coatings Technology*, vol. 220, pp. 85-89, 2013/04/15/ 2013.
- [76] I. Martínez and C. Andrade, "Application of EIS to cathodically protected steel: Tests in sodium chloride solution and in chloride contaminated concrete," *Corrosion Science*, vol. 50, pp. 2948-2958, 2008/10/01/ 2008.
- [77] K. Taweessup, P. Visuttiptikul, N. Yongvanich, and G. Lothongkum, "Corrosion behavior of Ti-Cr-N coatings on tool steel substrates prepared using DC magnetron sputtering at low growth temperatures," *Surface and Coatings Technology*, vol. 358, pp. 732-740, 2019/01/25/ 2019.
- [78] Y. Yang, C. Zhang, Y. Peng, Y. Yu, and L. Liu, "Effects of crystallization on the corrosion resistance of Fe-based amorphous coatings," *Corrosion Science*, vol. 59, pp. 10-19, 2012/06/01/ 2012.
- [79] V. Kalavathi and R. Kumar Bhuyan, "A detailed study on zirconium and its applications in manufacturing process with combinations of other metals, oxides and alloys – A review," *Materials Today: Proceedings*, vol. 19, pp. 781-786, 2019/01/01/ 2019.
- [80] M. Ohashi, M. Sawabu, H. Nakanishi, K. Ohashi, and K. Maeta, "Electrical and structural properties of epitaxially deposited chromium thin films," *Physica B: Condensed Matter*, vol. 536, pp. 790-792, 2018/05/01/ 2018.
- [81] S. Cui, X. Yin, Q. Yu, Y. Liu, D. Wang, and F. Zhou, "Polypyrrole nanowire/TiO₂ nanotube nanocomposites as photoanodes for photocathodic protection of Ti substrate and 304 stainless steel under visible light," *Corrosion Science*, vol. 98, pp. 471-477, 2015/09/01/ 2015.
- [82] K. Hladky, L. M. Callow, and J. L. Dawson, "Corrosion Rates from Impedance Measurements: An Introduction," *British Corrosion Journal*, vol. 15, pp. 20-25, 1980/01/01 1980.
- [83] J. Li, X. Lin, P. Guo, M. Song, and W. Huang, "Electrochemical behaviour of laser solid formed Ti-6Al-4V alloy in a highly concentrated NaCl solution," *Corrosion Science*, vol. 142, pp. 161-174, 2018/09/01/ 2018.
- [84] E. Poorqasemi, O. Abootalebi, M. Peikari, and F. Haqdar, "Investigating accuracy of the Tafel extrapolation method in HCl solutions," *Corrosion Science*, vol. 51, pp. 1043-1054, 2009/05/01/ 2009.
- [85] Z. Qiu, Z. Li, H. Fu, H. Zhang, Z. Zhu, A. Wang, *et al.*, "Corrosion mechanisms

- of Zr-based bulk metallic glass in NaF and NaCl solutions," *Journal of Materials Science & Technology*, vol. 46, pp. 33-43, 2020/06/01/ 2020.
- [86] S. Calderón, C. Almeida Alves, N. Manninen, A. Cavaleiro, and S. Carvalho, "Electrochemical Corrosion of Nano-Structured Magnetron-Sputtered Coatings," *Coatings*, vol. 9, p. 682, 10/20 2019.
- [87] Z. Lu, J. Wang, Y. Ling, Q. Zhou, Z. Zhang, and B. Hou, "Modified wrinkles from oxidation of Cr coatings under low partial pressure," *Surface and Coatings Technology*, vol. 387, p. 125547, 2020/04/15/ 2020.
- [88] A. K. Panda, A. Singh, R. Divakar, N. G. Krishna, V. R. Reddy, R. Thirumurugesan, *et al.*, "Crystallographic texture study of pulsed laser deposited Cr₂O₃ thin films," *Thin Solid Films*, vol. 660, pp. 328-334, 2018/08/30/ 2018.
- [89] A. Lippitz and T. Hübert, "XPS investigations of chromium nitride thin films," *Surface and Coatings Technology*, vol. 200, pp. 250-253, 2005/10/01/ 2005.
- [90] M. A. Korotin, I. S. Zhidkov, A. I. Kukharensko, S. O. Cholakh, A. S. Kamenetskikh, N. V. Gavrilov, *et al.*, "Interfacial reactions in Al₂O₃/Cr₂O₃ layers: Electronic structure calculations and X-ray photoelectron spectra," *Thin Solid Films*, vol. 665, pp. 6-8, 2018/11/01/ 2018.
- [91] P. Z. Si, H. X. Wang, W. Jiang, J. G. Lee, C. J. Choi, and J. J. Liu, "Synthesis, structure and exchange bias in Cr₂O₃/CrO₂/Cr₂O₅ particles," *Thin Solid Films*, vol. 519, pp. 8423-8425, 2011/09/30/ 2011.
- [92] A. Rizzo, M. A. Signore, L. Mirengi, and T. Di Luccio, "Synthesis and characterization of titanium and zirconium oxynitride coatings," *Thin Solid Films*, vol. 517, pp. 5956-5964, 2009/09/01/ 2009.
- [93] R. Brenier, J. Mugnier, and E. Mirica, "XPS study of amorphous zirconium oxide films prepared by sol-gel," *Applied Surface Science*, vol. 143, pp. 85-91, 1999/04/01/ 1999.
- [94] G. I. Cubillos, M. Bethencourt, J. J. Olaya, J. E. Alfonso, and J. F. Marco, "The influence of deposition temperature on microstructure and corrosion resistance of ZrO_xNy/ZrO₂ coatings deposited using RF sputtering," *Applied Surface Science*, vol. 309, pp. 181-187, 2014/08/01/ 2014.
- [95] M. Gondal, T. Fasasi, U. Baig, and A. Mekki, "Effects of Oxidizing Media on the Composition, Morphology and Optical Properties of Colloidal Zirconium Oxide Nanoparticles Synthesized via Pulsed Laser Ablation in Liquid Technique," *Journal of Nanoscience and Nanotechnology*, vol. 18, 06/15 2017.
- [96] A. Lyapin, L. P. H. Jeurgens, and E. J. Mittemeijer, "Effect of temperature on the initial, thermal oxidation of zirconium," *Acta Materialia*, vol. 53, pp. 2925-2935, 2005/06/01/ 2005.
- [97] G. I. Cubillos, M. E. Mendoza, J. E. Alfonso, G. Blanco, and M. Bethencourt, "Chemical composition and microstructure of zirconium oxynitride thin layers from the surface to the substrate-coating interface," *Materials Characterization*, vol. 131, pp. 450-458, 2017/09/01/ 2017.
- [98] A. Roustila, J. Chêne, and C. Séverac, "XPS study of hydrogen and oxygen interactions on the surface of zirconium," *Journal of Alloys and Compounds*, vol. 356-357, pp. 330-335, 2003/08/11/ 2003.
- [99] I. Beshpalov, M. Datler, S. Buhr, W. Drachsel, G. Rupprechter, and Y. Suchorski, "Initial stages of oxide formation on the Zr surface at low oxygen pressure: An in situ FIM and XPS study," *Ultramicroscopy*, vol. 159, pp. 147-151,

- 2015/12/01/ 2015.
- [100] O. Appel, G. Breuer, S. Cohen, O. Beerli, T. Kyratsi, Y. Gelbstein, *et al.* (2019, 2019/05//). The Initial Stage in Oxidation of ZrNiSn (Half Heusler) Alloy by Oxygen. *Materials (Basel, Switzerland) 12(9)*. Available:
- [101] W. Ma, W. Herbert, S. Senanayake, and B. Yildiz, "Non-equilibrium oxidation states of zirconium during early stages of metal oxidation," *Applied Physics Letters*, vol. 106, 03/09 2015.
- [102] Z. Azdad, L. Marot, L. Moser, R. Steiner, and E. Meyer, "Valence band behaviour of zirconium oxide, Photoelectron and Auger spectroscopy study," *Scientific reports*, vol. 8, pp. 16251-16251, 2018.
- [103] B. Normand, H. Takenouti, M. Keddami, H. Liao, G. Monteil, and C. Coddet, "Electrochemical impedance spectroscopy and dielectric properties of polymer: application to PEEK thermally sprayed coating," *Electrochimica Acta*, vol. 49, pp. 2981-2986, 2004/07/30/ 2004.
- [104] P. L. Brown, E. Curti, and B. Grambow, *Chemical Thermodynamics of Zirconium*, 2005.
- [105] B. Ensor, A. M. Lucente, M. J. Frederick, J. Sutliff, and A. T. Motta, "The role of hydrogen in zirconium alloy corrosion," *Journal of Nuclear Materials*, vol. 496, pp. 301-312, 2017/12/01/ 2017.
- [106] C. Zhang, *Soil and Groundwater Remediation: Fundamentals, Practices, and Sustainability*: John Wiley & Sons, Inc., 2019.
- [107] V. Renčiuková, J. Macák, P. Sajdl, R. Novotný, and A. Krausová, "Corrosion of zirconium alloys demonstrated by using impedance spectroscopy," *Journal of Nuclear Materials*, vol. 510, pp. 312-321, 2018/11/01/ 2018.
- [108] J. Xu, T. Shoji, and C. Jang, "The effects of dissolved hydrogen on the corrosion behavior of Alloy 182 in simulated primary water," *Corrosion Science*, vol. 97, pp. 115-125, 2015/08/01/ 2015.
- [109] T. Kim, K. J. Choi, S. C. Yoo, Y. Lee, and J. H. Kim, "Influence of dissolved hydrogen on the early stage corrosion behavior of zirconium alloys in simulated light water reactor coolant conditions," *Corrosion Science*, vol. 131, pp. 235-244, 2018/02/01/ 2018.
- [110] K. Khojier, H. Savaloni, Z. Ashkabusli, and N. Z. Dehnavi, "Structural, mechanical and tribological characterization of chromium oxide thin films prepared by post-annealing of Cr thin films," *Applied Surface Science*, vol. 284, pp. 489-496, 2013/11/01/ 2013.
- [111] J. C. Brice, "Some thermodynamic aspects of the growth of strained crystals," *Journal of Crystal Growth*, vol. 28, pp. 249-253, 1975/03/01/ 1975.
- [112] I. Milošev, H. H. Strehblow, and B. Navinšek, "Comparison of TiN, ZrN and CrN hard nitride coatings: Electrochemical and thermal oxidation," *Thin Solid Films*, vol. 303, pp. 246-254, 1997/07/15/ 1997.
- [113] J. F. Moulder, W. F. Stickle, P. E. Sobol, and K. D. Bombem, *Handbook of X-ray Photoelectron Spectroscopy*. Eden Prairie, Minnesota 55344: Perkin-Elmer Corporation, 1992.
- [114] A. Rizzo, M. A. Signore, L. Mirengi, L. Tapfer, E. Piscopiello, E. Salernitano, *et al.*, "Sputtering deposition and characterization of zirconium nitride and oxynitride films," *Thin Solid Films*, vol. 520, pp. 3532-3538, 2012/02/29/ 2012.
- [115] G. I. Cubillos, J. J. Olaya, M. Bethencourt, G. Antorrena, and K. El Amrani,

- "Synthesis and characterization of zirconium oxynitride ZrO_xNy coatings deposited via unbalanced DC magnetron sputtering," *Materials Chemistry and Physics*, vol. 141, pp. 42-51, 2013/08/15/ 2013.
- [116] A. Conde, A.B. Cristóbal, G. Fuentes, T. Tate, and J. d. Damborenea, "Surface analysis of electrochemically stripped CrN coatings," *Surface & Coatings Technology*, vol. 201, pp. 2588-2595, 2006.
- [117] M. Matsuoka, S. Isotani, W. Sucasaire, N. Kuratani, and K. Ogata, "X-ray photoelectron spectroscopy analysis of zirconium nitride-like films prepared on Si(100) substrates by ion beam assisted deposition," *Surface & Coatings Technology*, vol. 202, pp. 3129-3135, 2008.
- [118] M.-H. Chan, P.-L. Wu, and F.-H. Lu, "Preparation of ZrN_xO_y films by magnetron sputtering using air as a reactive gas," *Thin Solid Films*, vol. 518, pp. 7300-7303, 2010.
- [119] C. Pei, L. Deng, H. Liu, Z. He, C. Xiang, S. Zhang, *et al.*, "Corrosion inhibition behaviors of ZrN_x thin films with varied N vacancy concentration," *Vacuum*, vol. 162, pp. 28-38, 2019/04/01/ 2019.
- [120] P. Wongpanya, T. Wongpinij, P. Photongkam, Chonthicha, Keawhan, S. Tunmee, *et al.*, "THE CORROSION BEHAVIOR OF CHROMIUM NITRIDE FILM ON AISI 4140 AND H 13 STEELS," 2016.
- [121] B. Subramanian, V. Swaminathan, and M. Jayachandran, "Microstructural, tribological and electrochemical corrosion studies on reactive DC magnetron sputtered zirconium nitride films with Zr interlayer on steel," *Metals and Materials International*, vol. 18, pp. 957-964, 2012/12/01 2012.

Appendix A

General information

A.1 Materials and substrate preparation

Details of chemicals and materials using in this experimental are listed in table A-1. As description in previous chapter, both of metallic and nitride films were deposited on a disk shape H13 steel. Before deposition process, H13 steel bars were heat-treated for elimination of retained austenite. The diagram of heat treatment is shown in figure A-1. Afterward, heat treated H13 bar were cut to a disk shape with 25.0 mm in thickness and polished with emery paper number 320, 400, 600, 800, 1000, 1200, 2000 and finishing with alumina powder (particle size 1 μm).

Table A-1 Details of chemical and materials using in this experimental

Chemicals/materials	Details
AISI H13 steels	5% wt. Cr, 1.5% wt. Mo, 1% wt. V, 0.4% wt.C and Fe balance, diameter 25.4 mm
Emery paper	No. 320, 400, 600, 800, 1000, 1200 and 2000
Alumina powder	particle size $\sim 1 \mu\text{m}$
Acetone	Ajax

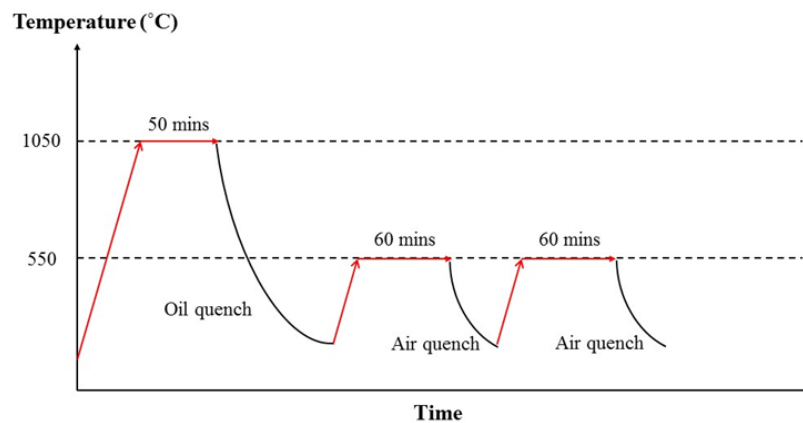


Figure A-1 Heat treatment diagram of H13 steels

A.2 Thickness measurement with image J software

In this research, all films were measured their thickness by FESEM images integrating with image J software. Each film was measure at least 30 lines and 3 fields for estimate thickness. The example of program display and measurement of pure chromium film (Cr-film) is shown in figure A-2.

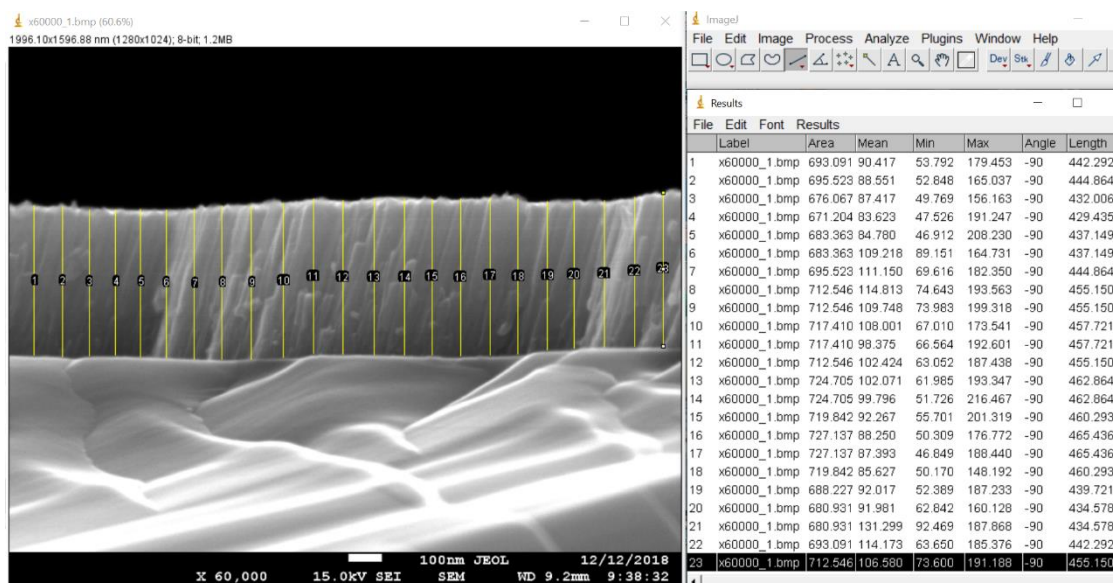


Figure A-2 Thickness measurement of the Cr-film by FESEM integrating with image J software

A.3 The XRD patterns for analyzation

The XRD patterns, which were used for phase identification in this research, are listed in this section. It composed of 3 patterns in metallic chapter and 2 patterns in nitride chapter. The metallic chapter consisted of ICSD 01-085-1336, 01-089-4892 and ICSD 01-086-1449, while the nitride chapter consisted of ICSD 01-076-2494 and 03-065-0972.

1. Chromium (ICSD 01-085-1336)

Crystallographic parameters

Crystal system: Cubic

Space group: Im-3m

Space group number: 229

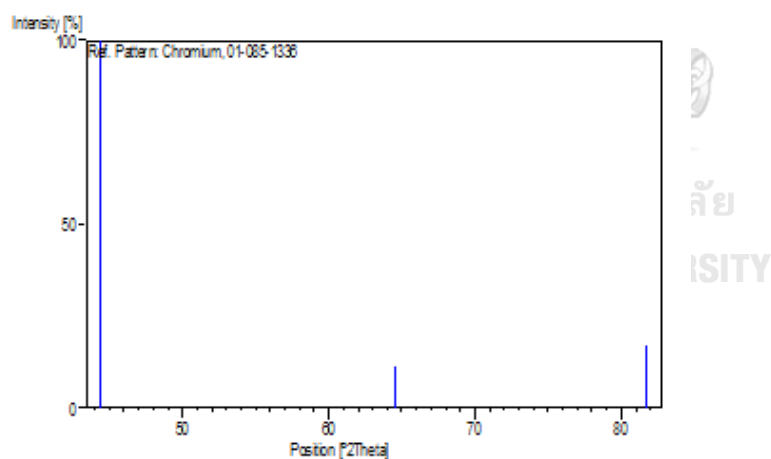
a (Å): 2.8849, b (Å): 2.8849 and c (Å): 2.8849

Alpha (°): 90.0000, Beta (°): 90.0000 and Gamma (°): 90.0000

Peak list

No.	h	k	l	d (Å)	2Theta (°)	I (%)
1	1	1	0	2.03996	44.371	100.0
2	2	0	0	1.44247	64.554	11.2
3	2	1	1	1.17777	81.693	17.2

Stick Pattern



2. Zirconium (ICSD 01-089-4892)

Crystallographic parameters

Crystal system: Hexagonal

Space group: P63/mmc

Space group number: 194

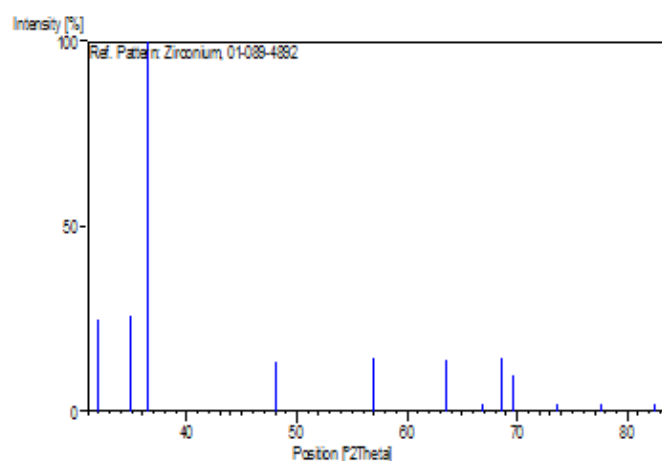
a (Å): 3.2312, b (Å): 3.2312 and c (Å): 5.1477

Alpha (°): 90.0000, Beta (°): 90.0000 and Gamma (°): 120.0000

Peak list

No.	h	k	l	d (Å)	2Theta (°)	I (%)
1	1	0	0	2.79830	31.957	25.0
2	0	0	2	2.57385	34.829	25.8
3	1	1	1	2.45853	36.519	100.0
4	1	0	2	1.89437	47.986	13.3
5	1	1	0	1.61560	56.952	14.4
6	1	0	3	1.46279	63.552	14.3
7	2	0	0	1.39915	66.809	2.0
8	1	1	2	1.36836	68.518	14.3
9	2	0	1	1.35017	69.573	10.1
10	0	0	4	1.28692	73.534	1.8
11	2	0	2	1.22926	77.605	2.2

Stick Pattern



2. Zirconium dioxide (ICSD 01-086-1449)

Crystallographic parameters

Crystal system: Monoclinic

Space group: P21/c

Space group number: 14

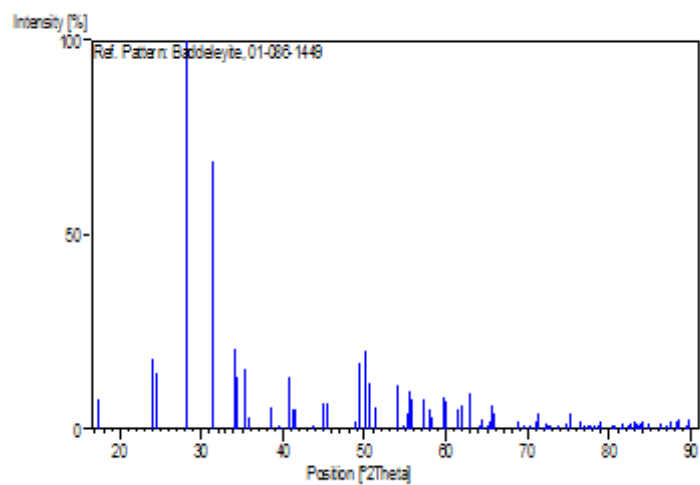
a (Å): 5.1442, b (Å): 5.2097 and c (Å): 5.3112

Alpha (°): 90.0000, Beta (°): 99.2200 and Gamma (°): 90.0000

Peak list

No.	h	k	l	d (Å)	2Theta (°)	I (%)
1	1	0	0	5.07776	17.451	7.6
2	0	1	1	3.69538	24.063	18.4
3	1	1	0	3.63627	24.460	14.3
4	-1	1	1	3.16267	28.194	100.0
5	1	1	1	2.83923	31.484	69.0
6	0	0	2	2.62129	34.179	20.7
7	0	2	0	2.60485	34.401	13.5
8	2	0	0	2.53888	35.324	15.8
9	0	2	1	2.33276	38.563	5.7
10	-2	1	1	2.21246	40.750	13.9
11	-1	2	1	2.17954	41.394	5.3
12	1	1	2	2.01932	44.849	6.8
13	2	1	1	1.98999	45.547	13.9
14	0	2	2	1.84769	49.278	5.3
15	2	2	0	1.81813	50.134	6.8
16	-1	2	2	1.80298	50.585	6.6
17	-2	2	1	1.78224	51.216	17.0

Stick Pattern



จุฬาลงกรณ์มหาวิทยาลัย
CHULALONGKORN UNIVERSITY

4. Chromium nitride (ICSD 01-076-2494)

Crystallographic parameters

Crystal system: Cubic

Space group: Fm-3m

Space group number: 225

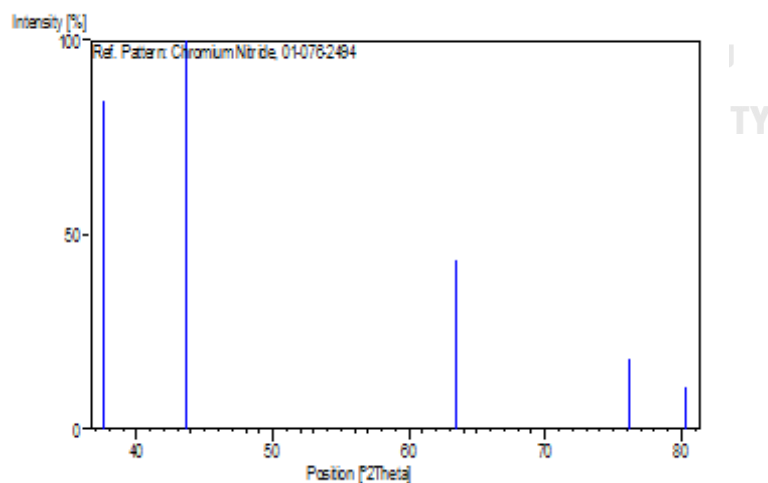
a (Å): 4.1400, b (Å): 4.1400 and c (Å): 4.1400

Alpha (°): 90.0000, Beta (°): 90.0000 and Gamma (°): 90.0000

Peak list

No.	h	k	l	d (Å)	2Theta (°)	I (%)
1	1	1	1	2.39023	37.601	84.7
2	2	0	0	2.07000	43.694	100.0
3	2	2	0	1.46371	63.507	43.7
4	3	1	1	1.24826	76.209	18.3
5	2	2	2	1.19511	80.263	10.9

Stick Pattern



4. Zirconium nitride (ICSD 03-065-0972)

Crystallographic parameters

Crystal system: Cubic

Space group: Fm-3m

Space group number: 225

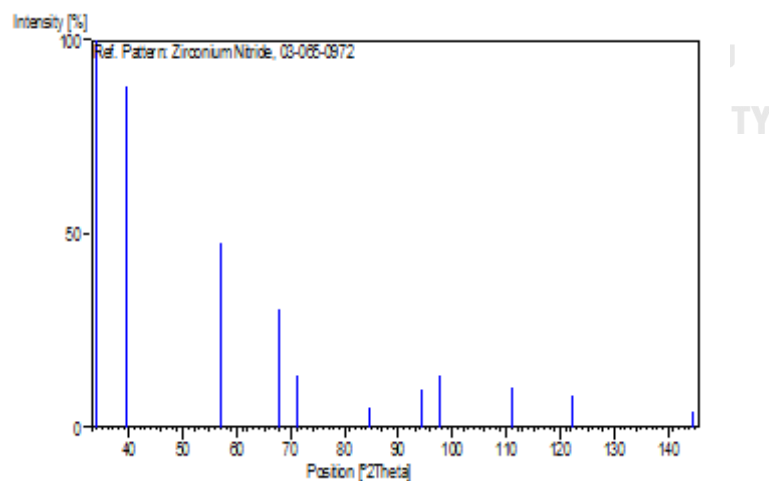
a (Å): 4.5750, b (Å): 4.5750 and c (Å): 4.5750

Alpha (°): 90.0000, Beta (°): 90.0000 and Gamma (°): 90.0000

Peak list

No.	h	k	l	d (Å)	2Theta (°)	I (%)
1	1	1	1	2.64138	33.911	100.0
2	2	0	0	2.28750	39.357	88.2
3	2	2	0	1.61751	56.878	47.6
4	3	1	1	1.37941	67.894	30.6
5	2	2	2	1.32069	71.360	13.2

Stick Pattern



VITA

NAME Kumpon Leelaruedee

DATE OF BIRTH 22 June 1990

PLACE OF BIRTH Chonburi

INSTITUTIONS ATTENDED Bachelor of engineering, Advanced materials and nanotechnology, Faculty of engineering and industrial technology, Silpakorn university
Master of engineering, Metallurgical and materials engineering, Faculty of engineering, Chulalongkorn university

HOME ADDRESS 276/117 Bangmod Thung-Khru Bangkok 10140



จุฬาลงกรณ์มหาวิทยาลัย
CHULALONGKORN UNIVERSITY